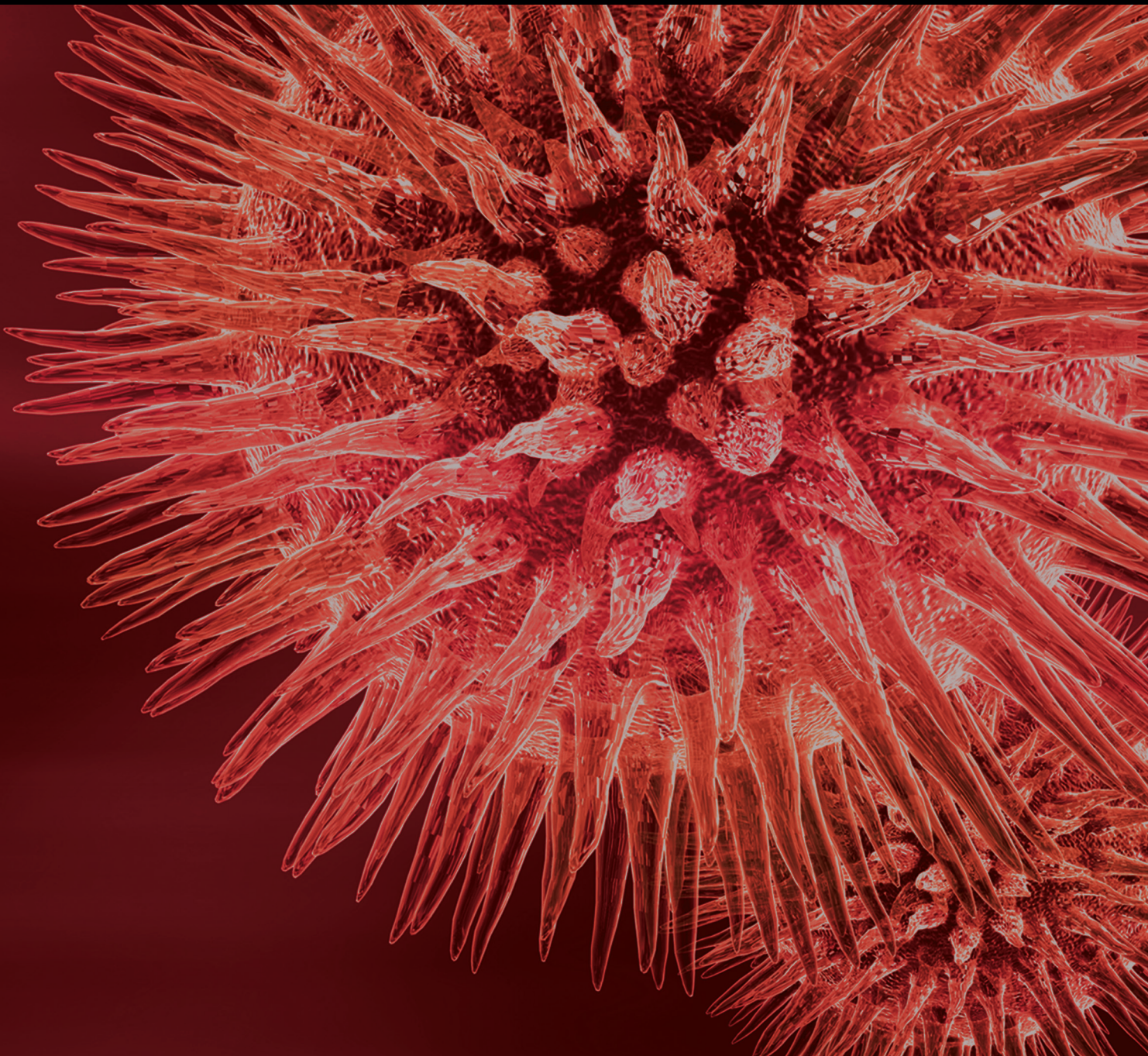


BioMed Research International

State-of-the-Art in Integrated Breast Imaging

Lead Guest Editor: Graziella Di Grezia

Guest Editors: Gianluca Gatta, Luca Brunese, and Giuseppe Falco






State-of-the-Art in Integrated Breast Imaging

BioMed Research International

State-of-the-Art in Integrated Breast Imaging

Lead Guest Editor: Graziella Di Grezia

Guest Editors: Gianluca Gatta, Luca Brunese, and Giuseppe Falco




Copyright © 2019 Hindawi. All rights reserved.





This is a special issue published in “BioMed Research International.” All articles are open access articles distributed under the Creative Commons Attribution License, which permits unrestricted use, distribution, and reproduction in any medium, provided the original work is properly cited.

Contents




State-of-the-Art in Integrated Breast Imaging

Graziella Di Grezia , Gianluca Gatta, Luca Brunese, and Giuseppe Falco
Editorial (2 pages), Article ID 7596059, Volume 2019 (2019)




Efficacy of Second-Look Ultrasound with MR Coregistration for Evaluating Additional Enhancing Lesions of the Breast: Review of the Literature

Maria Antonietta Mazzei , Letizia Di Giacomo , Alfonso Fausto, Francesco Gentili ,
Francesco Giuseppe Mazzei , and Luca Volterrani
Review Article (8 pages), Article ID 3896946, Volume 2018 (2019)





A New Challenge for Radiologists: Radiomics in Breast Cancer

Paola Crivelli , Roberta Eufrasia Ledda, Nicola Parascandolo , Alberto Fara , Daniela Soro,
and Maurizio Conti
Review Article (10 pages), Article ID 6120703, Volume 2018 (2019)


Patch Based Grid Artifact Suppressing in Digital Mammography

Qingqing Ling, Shuyu Wu, Xiaoman Duan, Genggeng Qin , Jianhui Ma, Chaomin Chen,
Hongliang Qi , Linghong Zhou , and Yuan Xu 
Research Article (11 pages), Article ID 9727259, Volume 2018 (2019)




Role of Magnetic Resonance Imaging in the Preoperative Staging and Work-Up of Patients Affected by Invasive Lobular Carcinoma or Invasive Ductolobular Carcinoma

Valeria Selvi, Jacopo Nori, Icro Meattini, Giulio Francolini, Noemi Morelli, Diego Di Benedetto,
Giulia Bicchierai , Federica Di Naro, Maninderpal Kaur Gill , Lorenzo Orzalesi, Luis Sanchez,
Tommaso Susini , Simonetta Bianchi, Lorenzo Livi, and Vittorio Miele 
Research Article (7 pages), Article ID 1569060, Volume 2018 (2019)





Use of a Total Variation Minimization Iterative Reconstruction Algorithm to Evaluate Reduced Projections during Digital Breast Tomosynthesis

Tsutomu Gomi  and Yukio Koibuchi
Research Article (14 pages), Article ID 5239082, Volume 2018 (2019)

The Evolving Role of Ultrasound Guided Percutaneous Laser Ablation in Elderly Unresectable Breast Cancer Patients: A Feasibility Pilot Study

Jacopo Nori, Maninderpal Kaur Gill , Icro Meattini, Camilla Delli Paoli, Dalmar Abdulcadir,
Ermanno Vanzi, Cecilia Boeri, Silvia Gabbrielli, Elisabetta Giannotti, Francesco Lucci, Vania Vezzosi,
Diego De Benedetto, Giulia Bicchierai , Simonetta Bianchi, Luis Sanchez, Lorenzo Orzalesi,
Guido Carmelo, Vittorio Miele , Lorenzo Livi, and Donato Casella
Research Article (7 pages), Article ID 9141746, Volume 2018 (2019)

Use of Quantitative Morphological and Functional Features for Assessment of Axillary Lymph Node in Breast Dynamic Contrast-Enhanced Magnetic Resonance Imaging

Roberta Fusco , Mario Sansone , Vincenza Granata , Maurizio Di Bonito, Franca Avino,
Orlando Catalano, Gerardo Botti, and Antonella Petrillo 
Review Article (8 pages), Article ID 2610801, Volume 2018 (2019)

Editorial

State-of-the-Art in Integrated Breast Imaging

Graziella Di Grezia ¹, **Gianluca Gatta**,² **Luca Brunese**,³ and **Giuseppe Falco**⁴

¹Radiology Department, “G. Criscuoli” Hospital, Sant’Angelo dei Lombardi, Italy

²Radiology Department, “University of Campania Luigi Vanvitelli”, Naples, Italy

³Medicine and Health Science Department, “University of Molise”, Campobasso, Italy

⁴Breast Surgery Department, Arcispedale Santa Maria Nuova, Reggio Emilia, Italy

Correspondence should be addressed to Graziella Di Grezia; graziella.digrezia@unicampania.it

Received 23 December 2018; Accepted 24 December 2018; Published 6 January 2019

Copyright © 2019 Graziella Di Grezia et al. This is an open access article distributed under the Creative Commons Attribution License, which permits unrestricted use, distribution, and reproduction in any medium, provided the original work is properly cited.

Innovation in radiology is a constant, thanks to technology evolution. Spread research and the daily request of the marketplace and of the other specializations necessitate always new possibilities not only in diagnostic but also in therapeutic fields [1].

Breast cancer represents the first oncological disease for the women and despite the efforts to promote early diagnosis, also with screening programs, advanced disease is already diagnosed.

Estrogen/Progestinic therapies, aesthetic surgery, and the greater life expectancy must be followed by a multimodality approach with a clinical exam and an advanced technology set of exams.

A personalized approach is gradually replacing the “one size fits all” of the previous prevention programs [2]; a breast radiology should answer not only on the diagnosis, but also on follow-up, response to therapy prediction, and therapeutic procedure as alternative to surgery [3].

In this issue we deal with 2D and tomosynthesis evolution, to US/MR coregistration and to features for radiomic approach and laser therapy in nonsurgical old patients.

In detail, Q. Ling et al. in the study “Patch Based Grid Artifact Suppressing in Digital Mammography” present a solution for fast suppressing grid artifacts and consequently high quality digital mammography.

This is a valid possibility of improving imaging quality also in hospitals and clinics that do not have tomosynthesis or in screening programs.

To date, in some countries there is already a dispute on dose problem in tomosynthesis exams; however, the increase

is really minimal and some authors (T. Gomi and Y. Koibuchi in “Use of a Total Variation Minimization Iterative Reconstruction Algorithm to Evaluate Reduced Projections during Digital Breast Tomosynthesis”) have evaluated the efficacies of the iterative reconstruction algorithm that allows reducing number of projections and reduce radiation doses [4].

Mammography is only the first step, especially in over forty women and in screening programs; however more studies have been conducted to optimize breast MRI results that is to date a very sensible but low specific exam.

R. Fusco et al. in the manuscript “Use of Quantitative Morphological and Functional Features for Assessment of Axillary Lymph Node in Breast Dynamic Contrast-Enhanced Magnetic Resonance Imaging” evaluated morphologic features and dynamic behavior to predict metastatic disease with a good diagnostic accuracy.

One of the long-standing problems is the US second look to identify additional breast lesions detected on MRI.

The different position of the patient, breast size, and the small size of some lesions on MRI do not allow concluding the diagnosis on second look and in some cases, a MRI guided biopsy could be necessary.

A. Mazzei et al. in the study “Efficacy of Second-Look Ultrasound with MR Coregistration for Evaluating Additional Enhancing Lesions of the Breast: Review of the Literature” present that the coregistration of US and MRI allows reducing these problems also thanks to multiplanar reconstructions.

Therapeutic possibilities have been addressed in the study “The Evolving Role of Ultrasound Guided Percutaneous

Laser Ablation in Elderly Unresectable Breast Cancer Patients: A Feasibility Pilot Study” by J. Nori et al.

Interventional procedures are not always and only diagnostic [5]; laser ablation is a really alternative to surgery in old patients with high anesthesiological risk and not eligible to surgery with a good compliance of the patients, less complications, and shorter hospitalization in comorbidity patients.

In the future the radiologist should predict the therapy response to breast cancer and orient geneticists [6, 7], oncologist, radiotherapist, and surgeons on the best personalized approach to breast cancer in specific patients. It would be possible thanks to radiomics features and multidisciplinary approach including biomedical engineers and physics (P. Crivelli et al. in “A New Challenge for Radiologists: Radiomics in Breast Cancer”) [8].

Conflicts of Interest

The editors declare that they have no conflicts of interest regarding the publication of the special issue.

Acknowledgments

The guest editorial team would like to express gratitude to all the authors for their interest in selecting this special issue as a venue for disseminating their scholarly work. The editors also wish to thank the anonymous reviewers for their careful reading of the manuscripts submitted to this special issue collection and their many insightful comments and suggestions.

Graziella Di Grezia
Gianluca Gatta
Luca Brunese
Giuseppe Falco

References

- [1] C. K. Kuhl, “The changing world of breast cancer,” *Plastic Surgical Nursing*, vol. 36, no. 1, pp. 31–49, 2016.
- [2] G. Di Grezia, F. Somma, N. Serra et al., “Reducing costs of breast examination: ultrasound performance and inter-observer variability of expert radiologists versus residents,” *Cancer Investigation*, vol. 34, no. 7, pp. 355–360, 2016.
- [3] G. Di Grezia, V. Prisco, T. Iannaccone, R. Grassi, N. Serra, and G. Gatta, “Personality disorders and temperamental traits in patients with breast disease: Preliminary results,” *Minerva Psichiatrica*, vol. 57, no. 3, pp. 85–92, 2016.
- [4] P. S. Sujlana, M. Mahesh, S. Vedantham, S. C. Harvey, L. A. Mullen, and R. W. Woods, “Digital breast tomosynthesis: Image acquisition principles and artifacts,” *Clinical Imaging*, vol. S0899-7071, pp. 30201–30208, 2018.
- [5] G. Gatta, G. Di Grezia, A. Ancona et al., “Underestimation of atypical lobular hyperplasia and lobular carcinoma in situ at stereotaxic 11-gauge vacuum-assisted breast biopsy,” *European Journal of Inflammation*, vol. 11, no. 3, pp. 825–835, 2013.
- [6] G. Di Grezia, T. Romano, F. De Francesco et al., “Breast ultrasound in the management of gynecomastia in Peutz-Jeghers

syndrome in monozygotic twins: Two case reports,” *Journal of Medical Case Reports*, vol. 8, no. 1, p. 440, 2014.

- [7] G. A. Ferraro, T. Romano, F. De Francesco et al., “Management of prepubertal gynecomastia in two monozygotic twins with Peutz-Jeghers syndrome: from aromatase inhibitors to subcutaneous mastectomy,” *Aesthetic Plastic Surgery*, vol. 37, no. 5, pp. 1012–1022, 2013.
- [8] K. Pinker, J. Chin, A. N. Melsaether, E. A. Morris, and L. Moy, “Precision medicine and radiogenomics in breast cancer: new approaches toward diagnosis and treatment,” *Radiology*, vol. 287, no. 3, pp. 732–747, 2018.

Review Article

Efficacy of Second-Look Ultrasound with MR Coregistration for Evaluating Additional Enhancing Lesions of the Breast: Review of the Literature

Maria Antonietta Mazzei ¹, **Letizia Di Giacomo** ¹, **Alfonso Fausto**,² **Francesco Gentili** ¹, **Francesco Giuseppe Mazzei** ² and **Luca Volterrani**¹

¹Department of Medical, Surgical and Neuro Sciences, Diagnostic Imaging, University of Siena, Azienda Ospedaliera Universitaria Senese, Viale Bracci 10, 53100 Siena, Italy

²Diagnostic Imaging, Azienda Ospedaliera Universitaria Senese, Viale Bracci 10, 53100 Siena, Italy

Correspondence should be addressed to Letizia Di Giacomo; digileti@libero.it

Received 14 December 2017; Accepted 26 September 2018; Published 21 October 2018

Guest Editor: Graziella Di Grezia

Copyright © 2018 Maria Antonietta Mazzei et al. This is an open access article distributed under the Creative Commons Attribution License, which permits unrestricted use, distribution, and reproduction in any medium, provided the original work is properly cited.

Contrast enhanced magnetic resonance imaging (CE-MRI) has acquired a central role in the field of diagnosis and evaluation of breast cancer due to its high sensitivity; on the other hand, MRI has shown a variable specificity because of the wide overlap between the imaging features of benign and malignant lesions. Therefore, when an additional breast lesion is identified at CE-MRI, a second look with targeted US is generally performed because it provides additional information to further characterise the target lesion and makes it possible to perform US-guided biopsies which are costless and more comfortable for patients compared with MRI-guided ones. Nevertheless, there is not always a correspondence between CE-MR findings and targeted US due to several factors including different operator's experience and position of patients. A new technique has recently been developed in order to overcome these limitations: US with MR coregistration, which can synchronise a sonography image and the MR image with multiplanar reconstruction (MPR) of the same section in real time. The aim of our study is to review the literature concerning the second look performed with this emerging and promising technique, showing both advantages and limitations in comparison with conventional targeted US.

1. Introduction

Contrast-enhanced magnetic resonance imaging (CE-MRI) of the breast has progressively acquired a central role in the field of detection and evaluation of breast cancer due to its high sensitivity, ranging from 94% to 100% for invasive carcinoma and from 40% to 100% for ductal carcinoma in situ (DCIS) [1–5]. On the other hand, MRI still shows low to moderate specificity (72%) and moderate positive predictive values (PVVs) for lesion characterisation [6] due to a wide overlap between the imaging features of benign and malignant lesions [7–15]. Therefore, when abnormalities detected on MRI are occult on mammograms or are not identified with previously performed breast ultrasonography (US), a targeted second-look US is commonly prescribed [16]. The use of targeted US has several advantages: first it can provide

additional information for a further characterisation of the additional lesion when correlated with MRI findings [17, 18]; second, it makes it possible to practise US-guided biopsies which are preferable to the MR-guided ones because they are superior in terms of accessibility, efficacy, and comfort for patients [19]. However, it has been observed that the detection rate of the additional lesions with second-look US is variable, with a reported range between 23% and 82,1%; this wide range of variability can be attributed to different factors which may include technical differences and different reader experience [20]. A new innovative technique has recently been developed in order to overcome this problem by using MR coregistration during live US examination. Different vendors have used various names for this revolutionary technology which enables coregistration of a previously acquired MR volume during US examination with magnetic sensors on the US probe and

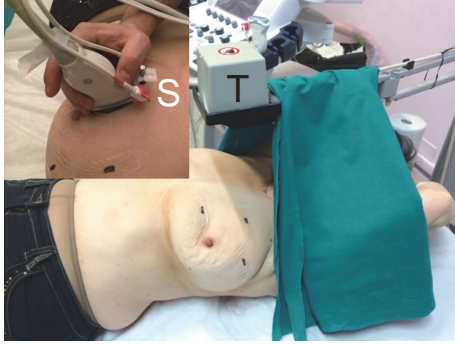


FIGURE 1: US-MR coregistration equipment composition: a pair of freehand sensors (S) and a fixed transmitter (T) connected to a position-sensing unit embedded in the US equipment.

a transmitter connected to US equipment [21, 22]. Several studies have shown that MR navigated US is an accurate method which increases US detection rate of MR-detected additional lesions [21–32]. The aim of our study was to give an update of the literature concerning the utility of second-look US coregistered with breast MR showing both the advantages and disadvantages of this emerging and promising technique.

2. Materials and Methods

We performed computerised research on PubMed database, Google, and ResearchGate by using the following search terms: “Breast volume navigation”, “second-look breast lesions” and “second-look real time-ultrasonography”. Full texts were then retrieved, including those of reviews concerning various coregistration techniques; nevertheless, in three cases it was not possible to obtain either the full text or the abstract because they were available only in Japanese language. Finally, in order to make our research more complete, a systematic review of the references of each article was performed. After carefully reading the articles, we analysed the methods and the systematic errors of each system if reported, and compared the clinical value of each reported technology.

2.1. Technical Principles of Ultrasound with MR Coregistration.

The equipment consists of two electromagnetic sensors which are attached to the US probe, a portable electromagnetic transmitter that is positioned near the patient under examination, and a position-sensing unit that connects the electromagnetic sensors and the transmitter enabling the tracking probe position and orientation within the electromagnetic field embedded in US equipment. After uploading the preacquired MR volume in the US equipment, coregistration can be obtained by matching skin and MR markers. The matching can be obtained coupling at least three pairs of points, one point and a plane, or automatically, according to different vendors. The coregistration is usually displayed on a US monitor showing US and MR images side by side or overlaying both images, the so-called fusion images (Figure 1). According to a recent review of Young Park et

al. the following ultrasound navigation systems are commercially available: Real-time Virtual Sonography (Hitachi Medical Corporation); Volume Navigation (GE Healthcare); eSie Fusion (Siemens Healthcare); Virtual Navigator (Esaote); PercuNav (Philips Healthcare); and Smart Fusion (Toshiba Medical Systems Corporation). These systems operate on the basis of similar equipment components and technical principles as described above [33]. The possibility of synchronising MR and US images by using multiplanar reconstruction (MPR) of the same section in real time is a great advantage, as it makes the exam more objective and less operator-dependent.

Nevertheless, an important limitation which has to be taken into account is that this new technique requires images information obtained from two different modalities at different times; breast tissues are soft and easily deformable, so that the position of the different structures may undergo significant variations from one exam to another, causing spatial displacement and misalignment. In order to overcome this problem, it is necessary to perform a nonrigid registration which requires application of the best transformation algorithm, making it possible to obtain an alignment with the least error between two breast images [34, 35]. Different coregistration methods have been developed with the aim of obtaining the best result. At one extreme, patient position and algorithms have been developed to reduce deformations due to the mechanical properties of the breast as much as possible; at the other extreme, algorithms have been developed to model the deformations imposed on the images using simple functions. In this case, landmarks are identified between the two images to be registered and a transformation is computed to coregister these landmarks. With regard to the breast, anatomic features can be either at the surface or internal [36].

2.2. Additional Supine MRI for Volume Navigation System: Technical Limits and Advantages. Breast MRI is commonly performed in the prone position because it minimises breast motion due to respiration and reduces the potential interference with the beating heart. In addition, the coil coupling is improved. [37]

Nevertheless, breast tissue is highly mobile and deformable and composition may vary with the individual hormonal status such as menstrual cycle. These factors may cause difficulties in coregistration due to the different position between ultrasound and MR examination (supine versus prone) that may lead to a misdiagnosis of breast lesions on second-look ultrasound [33]. In an attempt to minimise spatial displacement, various solutions have then been adopted.

Piron et al. developed a hybrid biopsy system based on the standard closed-bore MR magnet configuration, merging prebiopsy MR and real-time US information in one procedure, and proposed to perform both US and MR image acquisition in the prone position, obtaining encouraging results. [38].

In a pilot study, Causer et al. evaluated the accuracy of the same MR-US coregistration system in vivo; both MR and US examinations were performed with the patient in the

prone position using a system designed at their institution that featured a redesign of the MR bed and coil system with added computer software assistance for calculating ultrasound transducer placement; the mean x , y , and z plane errors for displaying MR additional lesion with US were 2.5 mm (range, 0.9-6.3 mm), 1.1 mm (range, 0-4 mm), and -2.6 mm (range -0.9 to 5.3 mm), respectively, with no significant clinical difference. Moreover, after applying the correction value to the initially calculated error measurement on the z -plane, the error decreased to -1.7 mm (range, -0.04 to 4.2 mm) [39]. However, in these cases the position of the radiologist was below the patient during the US examination and interventional procedures and it seems to be less practical in clinical routine or during a biopsy procedure [25]. In a recent study, Young DK et al. reported a median difference in lesion-to-nipple distance on supine and prone MRI of 8 mm (0-34 mm) in the horizontal direction and 5 mm (0-39,5 mm) in the vertical direction; in addition, thirteen lesions had a difference greater than 1 cm in both horizontal and vertical directions. No significant differences were found in both directions with respect to upper and lower locations [29].

Fausto and coworkers found good accuracy and reproducibility of volume navigation by combining US and MR images which had been both acquired in the supine position; in particular, MR was acquired in the supine position, with upper extremities extended over the head using a double synergy body coil with sensitivity encoding, covering both breasts. Breast compression was minimised using a dedicated mattress and two straps. Live US exams were performed in healthy volunteers in the supine position using a platform configured with volume navigation technique (LOGIQ E9, GE Healthcare) and a 6–15 MHz transducer with a geometry, which allows the visualisation of a wide field-of-view in both conventional and trapezoid imaging [25, 26]. The latter findings have subsequently been confirmed in another study, again conducted by Fausto and coworkers using the same technique described above, which showed that the use of second-look ultrasound with volume navigation makes it possible to objectively correlate MRI additional lesions with ultrasound appearances, showing a significant higher detection rate in comparison with conventional targeted US but without differences in the number of false positive or true positive lesions [24]. Moreover, Nakano and coworkers, who were the first to quantify the positioning error of a magnetic navigation system in breast imaging by performing MRI in the supine position, reported an overall 3D mean positioning error of approximately 12 mm, which is clinically acceptable [22]. Therefore, in light of these considerations, we can affirm that although an additional supine MR examination can be time-consuming [33], requires the use of more contrast, and reduces image quality, it has the major advantage of better correspondence with standard US and surgical position that is very helpful for both targeting and biopsy [23, 36] (Figures 2 and 3).

2.3. Accuracy and Feasibility of Second-Look with MR Coregistration: A Comparison with Conventional Targeted US. Different breast-imaging modalities offer complementary

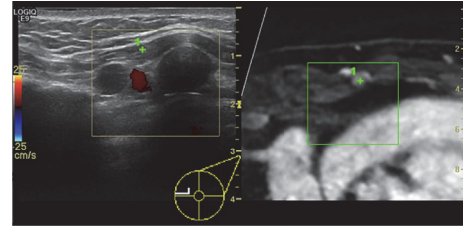


FIGURE 2: Ultrasound image (left side) with the corresponding multiplanar reconstructed MR image (right side) of a 55-year-old woman who underwent a previous surgery of the left breast for invasive ductal carcinoma (IDC, pT2N0). After 6 months, a follow-up MR was performed showing a rounded enhancing lesion in the left internal mammary chain (green cross). Second-look ultrasound with coregistration revealed a pathological lymph node.

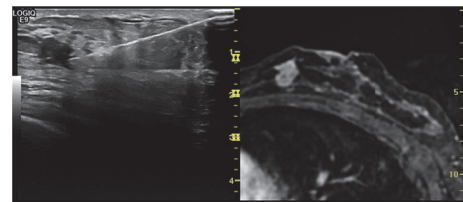


FIGURE 3: A 48-year-old woman with a previous left breast quadrantectomy (lower outer quadrant) for an invasive ductal carcinoma (IDC, pT1N0) underwent a MR follow-up 5 months after surgery that showed an additional enhancing lesion at the confluence of the inner quadrants near the nipple. Second-look ultrasound with MR coregistration confirmed the lesion which was biopsied by fine needle aspiration; the histological finding revealed an IDC.

information that can help to establish a diagnosis or assist the clinician for a therapeutic gesture [34].

In particular, the advantages of incorporating ultrasound in image fusion consist in the real-time images (which enable image-guided intervention), the lack of radiation to both patient and staff, and the possibility of comparing findings between different modalities [40].

In our research, we found 11 original papers evaluating the diagnostic performance of US-MR coregistration, published from October 2008 to October 2017, which showed that this technique may identify additional enhancing lesions with high accuracy. The first of these was a pilot study by Causer and coworkers, which was carried out to determine the accuracy of MR-US coregistration system in vivo for showing breast lesions visible on MRI and US. Both techniques were performed in the prone position, lesion pathology was determined on the basis of imaging features for cysts or histopathology for masses, and targeted lesions were displayed on the US monitor on the basis of transducer coordinates calculated from MR images. By using these methods, they found that mean lesion size correlated well ($R = 0.99$) on MR (11.4 mm; range, 6–28 mm) compared with US (10.3 mm; range, 6–28 mm) and mean error measurement on the three planes was clinically acceptable. Although results were encouraging, the small number of lesions included in the study (13) was an important limitation [39].

TABLE 1: Studies in which both conventional US and US with MR coregistration have been performed.

Authors	Number of patients with MR additional lesions	Number of MR additional lesions	US-correlate	US with MR coregistration correlate
S.Nakano 2009	17	23	7/23 (30%)	19/23 (83%)
S.Nakano 2012	51	63	42/63 (67%)	63/63 (100%)
S.Nakano 2012	55	67	18/67 (30%)	60/67 (90%)
E.P Pons 2014	148	28	3/28 (11%)	21/28 (75%)
A.Y.Park 2017	70	67	41/67(61,2%)	64/67 (95,5%)

TABLE 2: Studies in which US with MR coregistration has been only performed in order to identify US-missed MR additional lesions.

Authors	Number of patients with MR additional lesions	Number of MR additional lesions	US correlate	US- missed additional lesions detected with US with MR coregistration
A. Fausto 2012	129	207	83/207 (40%)	124/124 (100%)
T. Uematsu 2016	70	78	50/78 (64%)	24/28 (85,7%)
D.K. Kang 2017	101	119	79/119 (66,4%)	31/40 (78%)
R. Watanabe 2017	53	59	20/59 (34%)	33/39 (85%)
E. Aribal 2017	73	77	51/77 (66%)	26/26 (100%)

With regard to the other 10 more recent studies, the number of patients enrolled ranged from a minimum of 51 [22] to a maximum of 831 [29] and MRI was performed either for staging a known breast cancer only or for both staging and solving diagnostic problems. MR for coregistration was always performed in the supine position and in 6 out of 10 cases was obtained on 1.5 T equipment [21–23, 27, 29, 32] while in the other 4 on 3 T equipment [24, 28, 30, 31]. In 5 out of 10 studies all the detected additional lesions were studied with second-look US with and without MR coregistration and in one case [21] it was specified that patients had been studied with mammography, US, and MR in addition to coregistration (Table 1).

The reported detection rates of second-look with conventional US were highly variable, ranging from 30% to 61.2%, while those concerning MR coregistration were much higher, ranging from 83% to 95,5%; moreover, all enhancing lesions that were detected at second look with conventional US could be identified by using the coregistration system. Shogo Nakano et al. also showed that the overall sensitivity for detecting index tumours was 85% for mammography, 91% for US, 97% for MR, and 98% for the coregistration system (100% invasive ductal carcinomas, 100% mucinous carcinoma, and 88% ductal carcinomas in situ); notably, in one instance in which the cancer was not seen on MR, US-MR coregistration detected it with the supplementation of sonography [21].

In the other 5 studies, US and MR coregistration was only performed with the aim of identifying the MR-additional lesions not found at second look with conventional US; the reported values concerning the detection rate of US alone were in line with the previous ones and coregistration was successful in detecting US-missed additional lesions in a

high percentage of cases (detection rate from 78% to 100%) (Table 2).

Accordingly with previous studies, Elena Pastor Pons found that diagnostic performance of US-MR coregistration for identifying malignant nodules, considering overall lesions and the subgroup of ILSM, was sensitivity 96.3% and 100%, specificity 18.8% and 30.7%, positive predictive value 66.7% and 43.7%, and negative predictive value 75% and 100%, respectively; in addition, US-MR coregistration enabled biopsy of 2 metastatic lymph nodes [27].

All authors reported high rates of histological confirmation of target lesions obtained under sonography guidance, showing that US-MR coregistration is a feasible alternative to MR-guided biopsy which is time-consuming, expensive, and not widely available [17]. In particular, an important result which emerged in a recent study of Aribal et al. was that pathologic diagnoses of all malignant and high risk lesions were achieved by ultrasound guided biopsy using US-MR coregistration technique [30].

Moreover, 2 studies reported that the few added lesions with no Real-time Virtual Sonography (RVS) correlate were more benign than malignant [23, 32] and Kang DK et al. found that 2 out of 4 lesions not detected on US-MR coregistration examination disappeared, while the remaining 2 did not exhibit any change on follow-up MR [29]. Although these results require further confirmation, they suggest that US-MR coregistration could help to reduce the number of false positives thus avoiding useless biopsies.

Some authors analysed the association between US, MR and histological characteristics of target lesions and US-MR coregistration results.

In only 2 out of 10 articles it was found that US-detected lesion size during US-MR coregistration alone was

significantly smaller than that detected by conventional B-mode [22, 24]. Shogo Nakano et al. also reported that the mean tumour size provided by RVS and MRI-Multiplanar Reformation was 12.3 mm and 14.1 mm, respectively ($r = 0.848$, $p < 0.001$) [22]. Nevertheless, the results obtained in another 3 out of 10 articles regarding this parameter showed no statistically significant association [21, 23, 31]. Furthermore, an analysis again conducted by Shogo Nakano and coworkers, showed that, compared with the use of US alone, US-MR coregistration was useful in identifying lesions in patients whose diagnostic images exhibited smaller differences in echogenicity between the interior and exterior parts of the tumours, and which exhibited non-tumoral low-echo regions in the background [21].

In 2 out of 10 studies, statistically significant differences were found between some MR characteristics of US-MR coregistration detected lesions and those of undetected ones; in particular, Shogo Nakano found that identification by US-MR coregistration was more likely when the MR-detected lesions appeared as one or more foci (94%) or as a mass (89%) ($p = 0.001$, $p < 0.001$, respectively) than when lesions were described as showing non-mass-like enhancement (80%). Moreover he found that US-MR coregistration had a higher detection rate for lesions of 5 mm and those of 5-10 mm at MRI ($p = 0.001$, $p < 0.001$, respectively) and observed that lesions detected by coregistration technique alone were more likely to be found around mammary fascia (71%), whereas those identified by conventional US were more frequently found within the mammary gland (61%) ($p = 0.023$) [23]. The latter findings were in line with a recent study conducted by Park et al. which found a statistically significant difference in lesion depth between the group of US-MR coregistration detected lesions and that of US detected ones; in fact lesions of the first group tended to be located in the middle or posterior portion of breast parenchyma (78.3% [18 out of 23] for coregistration vs. 46.3% [19 out of 41] for US), whereas those of the second group tended to be located in the anterior portion of parenchyma (53.7% [22 out of 41] for US vs. 21.7% [5 out of 23] for coregistration). No significant difference in detection with conventional US and coregistration techniques was found on the basis of lesion size, distance between the nipple and the lesion, lesion shape, orientation, margin, posterior features, association with calcification or duct changes, lesion type (mass-like vs. non-mass-like lesions), and kinetic curve assessment [31]. In contrast Uematsu T et al., Kang DK et al., and Watanabe R et al. found no significant correlation between MR characteristics and lesion detection with US-MR coregistration or US alone [28, 29, 32].

Interestingly, Park AY et al. also observed that lesions detected during the coregistration technique are at increased risk of malignancy compared to conventional US (McNemar test 21 vs. 11, $P < .001$) and after second-look US, the optimal treatment plan changed in 16 of 55 (29.1%) patients; in particular, in 9 out of 16 patients (60%) the treatment plan changed because of additionally found lesions by coregistration technique [31]. Similarly, Watanabe R et al. reported that in 7 out of 53 patients (13%) surgical management was altered by US-guided biopsy of the lesions detected by coregistration technique [32].

3. Discussion

As previously discussed, the sensitivity of breast MRI for the detection of breast cancer is high, but its specificity is only moderate, ranging from 37% to 100% [16]. It is then essential to biopsy suspicious MR-detected lesions to make a definitive diagnosis [22]; MR-guided breast biopsy is gradually increasing, especially when lesions are visible on MRI but not on conventional imaging [41-43]. Nevertheless, these techniques are not widely available and require the use of expensive MR magnets, time, and personnel [21]. Furthermore, the positive predictive value of MR-guided biopsy has been reported as relatively low due to the high benignancy rate found at pathology, thus leading to a high number of unnecessary biopsy procedures even in experienced settings [25].

For these reasons, second-look targeted US has become the tool of first choice to further characterise additional MR-detected lesions.

A recent meta-analysis by Spick et al., including seventeen studies, found that lesion detection rate at second-look US was very heterogeneous ranging between 22.6% and 82.1% (pooled rate, 57.5% [1266 of 2201]; 95% confidence interval [CI]: 50.0%, 64.1% [random-effects model]; $I^2 = 90.9%$; $P < .0001$). The highest second-look US detection rates were observed for mass lesions (as opposed to non-mass lesions) and for malignant (vs. benign) lesions ($P < .001$ for both). However, they also observed that if a lesion is not visualised at second-look US, malignancy might occur in a pooled estimate of 12.2%, and therefore a negative second-look US cannot exclude malignancy [20]. Similarly, a recent review of literature which analysed sixteen original papers evaluating the diagnostic performance of breast second-look ultrasound reported that this technique makes it possible to find a correlation to MR additional lesions in 64% of cases (weighted average; SD 18%), ranging from 23% to 89%, with a probability of cancer detection at second-look ultrasound ranging from 8% to 56% (weighted average of 36%) compared with an MR-guided biopsy weighted average of 21% [24]. The success of US examination depends on several factors such as the operator's experience, breast size, findings, and lesion depth; moreover, because the operator has to perform the US-guided biopsy based only on mentally visualised positional information from the MR, there is no direct evidence that the lesion has been accurately detected and biopsied [22].

In order to overcome these problems, a new coregistration technique carrying different names depending on its vendors has recently been developed, which can synchronise the sonographic and MR images during live US [21].

Our analysis showed that the US-MR coregistration technique increases the overall accuracy of second-look US due to its higher sensitivity for additional MR-detected lesions compared with conventional US; in particular, the authors reported detection rate values ranging from 83% to 100% and some of them found that RVS was successful in detecting additional lesions blinded at US in an high percentage of cases (detection rate from 60% to 100%). Another important advantage is that US-MR coregistration is an easy-to-use tool that is well-integrated in US equipment and could be a way to

reduce operator-dependency of US when lesion displacement due to different position of the patient has a fundamental impact on detection [24].

In addition, although further confirmation is needed, the results obtained by some authors suggested that the US-MR coregistration technique could improve the identification of high risk and malignant lesions and could also be helpful in detecting suspicious lymph nodes [33]; this means that this technique may significantly reduce the number of MR-guided biopsies enabling operators to select cases that really require it and to choose the most appropriate treatment plan for each patient. Nevertheless, there are some technical limitations which have to be taken into account: first of all, pressure applied to the probe may alter the depth of lesions and distort anatomic landmarks depicted by MRI, especially during interventional procedures; it is thus necessary to conduct the operation gently, avoiding the application of excessive pressure on breast tissue [30]; secondly, although the US-MR coregistration technique enables the identification of deep lesions which are often missed on conventional US [23, 31], the patient has to maintain the supine position that may hide the lesions localised in the lateral portions of the breast and hinders US-guided biopsy of peripheral lesions [30].

Accurate localisation is also essential for adequate surgical removal of breast tumours, in which an optimal balance between good cosmetic results and preservation of resection margins is the primary goal [44]. Some studies have been conducted in order to investigate the feasibility of the US-MR coregistration to demarcate breast cancer. Anderliesten et al. reported that image-guided coregistration to demarcate breast cancer, on the basis of preacquired MR images, in a supine orientation, appears feasible if patient's breath is tracked during the navigation procedure, positional uncertainty is visualised, and pressure on the location instrument is released after the verification of its position [45]. Moreover, Chang et al. found that the tumour size, estimated by US-MR coregistration technique, was more strongly correlated with the histological one than with US alone; measurement of the lesions by US-MR coregistration technique was significantly more accurate for mass type lesions detected on MRI. In addition, accurate measurement of mass extent was improved with the US-MR coregistration technique, compared with US alone, in patients who had non-mass type lesions on MRI and who had undergone neoadjuvant systemic chemotherapy [44]. In light of these considerations, we could assume that if these findings will be further confirmed, US-MR coregistration technique may become an important tool not only for second-look US, but also for surgical planning.

Limitations of volume navigation technique are associated with errors in coregistration of MR dataset and live US because it is primarily based on the assumption that the structures within the data volume (i.e., the body part studied) have fixed positions, relative to each other, in the two different imaging modalities [46].

Nevertheless, as previously noted, breast tissues are soft and easily deformable so that they can undergo relevant modifications from prone to supine position, thus causing discrepancies and misalignment in coregistration. Compensation algorithms for such causes of misalignment have been

proposed, but they are still limited in medical applications because of the complex physical properties of tissues [46]. Another important factor which may reduce the effectiveness of US-MR coregistration is breast hypertrophy. In patients with high breast volume, the transition from the prone to the supine position determines a large variability of tissue placement and possibility of dislocation. Using two anthropomorphic measurements as suggested by Sigurdson, a good selection of subjects can be made [47]. Actually, this method enables a precise determination of breast volume, thus helping operators to select patients who need MR-guided biopsy, especially if the additional lesion is localised at the external quadrants and far from the skin. Eventually an additional supine MRI may be used to obtain a better MR-US match of the lesion since US is performed with the patient in the supine position too [28]. Moreover the supine position allows an accurate preoperative planning since the patient is analysed in the same position adopted on the operating table [23]. However this approach has several disadvantages: first of all, image quality is lower compared with prone MRI due to respiratory or heartbeats artefacts and to the use of nondedicated coils [22, 25, 30]; secondly, an additional MRI examination in the supine position is time-consuming, requires additional administration of contrast agent, or may be unavailable [33].

On the other hand several authors did not find significant misalignment of the lesions on the three axes using standard US-MR coregistration, demonstrating that this technique is accurate and feasible even to locate lesions within a limited volume [22, 25, 29, 46].

4. Conclusions

In light of these considerations, we can affirm that US-MR coregistration technique is an accurate and feasible imaging technique which can significantly increase both the detection rate of additional enhancing lesions of the breast and the number of US-guided interventional procedures, which are preferable to MR-guided ones. Moreover, it is easier to perform, much less operator-dependent, and also comfortable for the patient because it does not require radiation and additional preparation. Although further studies are needed in order to confirm these findings and to overcome technical limitations, results are encouraging and suggest that US-MR coregistration technique may become an important tool for second look which could also help operators to choose the most adequate treatment plan and patient management.

Conflicts of Interest

None of the authors has any conflicts of interest to report.

Authors' Contributions

All the authors contributed equally to this work; M. A. Mazzei, F. Gentili, A. Fausto, L. Volterrani, F. G. Mazzei, and L. Di Giacomo contributed to conception, design, and critical revision of this article; L. Di Giacomo, A. Fausto,

M. A. Mazzei, and F. Gentili contributed to analysis and interpretation of the data and drafting of the article; all the authors gave final approval of the version to be published.

References

- [1] S. G. Orel and M. D. Schnall, "MR imaging of the breast for the detection, diagnosis, and staging of breast cancer," *Radiology*, vol. 220, no. 1, pp. 13–30, 2001.
- [2] S. E. Harms and D. P. Flamig, "Breast MRI," *Clinical Imaging*, vol. 25, no. 4, pp. 227–246, 2001.
- [3] W. A. Berg, "Overview of breast imaging," *Seminars in Roentgenology*, vol. 36, no. 3, pp. 180–186, 2001.
- [4] S. G. Orel, "MR imaging of the breast," *Magnetic Resonance Imaging Clinics of North America*, vol. 9, no. 2, pp. 273–288, 2001.
- [5] C. K. Kuhl, "Current status of breast MR imaging: Part 2. Clinical applications," *Radiology*, vol. 244, no. 3, pp. 672–691, 2007.
- [6] G. L. G. Menezes, F. M. Knuttel, B. L. Stehouwer, R. M. Pijnappel, and M. A. A. J. Van Den Bosch, "Magnetic resonance imaging in breast cancer: A literature review and future perspectives," *World Journal of Clinical Oncology*, vol. 5, no. 2, pp. 61–70, 2014.
- [7] M. M. Tilanus-Linthorst, I. M. Obdeijn, K. C. Bartels, H. J. de Koning, and M. Oudkerk, "First experiences in screening women at high risk for breast cancer with MR imaging," *Breast Cancer Research and Treatment*, vol. 63, no. 1, pp. 53–60, 2000.
- [8] F. Podo, F. Sardaneli, R. Canese, and G. Dagnolo, "The Italian multi-centre project on evaluation of MRI and other imaging modalities in early detection of breast cancer in subjects at high genetic risk," *Journal of Experimental & Clinical Cancer Research*, vol. 21, pp. 115–124, 2002.
- [9] E. A. Morris, L. Liberman, D. J. Ballon et al., "MRI of occult breast carcinoma in a high-risk population," *American Journal of Roentgenology*, vol. 181, no. 3, pp. 619–626, 2003.
- [10] M. Kriege, C. T. M. Brekelmans, C. Boetes et al., "Efficacy of MRI and mammography for breast-cancer screening in women with a familial or genetic predisposition," *The New England Journal of Medicine*, vol. 351, no. 5, pp. 427–519, 2004.
- [11] E. Warner, D. B. Plewes, K. A. Hill et al., "Surveillance of BRCA1 and BRCA2 mutation carriers with magnetic resonance imaging, ultrasound, mammography, and clinical breast examination," *Journal of the American Medical Association*, vol. 292, no. 11, pp. 1317–1325, 2004.
- [12] C. K. Kuhl, S. Schradang, C. C. Leutner et al., "Mammography, breast ultrasound, and magnetic resonance imaging for surveillance of women at high familial risk for breast cancer," *Journal of Clinical Oncology*, vol. 23, no. 33, pp. 8469–8476, 2005.
- [13] M. O. Leach, "Screening with magnetic resonance imaging and mammography of a UK population at high familial risk of breast cancer: A prospective multicentre cohort study (MARIBS)," *The Lancet*, vol. 365, no. 9473, pp. 1769–1778, 2005.
- [14] C. D. Lehman, J. D. Blume, P. Weatherall et al., "Screening women at high risk for breast cancer with mammography and magnetic resonance imaging," *Cancer*, vol. 103, no. 9, pp. 1898–1905, 2005.
- [15] C. D. Lehman, C. Isaacs, M. D. Schnall et al., "Cancer yield of mammography, MR, and US in high-risk women: prospective multi-institution breast cancer screening study," *Radiology*, vol. 244, no. 2, pp. 381–388, 2007.
- [16] C. Wiratkapun, D. Duke, A. S. Nordmann et al., "Indeterminate or suspicious breast lesions detected initially with mr imaging. Value of MRI-directed breast ultrasound," *Academic Radiology*, vol. 15, no. 5, pp. 618–625, 2008.
- [17] M. J. Hong, J. H. Cha, H. H. Kim et al., "Second-look ultrasonography for MRI-detected suspicious breast lesions in patients with breast cancer," *Ultrasonography*, vol. 34, no. 2, pp. 125–132, 2015.
- [18] H. Abe, R. A. Schmidt, R. N. Shah et al., "MR-directed ('second-look') ultrasound examination for breast lesions detected initially on MRI: MR and sonographic findings," *American Journal of Roentgenology*, vol. 194, no. 2, pp. 370–377, 2010.
- [19] J. H. Youk, E. Kim, M. J. Kim, J. Y. Lee, and K. K. Oh, "Missed breast cancers at US-guided core needle biopsy: how to reduce them," *RadioGraphics*, vol. 27, no. 1, pp. 79–94, 2007.
- [20] C. Spick and P. A. T. Baltzer, "Diagnostic utility of second-look US for breast lesions identified at MR imaging: Systematic review and meta-analysis," *Radiology*, vol. 273, no. 2, pp. 401–409, 2014.
- [21] S. Nakano, M. Yoshida, K. Fujii et al., "Fusion of MRI and sonography image for breast cancer evaluation using real-time virtual sonography with magnetic navigation: First experience," *Japanese Journal of Clinical Oncology*, vol. 39, no. 9, pp. 552–559, 2009.
- [22] S. Nakano, M. Yoshida, K. Fujii et al., "Real-time virtual sonography, a coordinated sonography and MRI system that uses magnetic navigation, improves the sonographic identification of enhancing lesions on breast MRI," *Ultrasound in Medicine & Biology*, vol. 38, no. 1, pp. 42–49, 2012.
- [23] S. Nakano, J. Kousaka, K. Fujii et al., "Impact of real-time virtual sonography, a coordinated sonography and MRI system that uses an image fusion technique, on the sonographic evaluation of MRI-detected lesions of the breast in second-look sonography," *Breast Cancer Research and Treatment*, vol. 134, no. 3, pp. 1179–1188, 2012.
- [24] A. Fausto, D. Casella, L. Mantovani, G. Giacalone, and L. Volterrani, "Clinical value of second-look ultrasound: Is there a way to make it objective?" *European Journal of Radiology*, vol. 81, no. 1, pp. S36–S40, 2012.
- [25] A. Fausto, G. Rizzato, A. Preziosa et al., "A new method to combine contrast-enhanced magnetic resonance imaging during live ultrasound of the breast using volume navigation technique: A study for evaluating feasibility, accuracy and reproducibility in healthy volunteers," *European Journal of Radiology*, vol. 81, no. 3, pp. e332–e337, 2012.
- [26] Fausto et al., "Six-year prospective evaluation of second-look US with volume navigation for MRI-detected additional breast lesions," *European Radiology*, <https://www.editorialmanager.com/eura/Default.aspx?pg=login.asp&username=>>.
- [27] E. P. Pons, F. M. Azcón, M. C. Casas, S. M. Meca, and J. L. G. Espona, "Real-time MRI navigated US: Role in diagnosis and guided biopsy of incidental breast lesions and axillary lymph nodes detected on breast MRI but not on second look US," *European Journal of Radiology*, vol. 83, no. 6, pp. 942–950, 2014.
- [28] T. Uematsu, K. Takahashi, S. Nishimura et al., "Real-time virtual sonography examination and biopsy for suspicious breast lesions identified on MRI alone," *European Radiology*, vol. 26, no. 4, pp. 1064–1072, 2016.
- [29] D. K. Kang, Y. Jung, S. Han, J. Y. Kim, and T. H. Kim, "Clinical utility of real-time MR-navigated ultrasound with supine breast

- MRI for suspicious enhancing lesions not identified on second-look ultrasound,” *Ultrasound in Medicine & Biology*, vol. 43, no. 2, pp. 412–420, 2017.
- [30] E. Aribal, D. Tureli, F. Kucukkaya, and H. Kaya, “Volume navigation technique for ultrasound-guided biopsy of breast lesions detected only at MRI,” *American Journal of Roentgenology*, vol. 208, no. 6, pp. 1400–1409, 2017.
- [31] A. Y. Park, B. K. Seo, H. Han et al., “Clinical value of real-time ultrasonography-MRI fusion imaging for second-look examination in preoperative breast cancer patients: additional lesion detection and treatment planning,” *Clinical Breast Cancer*, vol. 18, no. 4, pp. 261–269, 2018.
- [32] R. Watanabe, T. Ando, M. Osawa et al., “Second-look US using real-time virtual sonography, a coordinated breast US and MRI system with electromagnetic tracking technology: a pilot study,” *Ultrasound in Medicine & Biology*, vol. 43, no. 10, pp. 2362–2371, 2017.
- [33] A. Y. Park and B. K. Seo, “Real-time MRI navigated ultrasound for preoperative tumor evaluation in breast cancer patients: Technique and clinical implementation,” *Korean Journal of Radiology*, vol. 17, no. 5, pp. 695–705, 2016.
- [34] Y. Guo, R. Sivaramakrishna, C. Lu, J. S. Suri, and S. Laxminarayan, “Breast image registration techniques: a survey,” *Medical & Biological Engineering & Computing*, vol. 44, no. 1-2, pp. 15–26, 2006.
- [35] V. Rajagopal, A. Lee, J.-H. Chung et al., “Creating individual-specific biomechanical models of the breast for medical image analysis,” *Academic Radiology*, vol. 15, no. 11, pp. 1425–1436, 2008.
- [36] G. Rizzatto and A. Fausto, “Breast imaging and volume navigation: MR imaging and ultrasound coregistration,” *Ultrasound Clinics*, vol. 4, no. 3, pp. 261–271, 2009.
- [37] P. Siegler, C. M. B. Holloway, P. Causer, G. Thevathasan, and D. B. Plewes, “Supine breast MRI,” *Journal of Magnetic Resonance Imaging*, vol. 34, no. 5, pp. 1212–1217, 2011.
- [38] C. A. Piron, P. Causer, R. Jong, R. Shumak, and D. B. Plewes, “A hybrid breast biopsy system combining ultrasound and MRI,” *IEEE Transactions on Medical Imaging*, vol. 22, no. 9, pp. 1100–1110, 2003.
- [39] P. A. Causer, C. A. Piron, R. A. Jong, and D. B. Plewes, “Preliminary in vivo validation of a dedicated breast MRI and sonographic coregistration imaging system,” *American Journal of Roentgenology*, vol. 191, no. 4, pp. 1203–1207, 2008.
- [40] C. Ewertsen, A. Săftoiu, L. G. Gruionu, S. Karstrup, and M. B. Nielsen, “Real-time image fusion involving diagnostic ultrasound,” *American Journal of Roentgenology*, vol. 200, no. 3, pp. W249–W255, 2013.
- [41] F. G. Mazzei, F. Gentili, S. Guerrini et al., “MR lymphangiography: a practical guide to perform it and a brief review of the literature from a technical point of view,” *BioMed Research International*, vol. 2017, Article ID 2598358, 8 pages, 2017.
- [42] P. Gennaro, A. Borghini, G. Chisci et al., “Could MRI visualize the invisible? An Italian single center study comparing magnetic resonance lymphography (MRL), super microsurgery and histology in the identification of lymphatic vessels,” *European Review for Medical and Pharmacological Sciences*, vol. 21, no. 4, pp. 687–694, 2017.
- [43] M. A. Mazzei, F. Gentili, F. G. Mazzei et al., “High-resolution MR lymphangiography for planning lymphaticovenous anastomosis treatment: a single-centre experience,” *La Radiologia Medica*, vol. 122, no. 12, pp. 918–927, 2017.
- [44] W. K. Moon, J. M. Chang, W. Han et al., “Evaluation of tumor extent in breast cancer patients using real-time MR navigated ultrasound: Preliminary study,” *European Journal of Radiology*, vol. 81, no. 11, pp. 3208–3215, 2012.
- [45] T. Alderliesten, C. Loo, A. Paape et al., “On the feasibility of MRI-guided navigation to demarcate breast cancer for breast-conserving surgery,” *Medical Physics*, vol. 37, no. 6, pp. 2617–2626, 2010.
- [46] F. Kucukkaya, E. Aribal, D. Tureli, H. Altas, and H. Kaya, “Use of a volume navigation technique for combining real-time ultrasound and contrast-enhanced MRI: Accuracy and feasibility of a novel technique for locating breast lesions,” *American Journal of Roentgenology*, vol. 206, no. 1, pp. 217–225, 2016.
- [47] L. J. Sigurdson and S. A. Kirkland, “Breast volume determination in breast hypertrophy: An accurate method using two anthropomorphic measurements,” *Plastic and Reconstructive Surgery*, vol. 118, no. 2, pp. 313–320, 2006.

Review Article

A New Challenge for Radiologists: Radiomics in Breast Cancer

Paola Crivelli ¹, **Roberta Eufrasia Ledda**,²
Nicola Parascandolo ², **Alberto Fara** ², **Daniela Soro**,² and **Maurizio Conti**²

¹Department of Biomedical Sciences, Institute of Radiological Sciences, University of Sassari, Sassari, Italy

²Department of Clinical and Experimental Medicine, Institute of Radiological Sciences, University of Sassari, Sassari, Italy

Correspondence should be addressed to Paola Crivelli; paocri2000@gmail.com

Received 10 January 2018; Revised 24 August 2018; Accepted 9 September 2018; Published 8 October 2018

Guest Editor: Graziella Di Grezia

Copyright © 2018 Paola Crivelli et al. This is an open access article distributed under the Creative Commons Attribution License, which permits unrestricted use, distribution, and reproduction in any medium, provided the original work is properly cited.

Introduction. Over the last decade, the field of medical imaging experienced an exponential growth, leading to the development of radiomics, with which innumerable quantitative features are obtained from digital medical images, providing a comprehensive characterization of the tumor. This review aims to assess the role of this emerging diagnostic tool in breast cancer, focusing on the ability of radiomics to predict malignancy, response to neoadjuvant chemotherapy, prognostic factors, molecular subtypes, and risk of recurrence. *Evidence Acquisition.* A literature search on PubMed and on Cochrane database websites to retrieve English-written systematic reviews, review articles, meta-analyses, and randomized clinical trials published from August 2013 up to July 2018 was carried out. *Results.* Twenty papers (19 retrospective and 1 prospective studies) conducted with different conventional imaging modalities were included. *Discussion.* The integration of quantitative information with clinical, histological, and genomic data could enable clinicians to provide personalized treatments for breast cancer patients. Current limitations of a routinely application of radiomics are represented by the limited knowledge of its basics concepts among radiologists and by the lack of efficient and standardized systems of feature extraction and data sharing.

1. Introduction

Breast cancer is the most commonly diagnosed cancer and the second leading cause of death for cancer among women worldwide [1]. The prediction of response to treatment and of prognosis is essential in clinical practice in the era of precision medicine [2]. In the past decade, oncologists and radiologists have been showing an increasing interest for the clinical utility of quantitative imaging, encouraged by the significant advancements within the field of medical images analysis. This exponential growth led to the development of radiomics, with which innumerable quantitative features are extracted from digital medical images, usually tomographic, through a high-throughput computing. These features, relating to tumor size, shape, intensity, and texture, provide a comprehensive tumor characterization, defining what it has been called the radiomics signature of the tumor [3]. Radiomics is based on the central hypothesis that extracted quantitative data reflect mechanisms occurring at genetic and molecular levels [4]. Radiomics is a complex process that

involves several steps. It begins with acquisition of high-quality images, from which a region of interest (ROI) is identified and segmented either manually or automatically. The ROI can include the whole tumor or some parts of it. Once the segmentation is completed, the selected regions are rendered in three dimensions, becoming volumes. Dedicated software [5–7] then extract quantitative features from the obtained volumes to produce a report, which is inserted into a database and integrated with other data (clinical information, genomic profiles, serum markers, and/or histology data) to be shared across different centers or institutions [3, 8] (Figure 1). A radiomics methodology was first applied to neck and lung cancer imaging [9–11] and more recently to breast imaging [12]. Radiomics seems able to offer imaging biomarkers useful not just to diagnose breast cancer but also to predict treatment response and risk of recurrence. With regard to breast cancer, a radiomics approach has been investigated mainly with Magnetic Resonance Imaging (MRI). However, some studies appearing more recently have explored the potential of radiomics with different imaging modalities:

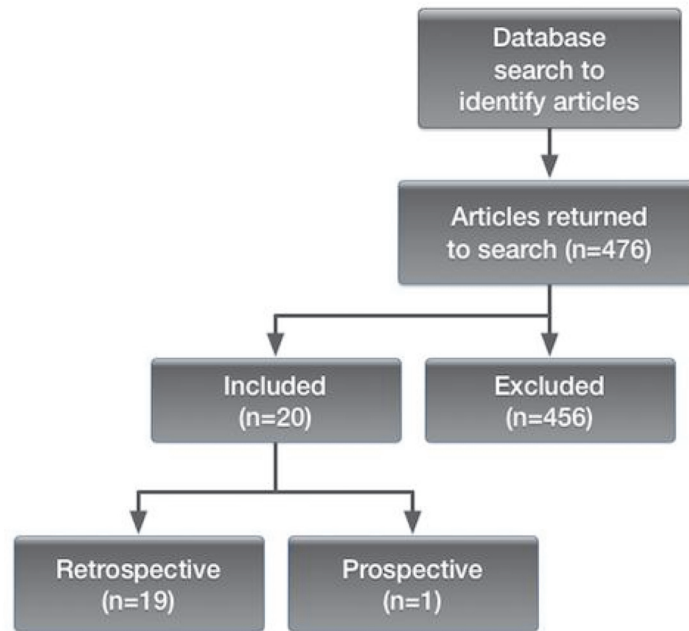


FIGURE 1

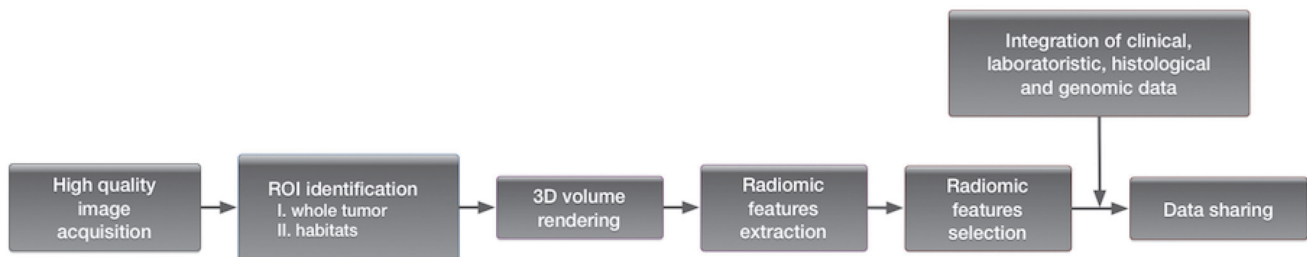


FIGURE 2

standard mammography, digital breast tomosynthesis (DBT), and ultrasound (US). Aim of this review is to explore the current and potential role of radiomics in breast cancer, focusing on the ability of radiomics to predict malignancy, response to neoadjuvant chemotherapy (NAC), prognostic factors, molecular subtypes, and risk of recurrence.

2. Methods and Materials

We referred to PubMed and the Cochrane review database websites to retrieve English-written relevant articles (abstract and/or full-text). Systematic reviews, review articles, meta-analyses, and randomized clinical trials (published from August 2013 up to July 2018) were considered. Keywords typed for our search were as the following: breast cancer and radiomics, breast MRI and radiomics, breast mammography and radiomics, breast tomosynthesis and radiomics, breast ultrasound and radiomics, breast neoplasia and radiomics, breast lesion and radiomics, breast eteroplasia and radiomics, breast MRI and texture analysis, breast MRI and quantitative analysis, breast mammography and texture analysis, breast

mammography and quantitative analysis, breast tomosynthesis and texture analysis, breast tomosynthesis and quantitative analysis, breast ultrasound and texture analysis, and breast ultrasound and quantitative analysis. To increase the inclusiveness of our search strategy, we also referred to texts to find other relevant cited manuscripts not retrieved in our initial search. Given the narrative nature of this review, no formal quality assessment was done.

3. Results

The search on PubMed and on Cochrane databases produced a total of 476 articles; non-English papers, duplicates, case reports, comments, letters, articles that did not considered breast cancer specifically, irrelevant studies, inappropriate data, and comparisons were excluded. All articles presenting quantitative studies but not purely radiomics were excluded as well as those on nuclear medicine imaging. All retro- and prospective original articles that investigated the application of radiomics to breast cancer were included. Twenty papers, 19 retrospective and 1 prospective studies, were selected (Figure 2; Table 1).

TABLE 1: Specifications of radiomics studies included in this narrative review.

Reference	Study design	Patients (No)	Diagnostic modality	Radiomics imaging features selected (No)	Prediction	Sensitivity (%)	Specificity (%)	Accuracy (%)	AUC
Parekh et al. (2017) [13]	Retrospective	124	MRI (3T)	690 (RFMs)	Malignancy	93	85		
Whitney et al. (2018) [14]	Retrospective	508	MRI (1.5 and 3 T)	38	Malignancy				0.846 (including size features) 0.848 (excluding size features)
Bickelhaupt et al. (2017) [15]	Retrospective	50	MRI (1.5 T)	188	Malignancy				0.842-0.851
Bickelhaupt et al. (2018) [16]	Retrospective	222	MRI (1.5 T)	359	Malignancy	98.4	69.7		
Zhang et al. (2017) [17]	Retrospective	117	US	364	Malignancy	85.7	89.3		
Tagliafico et al. (2018) [18]	Prospective	20	Mammography (DBT)	104	Malignancy				0.567
Braman et al. (2017) [19]	Retrospective	117	MRI (1.5 and 3 T)	99	NAC				0.78 (training dataset) 0.74 (independent testing set) 0.83 (HR+, HER2-) 0.93 (TN/HER2+) 0.847 (training set; model 10 T2-fat suppression) 0.770 (validation set; model 10 T2-fat suppression) 0.847 (training set; model 8 DWI) 0.787 (validation set; model 8) 0.863 (training set; model 10 joint T2-fat suppression/DWI) 0.805 (validation set; model 10 joint T2-fat suppression/DWI)
Obeid et al. (2016) [21]	Retrospective	63	MRI (1.5 and 3 T)	13	Prognostic factors				-

TABLE I: Continued.

Reference	Study design	Patients (No)	Diagnostic modality	Radiomics		Prediction	Sensitivity (%)	Specificity (%)	Accuracy (%)	AUC
				imaging features selected (No)	(No)					
Ma et al. (2018)[22]	Retrospective	377	MRI (3 T)	56		Prognostic factors	77.7	76.9	0.757	0.773
Liang et al. (2018)[23]	Retrospective	318	MRI (1.5 T)	30		Prognostic factors				0.762 (training dataset) 0.740 (validation dataset)
Guo et al. (2015)[24]	Retrospective	91	MRI (1.5 T)	38		Molecular subtypes				0.877 (stage) * 0.693 (lymph node) * 0.789 (ER) * 0.689 (PR) * 0.641 (HER2) *
Li et al. (2016) [4]	Retrospective	91	MRI (1.5 T)	38		Molecular subtypes				0.89 (ER+ vs ER-) 0.69 (PR+ vs PR-) 0.65 (HER+ vs HER2-) 0.67 TN vs others)
Wang et al. (2015) [25]	Retrospective	84	MRI (3 T)	85		Molecular subtypes	57.0 (TN vs others) ** 62.0 (TN vs ER+) ** 53.0 (TN vs PR+) ** 49.5 (TN vs LumA) ** 69.5 (TN vs LumB) **	94.7 (TN vs others) ** 93.6 (TN vs ER+) ** 94.1 (TN vs PR+) ** 89.8 (TN vs LumA) ** 90.0 (TN vs LumB) **	90.0 (TN vs others) ** 89.4 (TN vs ER+) ** 87.8 (TN vs PR+) ** 81.8 (TN vs LumA) ** 84.3 (TN vs LumB) **	0.878 (TN vs others) ** 0.883 (TN vs ER+) ** 0.859 (TN vs PR+) ** 0.814 (TN vs LumA) ** 0.789 (TN vs LumB) **
Fan et al. (2017)[26]	Retrospective	60	MRI (1.5 T)	88		Molecular subtypes	88.2 (LumA) 86.5 (LumB) 81.1 (HER2) 81.1 (basal-like)	76.9 (LumA) 62.5 (LumB) 100 (HER2) 100 (basal-like)		0.867 (LumA) 0.786 (LumB) 0.888 (HER2) 0.923 (basal-like)
Guo et al. (2017)[27]	Retrospective	215	US	463		Molecular subtypes				0.760
Ma et al. (2018)[28]	Retrospective	331	Mammography	39		Molecular subtypes				0.865 (TN vs non TN) 0.784 (HER2 vs non HER2) 0.752 (Lum vs non-Lum)
Li et al. (2016) [29]	Retrospective	84	MRI (1.5 and 3T)	38		Recurrence				0.88 (MammaPrint) 0.76 (Oncotype DX) 0.68 (PAM50 risk of relapse based on subtype) 0.55 (PAM50 risk of relapse based on subtype and proliferation)

TABLE I: Continued.

Reference	Study design	Patients (No)	Diagnostic modality	Radiomics imaging features selected (No)	Prediction	Sensitivity (%)	Specificity (%)	Accuracy (%)	AUC
Park et al. (2018)[30]	Retrospective	294	MRI (1.5 T)	156	Recurrence	-	-	-	-
Drukker et al. (2018)[31]	Retrospective	162	MRI (1.5 T)	1	Recurrence	-	-	-	-

(i) * AUC considering only radiomics models.

(ii) ** Considering both tumor and BPE features.

4. Radiomics and Malignancy

Several studies have investigated the usefulness and reliability of radiomics to discriminate benign breast lesions from cancers, demonstrating that its application might improve the radiologist confidence in the challenging diagnostic task.

4.1. MRI. Parekh and Jacobs [13], aiming to find a correlation between radiomics features and different breast tissues of interest, generated radiomics feature maps (RFMs) for visualization and evaluation of radiological images. The radiomics features were then correlated to different breast tissues and compared with quantitative values of radiological parameters. Malignant lesions showed higher values of entropy and the entropy RFM was the most reliable to distinguish malignant from benign lesions, reflecting the tumor heterogeneity and its vascular status. Whitney et al. proposed a radiomics method to investigate whether a set of quantitative features extracted from MR images might help to distinguish luminal A breast cancers from benign breast lesions, compared to using maximum linear size alone [14]. They retrospectively analyzed dynamic contrast-enhanced- (DCE-) MRI of 508 breast lesions and extracted 38 features, which were used to design three different classification protocols. The area under the curve (AUC) for maximum linear size alone was 0.797 in comparison to 0.846 and 0.848 for feature selection protocols including and excluding size features, respectively. Thus, the protocol excluding features related to size was statistically equivalent to that including all features in the ability to distinguish the two pathological entities. The radiomics feature of irregularity was found to play an important role in the feature selection process. In 2017, a retrospective study aimed to establish a potential ability of radiomics to determine the malignant nature of suspicious breast lesions detected on screening X-ray mammography [15]. Supported by emerging evidences on the accuracy of contrast-free breast MRI protocols in the detection of malignant breast lesions [32–34], they employed a radiomics methodology on two contrast-free MRI sequences: Diffusion Weighted Imaging (DWI) and T2-weighted sequences. Two radiomics classifiers allowed distinguishing benign from malignant lesions more accurately (AUC of 0.842–0.851) than the mean apparent diffusion coefficient (ADC) parameter alone (AUC of 0.774), proposed by Bogner et al. with the same scope [35]. However, the inclusion of the mean ADC parameter increased the accuracy of the model, demonstrating the advantages of taking into account previous results and, implicitly, of data sharing. Nevertheless, the performance of the proposed model was lower than that of expert breast radiologists (AUC of 0.959), suggesting that the potential of radiomics in prediction of malignant lesions has to be better assessed. Unenhanced sequences were also used by Bickelhaupt et al., who conducted a multicentric and prospective study to evaluate a radiomics model of suspicious breast lesions (BI-RADS 4 and 5) extracted from breast-tissue-optimized kurtosis MRI by two different vendors to differentiate benign from malignant lesions. The proposed model, evaluated in an independent test set, showed reliable results [16].

4.2. US and DBT. A radiomics approach on US imaging and specifically on sonoelastograms was proposed by Zhang in 2017, showing that some sonoelastomic features might help to discriminate between benign and malignant breast tumors [17]. A multicentric and prospective study applied a radiomics approach to DBT for the first time in order to differentiate normal breast tissue from malignant breast tissue in patients with dense breasts [18]. Twenty patients with negative standard mammography who had had a DBT-detected and histology-proven breast cancer were enrolled. Further 20 patients of similar age and breast density with negative DBT and US served as a control group. From 104 radiomics features extracted, 3 (skewness, entropy, and 90 percentile) were found to differ significantly between the two groups. Results also revealed that energy, entropy, and dissimilarity correlated significantly with tumor size and entropy with receptor status too. Despite the small patient sample and the biased selection of features, almost inevitably based on MRI, these preliminary results are encouraging, suggesting that a radiomics analysis of DBT images can be used to facilitate cancer detection and for a better characterization of the detected lesion.

5. Radiomics and Neoadjuvant Chemotherapy

NAC, administered before surgery to reduce tumor size and the risk of distant metastases, is often the first line treatment for those patients diagnosed with locally advanced breast cancer [36]. However, less than 50% of patients achieve a pathological complete response (pCR) [37, 38]. A retrospective study published by Braman et al. explored the ability of radiomics to predict pCR to NAC [19], analyzing 99 textural features extracted from the intratumoral and peritumoral regions of T1-weighted contrast-enhanced MRI scans. Authors concluded that radiomics might successfully be employed for the purpose, even more effectively if peritumoral regions are included into the analysis and the receptor status considered.

6. Radiomics and Prognostic Factors

6.1. Lymph Node Metastases. Determining the axillary lymph node status remains a mandatory requirement of the diagnostic process. In 2017, Dong et al. proposed an optimal multivariable radiomics model able to predict sentinel lymph node (SLN) metastases [20], finding that radiomics features extracted from DWI sequences showed higher correlation with SLN metastases than those extracted from ADC mapping. These results, which certainly need further validation, might help in clinical decision-making with respect to axillary surgery, potentially avoiding invasive procedures in patients at a low risk of SLN metastases.

6.2. Peritumoral Fat. Over the decades, numerous studies have demonstrated that obesity is associated with increased incidence and mortality from different forms of cancer, including breast cancer [39, 40]. A retrospective study conducted by Obeid et al. investigated the prognostic impact of peritumoral fat in early breast cancers (T1 and T2 stages)

[21]. Authors found a significant linking between a specific peritumoral fat feature, extracted from preoperative MRI sequences and axillary node metastases in patients with body mass index greater than 30. Despite the small sample size of patients, results suggest that a radiomics evaluation of the peritumoral fat might provide valuable noninvasive prognostic data.

6.3. Ki67. Ki67 labeling index is routinely used as a prognostic marker in breast cancer patients, to estimate both cell proliferation and therapeutic response [41, 42]. A retrospective study including 377 women diagnosed with invasive breast cancer investigated the possibility of predicting the proliferation marker Ki67 expression through a radiomics approach [22]. Three machine learning schemes were employed to classify cancers in to low- and high-Ki67 expression lesions. Following a semiautomatic segmentation on DCE-MRI, 56 radiomics features (morphological, greyscale statistic, and texture ones) were extracted. Results showed that some of the morphologic features such as perimeter, values of area, and diameter tend to have low values in low-Ki67 tumors, being the high expression of Ki67 associated with a high proliferation rate. Overall, 3 texture features (contrast, entropy, and line likeness) were significantly associated with the Ki67 expression. Liang et al. proposed a new, noninvasive Ki-67 predictor status based on breast MRI [23]. They retrospectively analyzed 318 MRI of breast cancer patients (200 for the training dataset and 118 for the validation dataset), whose Ki67 status was known. Authors selected 30 features and composed a Rad-score for each patient following the analysis of the unenhanced T2-weighted fat suppression sequences and the enhanced T1-weighted. Rad-score calculated on T2-weighted images was significantly associated with Ki67 status, in both training and validation datasets, whereas Rad-score on enhanced T1-weighted did not show correlation with Ki67 expression in the validation cases. These results suggest that a new radiomics marker, obtained with routinely performed unenhanced MRI sequence, might preoperatively predict Ki67 expression in breast cancer.

7. Radiomics and Molecular Subtypes

Numerous studies have proposed a radiomics approach to predict breast cancers molecular profile, whose definition is essential to establish the best patient management [43]. Furthermore, the integration between radiomics and genomic features, known as radiogenomics, has revealed promising results in oncology, providing opportunities to better understand tumors behavior and thus to improve diagnosis and prognosis [9, 44].

7.1. MRI. In 2015, Guo et al. explored the relationship between radiogenomics features and clinical variables such tumor stage, lymph node metastases and molecular receptor status (estrogen receptor, ER, status; progesterone receptor, PR, status; and human epidermal growth factor receptor-2, HER2, status) [24]. Ninety-one cases of invasive

breast carcinomas were included into the analysis. Thirty-eight radiomics features (related to size, shape, morphology, enhancement texture, kinetics, and variance kinetics), extracted from DCE-MRI, were correlated to 144 genomic features for 70 genes (70 gene expression features, 70 copy number features and 4 methylation features). Results showed a significant positive association between all tumor size features and tumor stage, as well as between tumor irregularity and tumor stage, meaning that high-stage tumors tend to be larger and more irregular. Several genomic features were found to be significantly associated with molecular receptor status, whereas no single radiomics feature showed a significant association with ER, PR and/or HER status. Conversely, no isolated genomic features showed a positive correlation with tumor stage and lymph node status. The radiomics feature that correlated the most with the tumor stage was the effective diameter, while the Aurora kinase B gene, AURKB (GE), represented the most useful genomic feature to predict the ER status. However, the model combining radiomics and genomic features showed no higher accuracy in the prediction of invasive breast carcinomas clinical phenotypes in comparison to those considering radiomics and genomic features independently, likely due to the small number of patients enrolled. A retrospective study published in 2016 explored the correlation between quantitative features and cancer receptors status (ER+, ER-, PR+, PR-, HER2+, HER2-, and triple negative, TN) [4]. It was demonstrated that MR image-based tumor phenotypes are significantly associated with receptor status and that heterogeneity is an important feature to discriminate different subtypes, of which, in the near future, it might be possible to define a radiomics predictive signature that will serve as a virtual biopsy. A set of radiomics features extracted from DCE-MRI was proposed by Wang et al. to distinguish TN breast cancers from other subtypes [25]. Both tumor and its surrounding parenchyma were included in the segmentation for each of the 84 women enrolled. Eighty-five features were extracted and combined with machine learning tools. Five different classification models were designed to differentiate TN cancers against non-TN, ER+, ER-, luminal A, and luminal B cancers. Both accuracy and sensitivity of the proposed models were improved by the inclusion of the background parenchyma quantitative features, whose heterogeneity was found to strongly correlate with TN status. In 2017, Fan et al. investigated the possibility of predicting breast cancers molecular subtypes by using radiomics features extracted from DCE-MRI and integrated with clinical information [26]. They retrospectively analyzed pretreatment breast DCE-MRI of 60 breast cancer patients, where 34 were diagnosed with luminal A breast cancers, 8 with luminal B, 7 with HER2, and 11 with basal-like. Age and menopausal status accounted for the clinical data considered. It was observed that features related to tumor heterogeneity tend to have low values in cancers with best prognosis such as luminal A cancers. Moreover, the clinically aggressive HER2 subtype showed the highest enhancement values, likely due to its raised angiogenesis growth rate.

7.2. US and Digital Mammography. In 2018, a radiomics approach based on the extraction of quantitative feature from US images was proposed by Guo et al. to better define the biologic characteristics of invasive ductal carcinoma (IDC) [27]. The analysis included patients with best prognosis IDC (HR+, HER2-) and worst prognosis IDC (TN). Tumor grade was also considered. Radiomics features were sorted into six different categories: shape, margin, boundary, echo pattern, posterior acoustic pattern, and calcification. Low grade HR+, HER- tumors were found to be more irregular in shape, with ill-defined margins, posterior shadowing and hyper- or complex echo. Conversely, high grade TN showed regular shape, a hypo- or complex posterior shadowing and posterior enhancement, similarly to other studies [45, 46]. The echo pattern features were the most effective in the prediction of molecular subtypes. A radiomics approach to be applied on digital mammography with the same aim has been recently proposed by Ma et al. [28]. Thirty-nine features, including morphologic, gray scale statistic, and texture ones, were extracted from the manually segmented area on digital mammography images of 331 invasive breast cancers. A machine learning scheme was employed for the molecular subtypes classifications: triple negative versus nontriple-negative; HER2-enriched versus non-HER2-enriched and luminal versus nonluminal cancers. Four features were significantly associated with tumor subtype, revealing that digital mammography, largely available examination, could provide clinicians with quantitative as well as qualitative information.

8. Radiomics and Cancer Recurrence

Li et al. investigated a potential linking between breast cancer MRI phenotypes and multigene assays to predict the risk of recurrence [29]. This retrospective study enrolled 84 patients diagnosed with invasive breast cancers: ductal, lobular, and mixed forms. Thirty-eight computer-extracted images phenotypes were automatic obtained from MRI sequences, describing size, shape, margin morphologic appearance, enhancement texture, kinetic curve assessment, and enhancement-variance kinetics of the cancers. These 38 MRI imaging phenotypes were then correlated with the risk of recurrence scores, calculated for each of the three multigene assays considered: MammaPrint, Oncotype DX, and PAM50, previously developed to predict breast cancer recurrence the former two and the molecular subtypes the latter one. The analysis showed promising results and, accordingly to other studies presented in this review, a combined evaluation of both phenotypic and genomic data might be successfully used to assess the risk of cancer recurrence. A more recent retrospective study proposed a radiomics approach based on preoperative MRI to develop a radiomics signature associated with breast cancer recurrence [30]. They enrolled 294 patients affected by invasive breast cancer appearing as a mass on contrast-enhanced MRI. One hundred and fifty-six features were extracted and grouped into three categories: morphological, histogram-based, and higher-order texture features. A radiomics signature, named Rad-score, was calculated for each patient, who was classified at a high-risk or low risk based on the Rad-score itself.

Then, a nomogram including the radiomics signature, MRI, and clinicopathological findings was designed to predict individual cancer recurrence, estimating the disease-free survival (DFS). Results showed higher Rad-scores correlation with worse DFS and that the DFS estimation was more accurate when clinicopathological data were included in the evaluation. Drukker et al. proposed a single new radiomics feature, named most enhancing tumor volume (METV), to be used instead of the functional tumor volume, FTV (a semiautomatically biomarker previously employed for the same purpose) for the prediction of recurrence-free survival [31]. They retrospectively included the same 141 women, affected by invasive breast cancer and treated with NAC, enrolled in the FTV validation dataset. METV, obtained on unenhanced and enhanced MR sequences, performed before and after the first cycle of NAC, was found reliable in the prediction of earlier cancer recurrence, with the advantage of being real-time and automatically calculated.

9. Discussion

Radiomics is a relatively new discipline with potentially limitless applications in clinical practice and research [2, 3]. The strengths of this postprocessing tool, however, have been mainly demonstrated in oncology imaging, where radiomics provides a comprehensive noninvasive characterization of the whole tumor, defining what it has been named the radiomics signature of the tumor [3]. Biopsy, which certainly remains central in breast cancer management, cannot be representative of the tumor entirety, whose characterization is mandatory for a thorough understanding of the tumor behavior with respect to treatment response particularly. The studies presented in our narrative review have shown that radiomics is promising in the prediction of malignancy, response to NAC, prognostic factors, molecular subtypes, and risk of recurrence. Results have also suggested that the integration of quantitative information with clinical, histological, and genomic data is key in the era of personalized treatments [3]. However, the application of the proposed radiomics approaches in clinical practice is hampered by the lack of knowledge of its basic concepts among radiologists and by the limited availability of efficient and standardized systems of feature extraction and data sharing. Furthermore, given that the majority of radiomics studies is retrospective and with a relatively small simple size, larger prospective studies are needed to validate these preliminary results.

In conclusion, we believe that the definition of a breast cancer radiomics signature could support clinicians to choose the best treatment option, assigning radiologist a central role in breast cancer management.

Abbreviations

ADC:	Apparent diffusion coefficient
AUC:	Area under the curve
AURKB(GE):	Aurora kinase B gene

DBT:	Digital breast tomosynthesis
DCE-MRI:	Dynamic contrast-enhanced-magnetic resonance imaging
DFS:	Disease-free survival
DWI:	Diffusion weighted imaging
ER:	Estrogen receptor
FTV:	Functional tumor volume
HER2:	Human epidermal growth factor receptor-2
IDC:	Invasive ductal carcinoma
METV:	Most enhancing tumor volume
MRI:	Magnetic resonance imaging
NAC:	Neoadjuvant chemotherapy
pCR:	Pathological complete response
PR:	Progesterone receptor
RFM:	Radiomic feature maps
ROI:	Region of interest
SLN:	Sentinel lymph node
TN:	Triple negative
US:	Ultrasound.

Conflicts of Interest

The authors declare that they have no conflicts of interest.

References

- [1] R. L. Siegel, K. D. Miller, and A. Jemal, "Cancer Statistics, 2017," *CA: A Cancer Journal for Clinicians*, vol. 67, no. 1, pp. 7–30, 2017.
- [2] F. Valdora, N. Houssami, F. Rossi, M. Calabrese, and A. S. Tagliafico, "Rapid review: radiomics and breast cancer," *Breast Cancer Research and Treatment*, vol. 169, no. 2, pp. 217–229, 2018.
- [3] R. J. Gillies, P. E. Kinahan, and H. Hricak, "Radiomics: images are more than pictures, they are data," *Radiology*, vol. 278, no. 2, pp. 563–577, 2016.
- [4] H. Li, Y. Zhu, E. S. Burnside et al., "Quantitative MRI radiomics in the prediction of molecular classifications of breast cancer subtypes in the TCGA/TCIA data set," *NPJ Breast Cancer*, vol. 2, no. 1, 2016.
- [5] P. Lambin, E. Rios-Velazquez, R. Leijenaar et al., "Radiomics: extracting more information from medical images using advanced feature analysis," *European Journal of Cancer*, vol. 48, no. 4, pp. 441–446, 2012.
- [6] C. Parmar, E. R. Velazquez, R. Leijenaar et al., "Robust radiomics feature quantification using semiautomatic volumetric segmentation," *PLoS ONE*, vol. 9, no. 7, 2014.
- [7] A. Fedorov, R. Beichel, J. Kalpathy-Cramer et al., "3D slicer as an image computing platform for the quantitative imaging network," *Magnetic Resonance Imaging*, vol. 30, no. 9, pp. 1323–1341, 2012.
- [8] V. Kumar, Y. Gu, and S. Basu, "Radiomics: the process and the challenges," *Magnetic Resonance Imaging*, vol. 30, no. 9, pp. 1234–1248, 2012.
- [9] H. J. W. L. Aerts, E. R. Velazquez, R. T. H. Leijenaar et al., "Erratum: Decoding tumour phenotype by noninvasive imaging using a quantitative radiomics approach," *Nature Communications*, vol. 5, 2014.
- [10] R. Wilson and A. Devaraj, "Radiomics of pulmonary nodules and lung cancer," *Translational Lung Cancer Research*, vol. 6, no. 1, pp. 86–91, 2017.
- [11] Y. Huang, Z. Liu, L. He et al., "Radiomics signature: A potential biomarker for the prediction of disease-free survival in early-stage (I or II) non-small cell lung cancer," *Radiology*, vol. 281, no. 3, pp. 947–957, 2016.
- [12] H. Rahbar, E. S. McDonald, J. M. Lee, S. C. Partridge, and C. I. Lee, "How Can Advanced Imaging Be Used to Mitigate Potential Breast Cancer Overdiagnosis?" *Academic Radiology*, vol. 23, no. 6, pp. 768–773, 2016.
- [13] V. S. Parekh and M. A. Jacobs, "Integrated radiomic framework for breast cancer and tumor biology using advanced machine learning and multiparametric MRI," *npj Breast Cancer*, vol. 3, no. 1, 2017.
- [14] H. M. Whitney, N. S. Taylor, K. Drukker et al., "Additive Benefit of Radiomics Over Size Alone in the Distinction Between Benign Lesions and Luminal A Cancers on a Large Clinical Breast MRI Dataset," *Academic Radiology*, 2018.
- [15] S. Bickelhaupt, D. Paech, P. Kickingeder et al., "Prediction of malignancy by a radiomic signature from contrast agent-free diffusion MRI in suspicious breast lesions found on screening mammography," *Journal of Magnetic Resonance Imaging*, vol. 46, no. 2, pp. 604–616, 2017.
- [16] S. Bickelhaupt, P. F. Jaeger, F. B. Laun et al., "Radiomics Based on Adapted Diffusion Kurtosis Imaging Helps to Clarify Most Mammographic Findings Suspicious for Cancer," *Radiology*, vol. 287, no. 3, pp. 761–770, 2018.
- [17] Q. Zhang, Y. Xiao, J. Suo et al., "Sonoelastomics for Breast Tumor Classification: A Radiomics Approach with Clustering-Based Feature Selection on Sonoelastography," *Ultrasound in Medicine & Biology*, vol. 43, no. 5, pp. 1058–1069, 2017.
- [18] A. S. Tagliafico, F. Valdora, G. Mariscotti et al., "An exploratory radiomics analysis on digital breast tomosynthesis in women with mammographically negative dense breasts," *The Breast Journal*, vol. 40, pp. 92–96, 2018.
- [19] N. M. Braman, M. Etesami, P. Prasanna et al., "Erratum: Intratumoral and peritumoral radiomics for the pretreatment prediction of pathological complete response to neoadjuvant chemotherapy based on breast DCE-MRI," *Breast Cancer Research*, vol. 19, no. 1, 2017.
- [20] Y. Dong, Q. Feng, W. Yang et al., "Preoperative prediction of sentinel lymph node metastasis in breast cancer based on radiomics of T2-weighted fat-suppression and diffusion-weighted MRI," *European Radiology*, vol. 28, no. 2, pp. 582–591, 2018.
- [21] J.-P. Obeid, R. Stoyanova, D. Kwon et al., "Multiparametric evaluation of preoperative MRI in early stage breast cancer: prognostic impact of peri-tumoral fat," *Clinical and Translational Oncology*, vol. 19, no. 2, pp. 211–218, 2017.
- [22] P. Liu, W. Ma, Y. Ji et al., "Breast cancer Ki67 expression preoperative discrimination by DCE-MRI radiomics features," in *Proceedings of the Multimodal Biomedical Imaging XIII*, p. 22, San Francisco, United States, January 2018.
- [23] C. Liang, Z. Cheng, Y. Huang et al., "An MRI-based Radiomics Classifier for Preoperative Prediction of Ki-67 Status in Breast Cancer," *Academic Radiology*, vol. 25, no. 9, pp. 1111–1117, 2018.
- [24] W. Guo, H. Li, Y. Zhu et al., "Prediction of clinical phenotypes in invasive breast carcinomas from the integration of radiomics and genomics data," *Journal of Medical Imaging*, vol. 2, no. 4, p. 041007, 2015.
- [25] J. Wang, F. Kato, N. Oyama-Manabe et al., "Identifying triple-negative breast cancer using background parenchymal enhancement heterogeneity on dynamic contrast-enhanced

- MRI: A pilot radiomics study,” *PLoS ONE*, vol. 10, no. 11, Article ID e0143308, 2015.
- [26] M. Fan, H. Li, S. Wang, B. Zheng, J. Zhang, and L. Li, “Radiomic analysis reveals DCE-MRI features for prediction of molecular subtypes of breast cancer,” *PLoS One*, vol. 12, no. 2, 2017.
- [27] Y. Guo, Y. Hu, M. Qiao et al., “Radiomics Analysis on Ultrasound for Prediction of Biologic Behavior in Breast Invasive Ductal Carcinoma,” *Clinical Breast Cancer*, vol. 18, no. 3, pp. e335–e344, 2018.
- [28] W. Ma, Y. Zhao, Y. Ji et al., “Breast Cancer Molecular Subtype Prediction by Mammographic Radiomic Features,” *Academic Radiology*, 2018.
- [29] H. Li, Y. Zhu, E. S. Burnside et al., “MR imaging radiomics signatures for predicting the risk of breast cancer recurrence as given by research versions of MammaPrint, oncotype DX, and PAM50 gene assays,” *Radiology*, vol. 281, no. 2, pp. 382–391, 2016.
- [30] H. Park, Y. Lim, E. S. Ko et al., “Radiomics Signature on Magnetic Resonance Imaging: Association with Disease-Free Survival in Patients with Invasive Breast Cancer,” *Clinical Cancer Research*.
- [31] K. Drukker, H. Li, N. Antropova, A. Edwards, J. Papaioannou, and M. L. Giger, “Most-enhancing tumor volume by MRI radiomics predicts recurrence-free survival “early on” in neoadjuvant treatment of breast cancer,” *Cancer Imaging*, vol. 18, no. 1, 2018.
- [32] P. A. T. Baltzer, M. Benndorf, M. Dietzel, M. Gajda, O. Camara, and W. A. Kaiser, “Sensitivity and specificity of unenhanced MR mammography (DWI combined with T2-weighted TSE imaging, ueMRM) for the differentiation of mass lesions,” *European Radiology*, vol. 20, no. 5, pp. 1101–1110, 2010.
- [33] M. Telegrafo, L. Rella, A. A. Stabile Ianora, G. Angelelli, and M. Moschetta, “Unenhanced breast MRI (STIR, T2-weighted TSE, DWIBS): An accurate and alternative strategy for detecting and differentiating breast lesions,” *Magnetic Resonance Imaging*, vol. 33, no. 8, pp. 951–955, 2015.
- [34] S. Bickelhaupt, F. B. Laun, J. Tesdorff et al., “Fast and noninvasive characterization of suspicious lesions detected at breast cancer X-ray screening: Capability of diffusion-weighted MR imaging with MIPs,” *Radiology*, vol. 278, no. 3, pp. 689–697, 2016.
- [35] W. Bogner, S. Gruber, K. Pinker et al., “Diffusion-weighted MR for differentiation of breast lesions at 3.0 T: How does selection of diffusion protocols affect diagnosis?” *Radiology*, vol. 253, no. 2, pp. 341–351, 2009.
- [36] A. M. Thompson and S. L. Moulder-Thompson, “Neoadjuvant treatment of breast cancer,” *Annals of Oncology*, vol. 23, no. 10, pp. x231–x236, 2012.
- [37] S. Luangdilok, N. Samarntai, and K. Korphaisarn, “Association between pathological complete response and outcome following neoadjuvant chemotherapy in locally advanced breast cancer patients,” *Journal of Breast Cancer*, vol. 17, no. 4, pp. 376–385, 2014.
- [38] H. Earl, E. Provenzano, J. Abraham et al., “Neoadjuvant trials in early breast cancer: Pathological response at surgery and correlation to longer term outcomes - what does it all mean?” *BMC Medicine*, vol. 13, no. 1, 2015.
- [39] E. J. Gallagher and D. LeRoith, “Obesity and diabetes: The increased risk of cancer and cancer-related mortality,” *Physiological Reviews*, vol. 95, no. 3, pp. 727–748, 2015.
- [40] P. J. Goodwin, C. B. Ambrosone, and C. Hong, “Modifiable Lifestyle Factors and Breast Cancer Outcomes: Current Controversies and Research Recommendations,” in *Improving Outcomes for Breast Cancer Survivors*, vol. 862 of *Advances in Experimental Medicine and Biology*, pp. 177–192, Springer International Publishing, Cham, 2015.
- [41] M. J. Ellis, V. J. Suman, J. Hoog et al., “Ki67 proliferation index as a tool for chemotherapy decisions during and after neoadjuvant aromatase inhibitor treatment of breast cancer: Results from the American college of surgeons oncology group Z1031 trial (alliance),” *Journal of Clinical Oncology*, vol. 35, no. 10, pp. 1061–1069, 2017.
- [42] G. Viale, A. Giobbie-Hurder, M. M. Regan et al., “Prognostic and predictive value of centrally reviewed Ki-67 labeling index in postmenopausal women with endocrine-responsive breast cancer: Results from breast international group trial 1-98 comparing adjuvant tamoxifen with letrozole,” *Journal of Clinical Oncology*, vol. 26, no. 34, pp. 5569–5575, 2008.
- [43] A. Goldhirsch, E. Winer, A. Coates et al., “Personalizing the treatment of women with early breast cancer: highlights of the St Gallen International Expert Consensus on the Primary Therapy of Early Breast Cancer 2013,” *Annals of Oncology*, vol. 24, pp. 2206–2223, 2013.
- [44] B. S. Rosenstein, C. M. West, S. M. Bentzen et al., “Radiogenomics: Radiobiology Enters the Era of Big Data and Team Science,” *International Journal of Radiation Oncology • Biology • Physics*, vol. 89, no. 4, pp. 709–713, 2014.
- [45] P. Tang, K. A. Skinner, and D. G. Hicks, “Molecular classification of breast carcinomas by immunohistochemical analysis: Are we ready?” *Diagnostic Molecular Pathology*, vol. 18, no. 3, pp. 125–132, 2009.
- [46] L. Zhang, Y.-J. Liu, S.-Q. Jiang, H. Cui, Z.-Y. Li, and J.-W. Tian, “Ultrasound utility for predicting biological behavior of invasive ductal breast cancers,” *Asian Pacific Journal of Cancer Prevention*, vol. 15, no. 19, pp. 8057–8062, 2014.

Research Article

Patch Based Grid Artifact Suppressing in Digital Mammography

Qingqing Ling,¹ Shuyu Wu,¹ Xiaoman Duan,¹ Genggeng Qin ,² Jianhui Ma,¹
Chaomin Chen,¹ Hongliang Qi ,¹ Linghong Zhou ,¹ and Yuan Xu ¹

¹School of Biomedical Engineering, Southern Medical University, Guangzhou 510515, China

²Department of Radiology, Nanfang Hospital, Southern Medical University, Guangzhou 510515, China

Correspondence should be addressed to Linghong Zhou; smart@smu.edu.cn and Yuan Xu; yuanxu@smu.edu.cn

Received 21 December 2017; Revised 22 May 2018; Accepted 18 July 2018; Published 12 August 2018

Academic Editor: Luca Brunese

Copyright © 2018 Qingqing Ling et al. This is an open access article distributed under the Creative Commons Attribution License, which permits unrestricted use, distribution, and reproduction in any medium, provided the original work is properly cited.

The mammography is the first choice of breast cancer screening, which has proven to be the most effective screening method. An antiscatter grid is usually employed to enhance the contrast of image by absorbing unexpected scattered signals. However, the grid pattern casts shadows and grid artifacts, which severely degrade the image quality. To solve the problem, we propose the patch based frequency signal filtering for fast grid artifacts suppressing. As opposed to whole image processing synchronously, the proposed method divides image into a number of blocks for tuning filter simultaneously, which reduces the frequency interference among image blocks and saves computation time by multithread processing. Moreover, for mitigating grid artifacts more precisely, characteristic peak detection is employed in each block automatically, which can accurately identify the location of the antiscatter grid and its motion pattern. Qualitative and quantitative studies were performed on simulation and real machine data to validate the proposed method. The results show great potential for fast suppressing grid artifacts and generating high quality of digital mammography.

1. Introduction

Breast cancer ranks as the first leading cancer in women all over the world [1]. According to the Global Burden of Disease Report [2, 3], the newly increased incidence and death tolls of breast cancer are on the rise around the world, which has accounted for one-quarter of the total new cases of women. The early screening and diagnosis of breast cancer are helpful to improve the survival fraction and quality of life [4]. Imaging examination is one of the most significant measurements in the breast cancer screening [5], which includes B-ultrasound, CT, MRI, and X-ray mammography [6–10]. The X-ray mammography is the first choice of breast cancer screening, which has proven to be the most effective screening method by World Health Organization [1]. When X-rays pass through the breast tissue, the irregular direction scattered signals are generated because of the Compton effect and Rayleigh scattering [11]. An antiscatter grid between the patient and the image detector is usually employed to enhance the contrast of image by absorbing unexpected scattered signals [12], and the grid consists of

alternating transmitting material and absorbing material of X-ray. However, the grid pattern casts shadows on the image detector and produces grid artifacts in the acquired X-ray image due to the existence of absorbing material [13, 14]. The artifacts severely degrade the image quality. Hence, grid artifact suppressing is the prerequisite and foundation in digital mammography.

To address the issue, various approaches have been proposed. The grid artifacts suppressing methods are classified as hardware methods and image processing methods. The first category utilizes grid techniques to depress artifacts. For instance, moving grids is frequently used to mitigate grid artifacts [12] with oscillating and reciprocating as basic moving mechanism. However, this technique is employed with extra complexity. By analyzing grid movements, Bednarek et al. [15] found that small grid movements could reduce artifacts under the conditions of the synchronization between linear grid motion and exposure time. Gauntt and Barnes introduced a comprehensive theory on the antiscatter grids [16] and also proposed an artifact suppression technique [17], and in this technique the grid moved at a modest

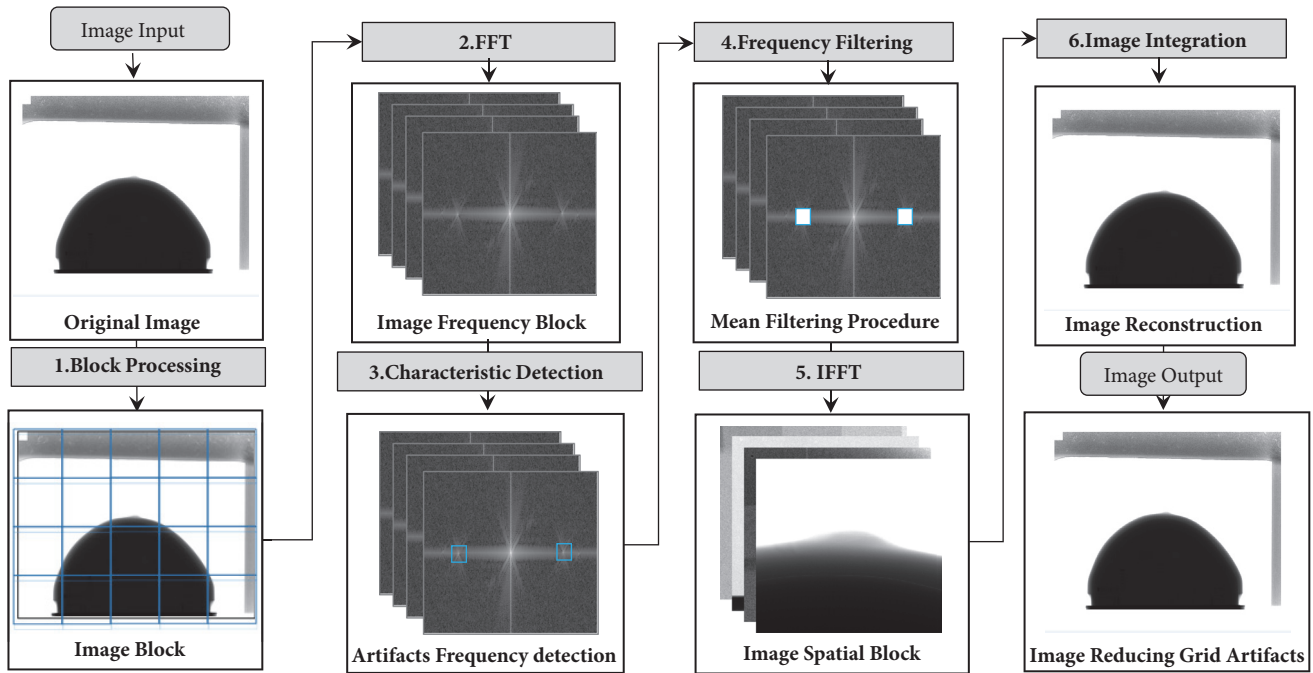


FIGURE 1: Workflow of the integrated method.

velocity when the X-ray exposure waveform had a soft start and stop. Those algorithms may be complicated due to the dependence of grid movement. Moreover, a high line density of the grid is necessary for obtaining more perfect image quality.

Image processing methods mainly depend on digital image processing techniques [18] rather than grid movement. For example, Wang and Huang [19] proposed a mathematical method to remove aliasing artifacts based on studying the amplitudes and the frequencies of artifacts and converted a film into digital form. Barski and Wang [20] proposed a method for grid artifacts reducing based on one-dimensional discrete Fourier transform and one-dimension frequency filtering by structuring blur kernels. Moreover, the one-dimension notch filter was also used by Belykh and Cornelius [21]. Unfortunately, the ripple artifacts were produced in the image. Different from the one-dimensional method based on frequency domain, Sasada et al. [22] proposed two-dimensional filtering based on the wavelet domain to alleviate grid artifacts. In another study by Lin et al. [23], Gaussian band-stop filters were conducted to reduce artifacts by determining the artifacts frequency. In addition, Zhang et al. [24] constructed an adaptive frequency filter by determining stripe frequency band and frequency distribution function to remove the artifacts. This method is easy to implement, but it was only tested on the infrared image. In order to minimize the damage from grid artifact reduction, Kim and Lee first analyzed grid artifacts with multiplicative model and rotated stationary grids and then removed grid artifacts by constructing the homomorphic filtering consisting of band-stop filters and one-dimensional low-pass filters for searching the optimal grid frequencies and angles [25–28]. Tang et

al. decomposed the image into several subimages using a multiscale two-dimensional discrete wavelet transform and the remove gridline signals by an automatic Gaussian band-stop filter [29]. There is higher accuracy of recognizing grid frequency in the method; however, this algorithm may involve fairly long computation time for searching the accurate grid frequencies and angles.

To address the above issues, we propose a patch based method for fast frequency signal filtering and grid artifacts suppressing in digital mammography. As opposed to whole image processing synchronously, the proposed method divides the image into a number of blocks processing simultaneously, which reduces the frequency interference among image blocks as well as saving computation time because of using multithread processing. Moreover, in order to alleviate grid artifacts more precisely, characteristic peak detection is employed in each block automatically, which can accurately identify the position of the antiscatter grid and its motion pattern.

The remaining part of this paper is organized as follows. Section 2 describes the workflow and each key step in detail. Section 3 focuses on the implementations to validate the proposed method. Experimental results are shown by simulation study and real digital mammography machine. In Section 4, a few related issues are discussed. Conclusions are given in Section 5.

2. Materials and Methods

Figure 1 shows a workflow of the proposed method, which consists of six steps. In step 1, the original mammogram is divided into several blocks. In step 2, in spatial domain,

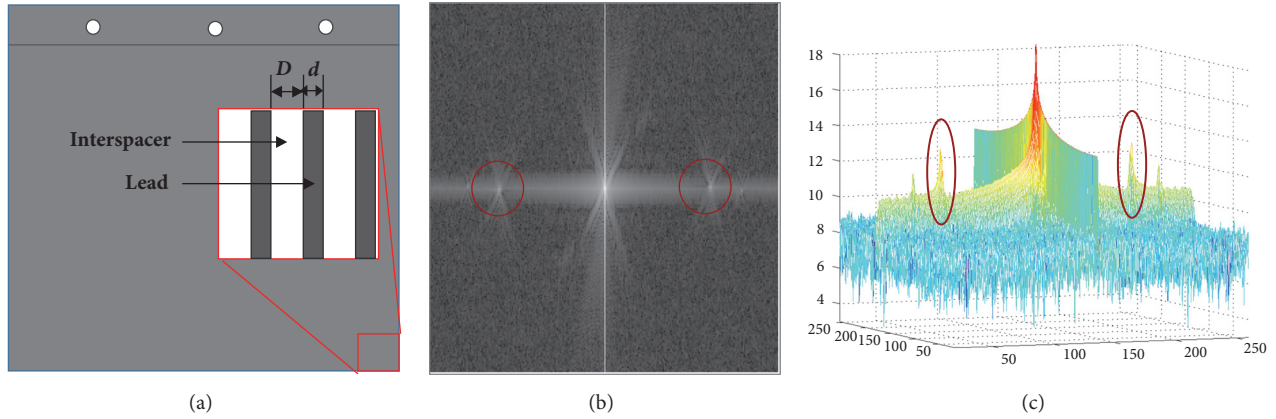


FIGURE 2: (a) Internal structure of antiscatter grid; (b) block image in the frequency domain; (c) 3D description of frequency components.

two-dimensional FFT is utilized to acquire frequency data of each block. In step 3, in frequency domain, the characteristic frequency detection of grid artifacts is implemented automatically in each frequency block. In step 4, the frequency filtering of characteristic peak is realized by using an improved mean filter. In step 5, the spatial image blocks are obtained by IFFT. Finally, we integrate the spatial image blocks by the inverse operation in step 1. By the above-mentioned steps, the corrected image of the grid artifacts suppressing is realized. The core of the proposed method is in step 1, step 3, and step 4. These steps in the workflow will be detailed and presented in the rest of the section.

2.1. Patch Based Deconstruction and Transformation. In this section, image block processing is introduced in detail, which is one of key steps of the proposed method. For a given image $f(x, y)$, block processing can be expressed as

$$f_b(x, y) = f(x, y)|_{x \in [x_b, x_b+X], y \in [y_b, y_b+Y]} \quad (1)$$

where (x_b, y_b) is the top left pixel coordinate of the image block, and $X \times Y$ is size of the image block.

There are a few points we would like to mention when the patch is applied in image deconstruction. First, image patch processing can decrease the frequency interference between different blocks. In addition, multithread parallel processing can reduce time overload and improve the efficiency of Central Processing Unit (CPU).

The image block is decomposed into sine and cosine components by the FFT. For an image block $f_b(x, y)$ with size of $X \times Y$, its expression of the two-dimensional FFT is as follows:

$$F(u, v) = \frac{1}{XY} \sum_{x=0}^{X-1} \sum_{y=0}^{Y-1} f_b(x, y) e^{-2\pi j(ux/X+vy/Y)} \quad (2)$$

where $F(u, v)$ is the frequency domain data, $u = 0, 1, \dots, X-1$, and $v = 0, 1, \dots, Y-1$.

2.2. Characteristic Peak Detection. In the spatial domain, the grid artifacts can be considered as periodic streak artifacts. So they are expressed as symmetrical signals in the

frequency domain [30] as shown in Figures 2(b) and 2(c). The frequency signals of grid artifacts are mainly in the red circles.

As mentioned previously, in order to remove grid artifacts precisely, the characteristic frequency detection of grid signals is conducted without manual intervention. According to sampling theorem and the FFT [31], the characteristic peak range of periodic signals in the frequency domain is defined as

$$N_f = \left[\zeta, \frac{(1/SR_p) \times ld \times Dim}{10} + \sigma \right] \quad (3)$$

where ζ and σ are length and width of detection range, Dim is the image resolution, SR_p is the image block resolution, and ld is the grid density. SR_p and ld are defined as

$$SR_p = \frac{1}{ps} \quad (4)$$

where ps is the pixel size depending on image detector.

$$ld = \frac{10}{D+d} \quad (5)$$

where D is the distance between two grids filled with interspacer such as aluminum oxide or plastic fiber in the antiscatter grid, d is the width of each grid made by lead [32]. The internal structure of antiscatter grid is shown in Figure 2(a).

After obtaining the range of characteristic peak frequency, we chose the maximum value of N_f as filter frequency by the experience and experiments. And F_{max} is expressed as

$$F_{max} = \max(F(u, v))|_{(u,v) \in N_f} \quad (6)$$

From (3), N_f is proportional to image resolution Dim and grid density ld , so the values of Dim and ld are lowered while the value of N_f is synchronously decreased. The relationship among the three variables indicates that we can obtain high precision of characteristic frequency even with the lower image resolution and common accuracy of grid density.

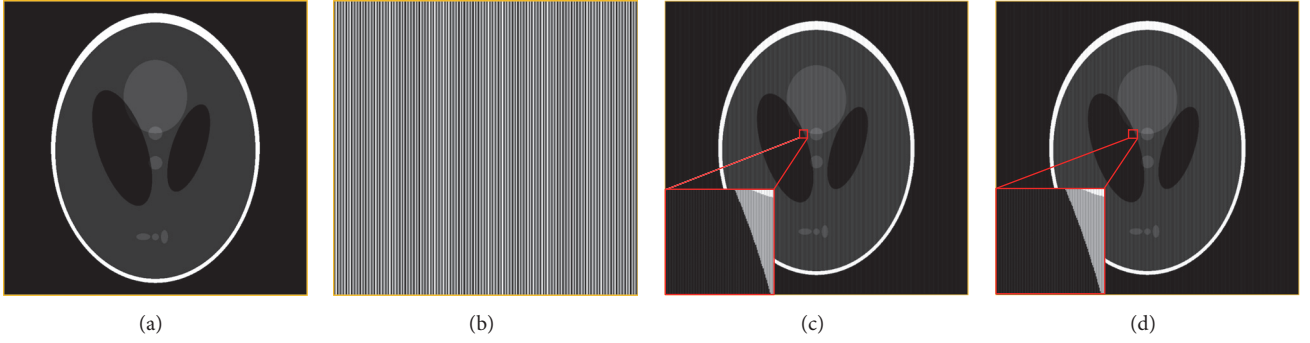


FIGURE 3: (a) Shepp-Logan phantom image; (b) the grid pattern of 3.5 lp/mm in spatial domain; (c) simulated image integrated with grid artifacts of 3.5 lp/mm; (d) simulated image integrated with grid artifacts of 3.49 lp/mm.

2.3. Frequency Signal Filtering and Reconstruction. For global filtering, the peak attenuation of characteristic frequency happened, which could lead to some loss of image information. Hence, global processing may produce filtering error and have a poor robustness. On the contrary, the block filtering could determine a proper filter size according to the block size and it could reduce the corresponding frequency interference between different blocks. Moreover, if an image block has a filter error, the impact of the error on the whole process could be ignored. Besides, considering that the computational complexities for the global filtering are so serious for the current detector products, we combined block blocking and local filters to improve computation efficiency by using GPU multithread processing. For minimizing the influence of artifacts frequency filtering, we propose an improved filter based on the conventional mean filter [18] to reduce characteristic frequency signals. The expression of filtering procedure is as follows:

$$G(u, v) = \text{mean}(F(u, v) * H(u, v))_{(u,v) \in D} \quad (7)$$

$$H(u, v) = \begin{pmatrix} 1 & 0 & \cdots & 0 & 0 \\ 0 & 1 & \cdots & 0 & 0 \\ \vdots & \vdots & 1 & \vdots & \vdots \\ 0 & 0 & \cdots & 1 & 0 \\ 0 & 0 & \cdots & 0 & 1 \end{pmatrix}_{M \times M} \quad (8)$$

where $M \times M$ is the size of mean filter, D is the frequency domain with the size of $M \times M$, and its center coordinate is (u_1, v_1) calculated from (6). The fundamental grid frequency indeed contains some harmonic components. Comparing with fundamental components, the harmonics have a higher frequency but a much lower magnitude [23]. And removing harmonics is not significant for grid artifacts suppressing and may introduce a new artifact. Hence, we ignored the effect of harmonic components.

Finally, the two-dimensional IFFT is utilized to convert the frequency domain data into spatial domain data, and then we integrate the processed image blocks to reconstruct

the image without grid artifacts. For a frequency block $G(u, v)$ with size of $X \times Y$, its two-dimensional IFFT is calculated as

$$f'(x, y) = \sum_{u=0}^{X-1} \sum_{v=0}^{Y-1} G(u, v) e^{2\pi j(ux/X+vy/Y)} \quad (9)$$

where $f'(x, y)$ is the spatial domain data.

2.4. Data Acquisition. To verify the efficacy and efficiency of the proposed method, the proposed method is tested by a simulation study of the classic Shepp-Logan phantom and a real phantom study. For simulation data with grid artifacts acquisition, the simulated grid pattern is added to the Shepp-Logan phantom image. The Shepp-Logan phantom image with the size of 2048×2048 is shown in Figure 3(a) and the simulated grid pattern image with 3.5-line pair per millimeter (lp/mm) is shown in Figure 3(b). Figures 3(c) and 3(d) show the Shepp-Logan phantom images integrated with simulated grid artifacts of 3.49 lp/mm and 3.5 lp/mm, respectively.

Furthermore, we performed a real phantom experiment with the digital mammography system as shown in Figure 4(a). The breast quality control phantom (CIRS, Inc., USA) [33] is used in this paper and its external and internal system structures are shown in Figures 4(b) and 4(c). In addition, the quality control phantom consists of 50% adipose material with 4.5cm thickness, 50% glands simulation material, and a removable 0.5cm equivalent layer of adipose tissue. In the study, an a-Se direct detector (AXS-2430, analogic Inc., Québec, Canada) with a pixel size of 0.085mm and the 2816×3584 resolution is employed.

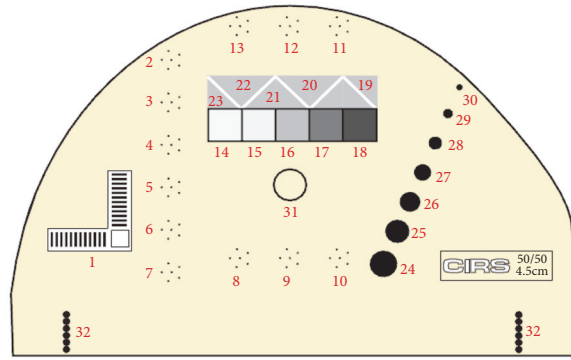
For qualitative evaluation in detail, we select four ROIs with central coordinates at (443, 487), (923, 1015), (1023, 1655), and (1627, 1523) in the simulation experiment, respectively. Figure 5(a) shows ROI#1, ROI#2, ROI#3, and ROI#4 with size of 256×256 in the red rectangles, respectively. Concerning real image observation, we also select four ROIs with central coordinates at (1763, 1301), (2017, 1805), (1669, 2160), and (2257, 2584), respectively. Figure 5(b) shows ROI#1, ROI#2, ROI#3, and ROI#4 with size of 256×256 in the red rectangles, respectively.



(a)



(b)



(c)

FIGURE 4: (a) Digital mammography system; (b) shape of CIRS 011A; (c) internal structure of CIRS 011A.

For the quantitative measurement, we utilize the normalized mean absolute distance (NMAB) to measure the difference between the conventional method and the proposed method. The NMAB of ROI is calculated:

$$NMAB = \frac{\sum_i^M \sum_j^N |f_{roc}(i, j) - f_{true}(i, j)|}{\sum_i^M \sum_j^N |f_{true}(i, j)|} \quad (10)$$

where $f_{roc}(i, j)$ denotes pixel value at (i, j) in the corrected ROI, $f_{true}(i, j)$ represents pixel value at (i, j) in the reference ROI, and $M \times N$ is the size of ROI. Note that the smaller the NMAB, the closer the results between the original image and the corrected image.

For quality control phantom image, we propose an evaluation term named as mean value of specific direction (MVSD) to compare the difference between the conventional method and the proposed method. The MVSD of a pixel with the coordinate at (i, j) is shown as follows:

$$MVSD(i, j) = \frac{1}{N} \sum_j^N f_{roi}(i, j) \quad (11)$$

where $f_{roi}(i, j)$ represents the pixel value at (i, j) in the ROI and N represents the width of ROI.

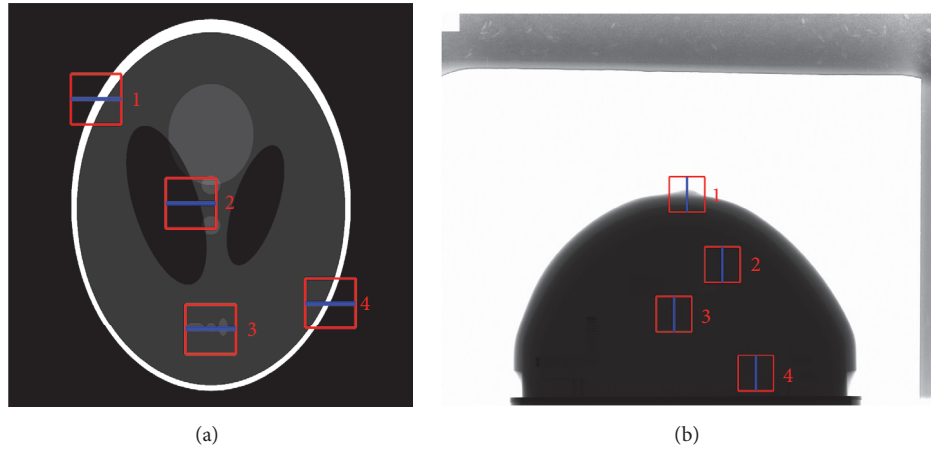


FIGURE 5: (a) Simulation image containing ROI#1, ROI #2, ROI #3, and ROI #4 in the red rectangles; (b) real image containing ROI#1, ROI #2, ROI #3, and ROI #4 in the red rectangles.

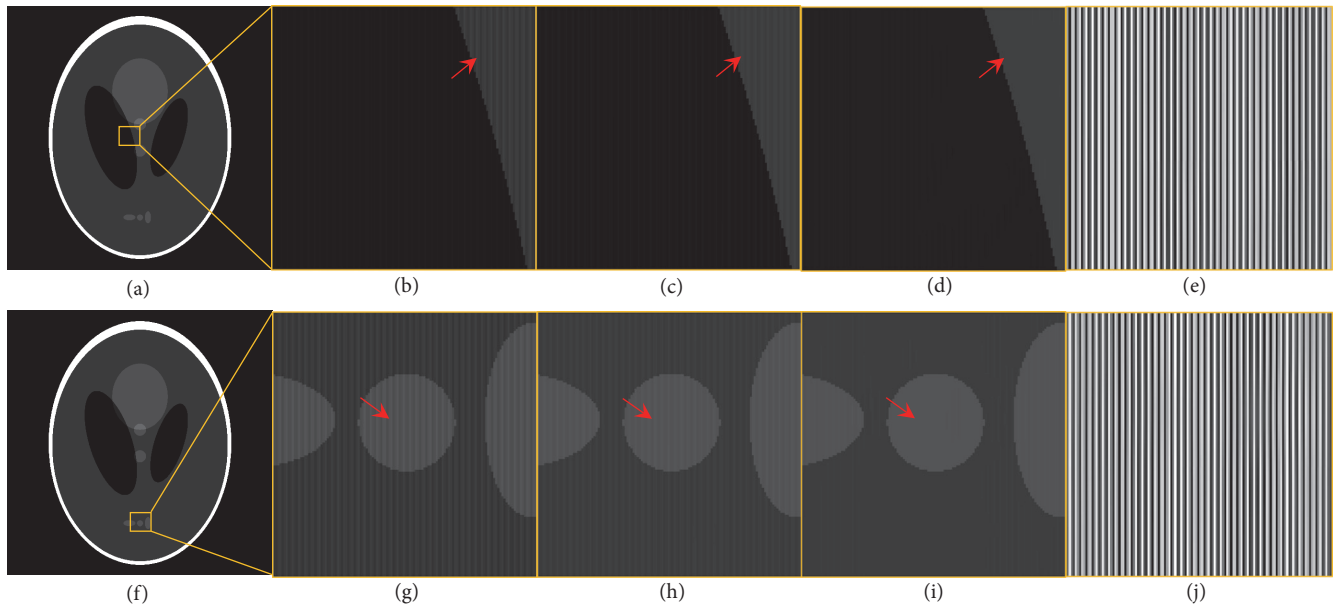


FIGURE 6: (a) Global image; (b)-(d) image without correction and images corrected by the global filter method and the proposed method of ROI#2, respectively; (g)-(i) image without correction and images corrected by the global filter method and the proposed method of ROI#4, respectively; ((e) and (j)) the spatial images of the difference between the images in (c), (h) and (d), (i) respectively; (f) global image.

3. Results

3.1. Simulation Experiment. In the simulated phantom experiment, we applied block processing with size 256×256 of image block, and the sizes of block and global filters are 15×15 and 51×51 , respectively. Figure 6 shows the simulated images with the grid artifacts of 3.49 lp/mm. Figures 6(b)–6(d) show the uncorrected image and the corrected images by the global filter method and the proposed method of ROI#2, respectively. Figures 6(g)–6(i) show the uncorrected image and the corrected images by the global filter method and the proposed method of ROI#4, respectively. As shown in the Figures 6(c) and 6(h), the global filter method can remove the grid artifacts to some extent. However, several grid artifacts

are still present, which are indicated by the red arrows. Compared with global filter method, images corrected by the proposed method are visually better, as shown in Figures 6(d) and 6(i). Those grid artifacts indicated by the red arrows almost disappear in the corrected images by the proposed method. Figures 6(e) and 6(j) show the difference images by subtracting Figures 6(c) and 6(h) from Figures 6(d) and 6(i), respectively. Figures 6(e) and 6(j) show that the proposed method can suppress more grid artifacts than global filter method.

Figure 7 plots the horizontal profiles of blue lines in ROI#1, ROI#2, ROI#3, and ROI#4 in Figure 5(a), respectively. The profiles of the results obtained by the proposed method are much closer to the results of reference image than the

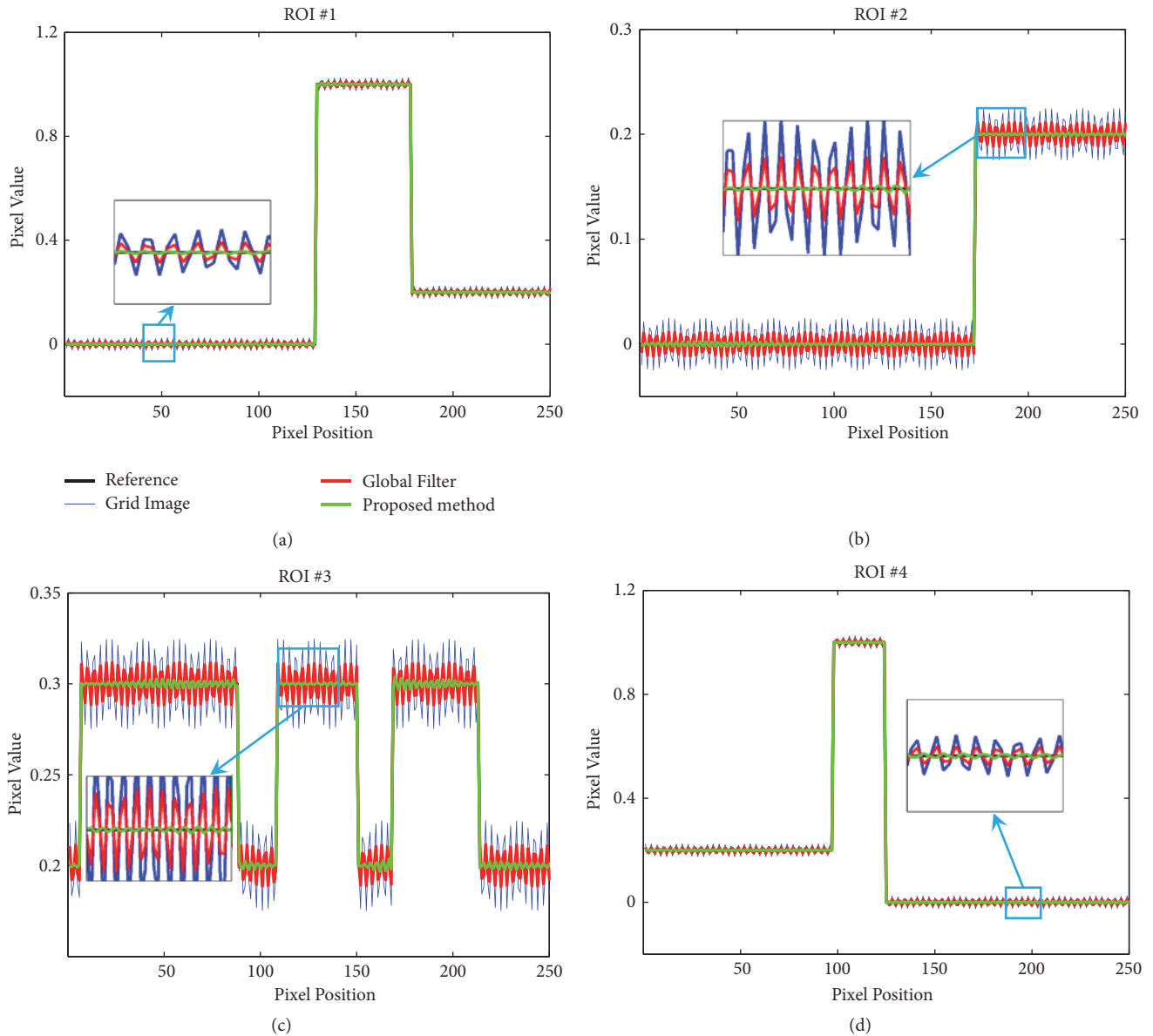


FIGURE 7: Image profiles indicated by the blue lines in ROI#1, ROI#2, ROI#3, and ROI#4 in Figure 5(a) with grid artifacts of the 3.49 lp/mm, respectively.

results by the global filter method. As shown in the blue line, the image without any correction could not match the reference well because of the grid artifacts. This result partially proves that grid artifacts seriously degrade the quality of images. As shown in the red line, the global filter method could improve image quality to some extent. However, the fluctuation in the profile demands for further improvement. By contrast, the proposed method achieves high image quality, as shown in the green line profile.

The difference between the reference image and the corrected images by the global method and the proposed method is quantitatively evaluated by NMAB. The NMAB of ROI#1, ROI#2, ROI#3, and ROI#4 with the two grid modes are shown in Tables 1 and 2, respectively. Compared with the global filter method, the results of proposed method achieve

TABLE 1: NMAB comparison of image with grid artifacts 3.49 lp/mm in different methods.

NMAB	ROI#1	ROI#2	ROI#3	ROI#4
Uncorrected	0.0630	0.1799	0.0738	0.0880
Global Filter	0.0290	0.0824	0.0344	0.0405
Proposed Method	0.0047	0.0098	0.0040	0.0063

an appreciable improvement, as shown in the last row of Tables 1 and 2.

3.2. Real Phantom Experiment. In the real phantom experiment, we applied block processing with size 256×256 of image block, and the sizes of block and global filters

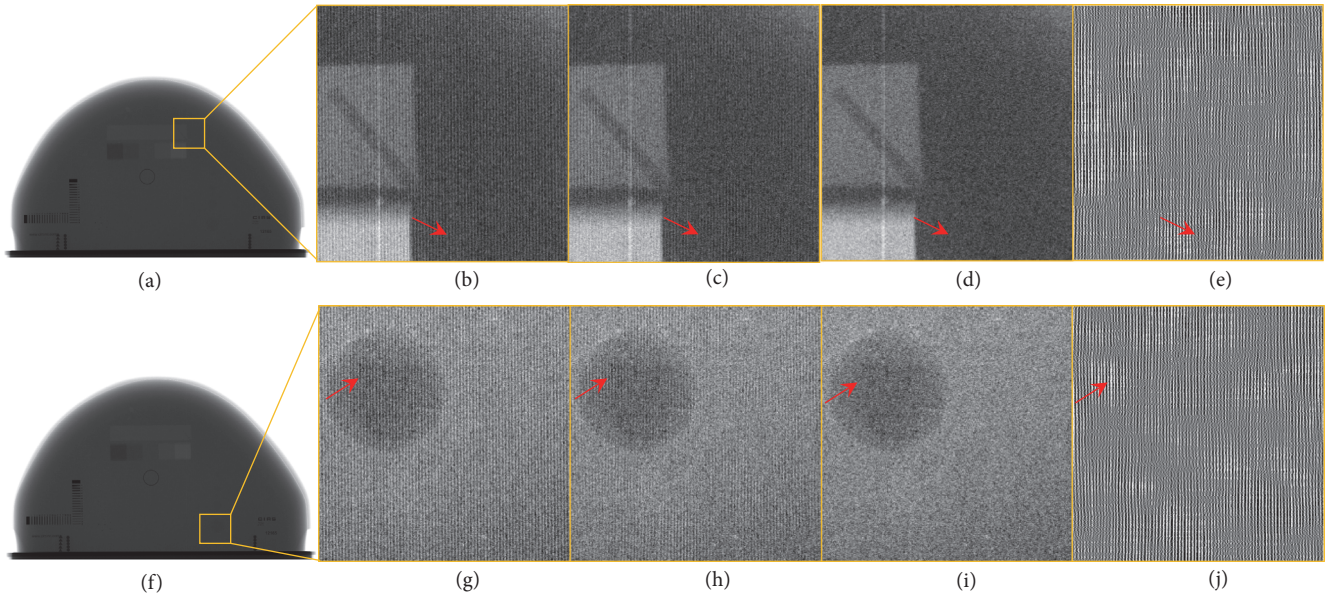


FIGURE 8: (a) Global image; (b)-(d) image without correction and images corrected by the global filter method and the proposed method of ROI#2, respectively; (g)-(i) image without correction and images corrected by the global filter method and the proposed method of ROI#3, respectively; ((e) and (j)) the spatial images of the difference between the images in (c), (h) and (d), (i) respectively; (f) global image.

TABLE 2: NMAB comparison of image with grid artifacts 3.5 lp/mm in different methods.

NMAB	ROI#1	ROI#2	ROI#3	ROI#4
Uncorrected	0.0630	0.1799	0.0738	0.0880
Global Filter	0.013	0.027	0.008	0.025
Proposed Method	0.0047	0.0095	0.0040	0.0062

are 11×11 and 61×61 , respectively. Figure 8 shows the images corrected with different methods in the real phantom experiment. Figures 8(b)–8(d) show the uncorrected image and the corrected images by the global filter method and the proposed method of ROI#2, respectively. Figures 8(g)–8(i) show the uncorrected image and the corrected images by the global filter method and the proposed method of ROI#3, respectively. As shown in Figures 8(c) and 8(h), the global filter method can remove the grid artifacts well. However, several grid artifacts are still present, which are indicated by the red arrows. Compared with the global filter method, the images corrected with the proposed method appear with fewer artifacts, as shown in Figures 8(d) and 8(i). The grid artifacts indicated by the red arrows almost entirely disappeared in the corrected images by the proposed method. Figures 8(e) and 8(j) display the difference images by subtracting Figures 8(c) and 8(h) from Figures 8(d) and 8(i), respectively. Figures 8(e) and 8(j) show that the proposed method can suppress more grid artifacts than the global filter method.

Figure 9 shows the vertical profiles of blue lines in ROI#1, ROI#2, ROI#3, and ROI#4 in Figure 5(b), respectively. The profiles of the results by the proposed method are much smoother than the results by the global filter method. As shown in the green line, the profile of the image without any

correction shows a vibration with large amplitude because of the grid artifacts. This result partially proves that grid artifacts seriously degrade the quality of images. As shown in the red line, the utilization of the global filter method achieves the improvement of image quality. However, the fluctuation in the profile demands for further improvement. By contrast, the proposed method achieves high image quality and the fluctuation is relatively weak, as shown in the black line.

4. Discussion

In this paper, we propose a fast frequency signal filtering method based on image block processing. In the proposed method, image block processing is utilized to reduce the frequency interference between image blocks. Besides, we can employ multithread processing to decrease the computing time of CPU. In addition, characteristic frequency detection is employed in each block automatically to improve the fault-tolerance property of the grid accuracy. For optimal filtering, an improvement filter is constructed to minimize the influence of the artifacts filtering processing on the significant signals. The efficiency and applicability of the proposed algorithm are achieved by using simulated phantom data as well as real phantom data.

There are several issues that we would like to discuss. Considering that the computational complexities for the global filtering are so serious for the current detector products, we combined block blocking and local filters to improve computation efficiency by using GPU multithread processing. In the real phantom experiment, the computation time is 2.278 s on a PC with i7(3.60 GHz) CPU and the time is 0.675 s by multithread processing on GPU (GTX 680) whose calculation efficiency has been increased by 3.4 times.

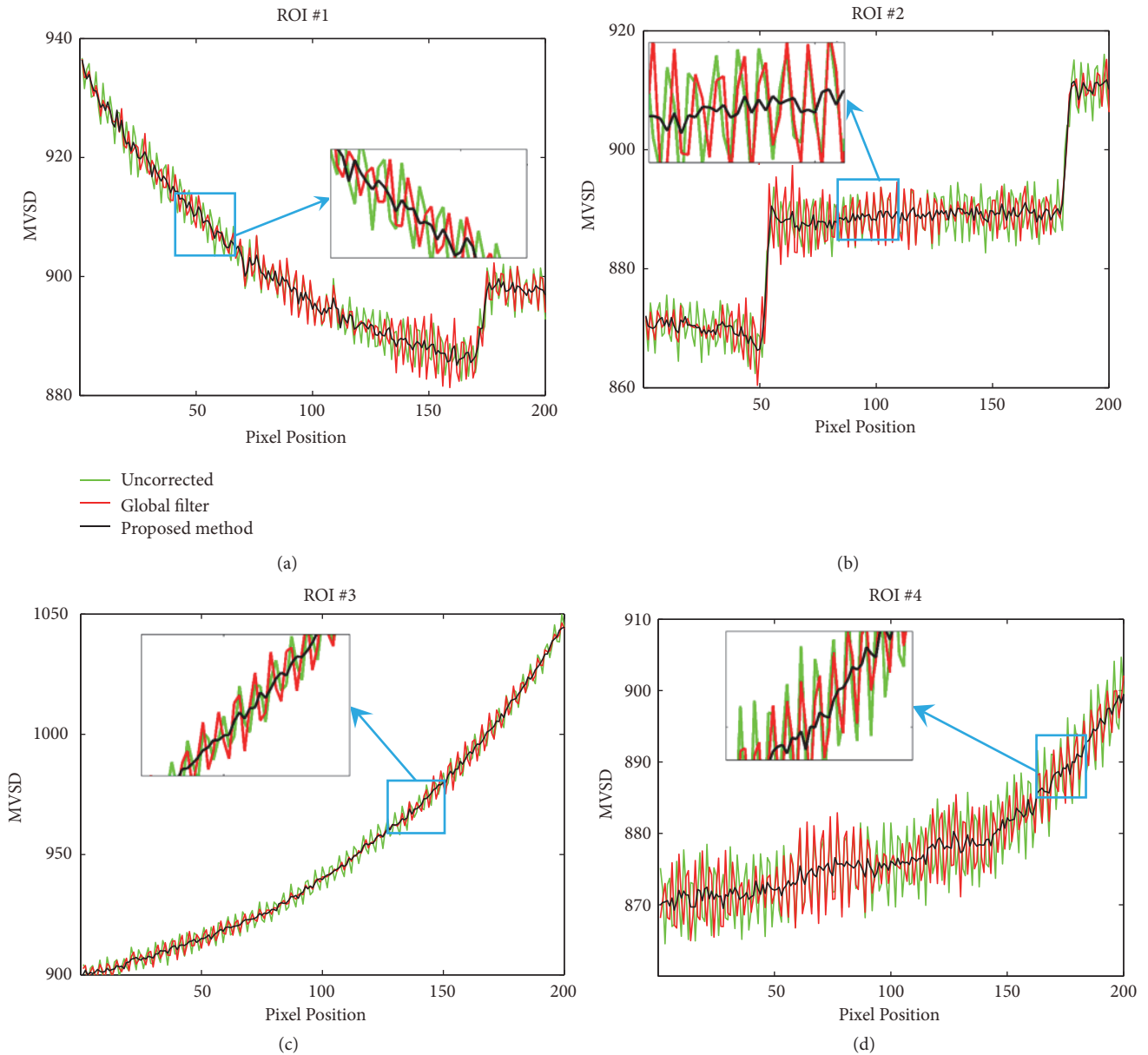


FIGURE 9: Image profiles indicated by the blue lines in ROI#1, ROI#2, ROI#3, and ROI#4 in Figure 5(b), respectively.

For image block processing, Figure 10 shows the corrected images with different block size such as 128×128 , 256×256 , and 512×512 . As shown in Figures 10(a) and 10(b), the block processing with sizes of 128×128 and 256×256 shows similar results, better than the result with size of 512×512 visually. And the time consuming is 0.680 s, 0.670 s, and 0.675 s, respectively. According to above-mentioned comparison, the optimal size of image block is 256×256 . Additionally, we would also like to discuss the parameters ζ and σ , which are closely related to detection range of characteristic frequency. By studying the frequency image, ζ and σ can be determined at the appropriate frequency offset by experience and experiment. In the paper, the size of detection range is 7×7 at a 0.2 Hz frequency offset according to our needs.

The image quality may suffer damage more or less by filtering processing. As shown in formulas (7) and (8), the users can select the optimal filter size according to their needs. In our experiments, the filter size is 15×15 in the Shepp-Logan phantom experiment, and in the real phantom (CIRS. Inc., USA) experiment the filter size is 11×11 . In frequency domain filtering, grid artifacts were removed by limiting the frequency components of grid. However, the loss of high frequency information could lead to ringing artifacts in most methods of grid artifacts suppressing. And ringing artifacts mainly exist near the contour edges of reconstructed images. Figure 11 shows the corrected images by the mean filter. Figures 11(a) and 11(b) are global simulation image by mean filter and the corresponding magnified ROI of yellow squares in Figure 11(a). As shown in Figure 11(b), there are still

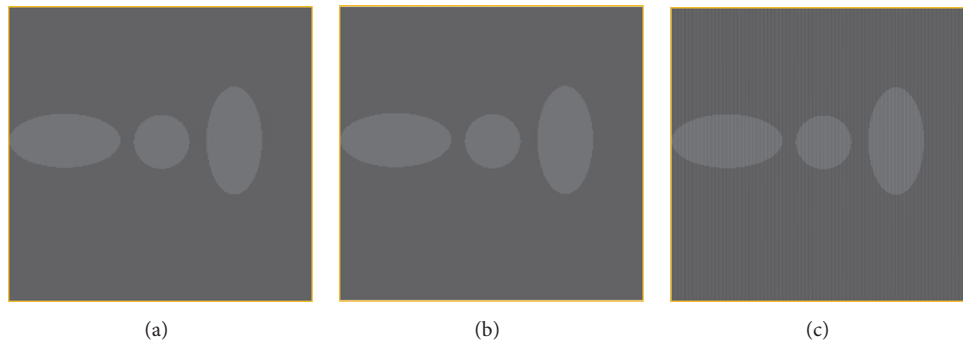


FIGURE 10: Images by block processing with the sizes of 128×128 , 256×256 and 512×512 , respectively.

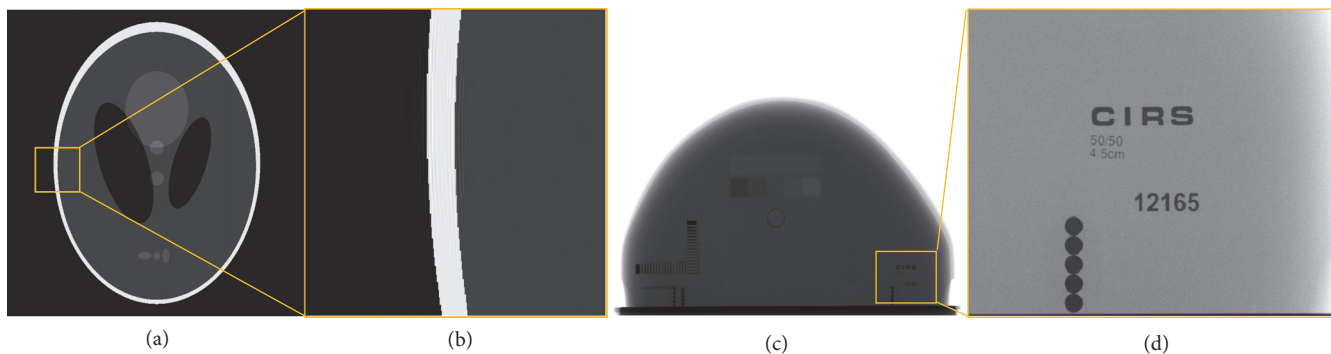


FIGURE 11: (a) Global simulation image by mean filter; (b) the corresponding magnified ROI of yellow squares in (a); (c) the real phantom image by mean filter; (d) the corresponding magnified ROI of yellow squares in (c).

a few ringing artifacts in simulated image due to the sharpness of gray value on the outline. However, in the real phantom experiment, these ringing artifacts almost disappeared visually as shown in Figure 11(d), which is the magnified ROI of yellow squares in Figure 11(c) by mean filter. And the filter results could basically be applied for clinical diagnosis. In the future, finding a better method to suppress ringing artifacts and grid artifacts will be the focus of our work.

5. Conclusion

In this study, the proposed integrated method, which has been tested in simulation system and the realistic systems, shows great potential for fast suppressing grid artifacts and generates high quality of digital mammography.

Conflicts of Interest

The authors declare that there are no conflicts of interest regarding the publication of this article.

Authors' Contributions

Qingqing Ling and Shuyu Wu contributed equally.

Acknowledgments

This work was supported by the National Key R&D Program of China (2016YFA0202003), National Natural Science

Foundation of China under Grants 81301940 and 81428019, Ministry of Science and Technology of China under Grant 2015BAI01B10, and Science and Technology Planning Project of Guangdong Province, China (2015A020214013).





References

- [1] W. H. Organization, "Breast cancer: prevention and control," *World Health Statistics Annual*, vol. 41, no. 7, pp. 697–700, 2012.
- [2] C. Fitzmaurice, D. Dicker, A. Pain et al., "The Global Burden of Cancer," *Oncology*, vol. 1, no. 4, pp. 505–527, 2013.
- [3] I. P. Collaborators, "Global, regional, and national incidence, prevalence, and years lived with disability for 310 diseases and injuries, 1990–2015: a systematic analysis for the Global Burden of Disease Study," *The Lancet*, vol. 388, no. 10053, pp. 1545–1602, 2015.
- [4] M. P. Coleman, D. Forman, H. Bryant et al., "Cancer survival in Australia, Canada, Denmark, Norway, Sweden, and the UK, 1995–2007 (the International Cancer Benchmarking Partnership): an analysis of population-based cancer registry data," *The Lancet*, vol. 377, no. 9760, pp. 127–138, 2011.
- [5] H. D. Nelson, K. Tyne, A. Naik, C. Bougatsos, B. K. Chan, and L. Humphrey, "Screening for breast cancer: an update for the U.S. Preventive Services Task Force," *Annals of Internal Medicine*, vol. 151, no. 10, pp. 727–737, 2009.
- [6] A. Sarvazyan, V. Egorov, J. S. Son, and C. S. Kaufman, "Cost-Effective Screening for Breast Cancer Worldwide: Current State and Future Directions," *Breast Cancer*, vol. 1, no. 1, p. 91, 2008.

- [7] Y. W. Chang, D. H. Kim, and M. H. Lee, "Usefulness of Preoperative Chest Multidetector CT for Evaluation of Breast Cancer: Comparison with Breast MRI," *Journal of the Korean Society of Radiology*, vol. 53, no. 2, p. 137, 2005.
- [8] A. Iesato, K. Murayama, T. Ito, K. Ito, and F. Takayama, "Diagnostic Value of Breast Magnetic Resonance Imaging in Cases Requiring Further Examination after Breast Cancer Screening," *Nihon Nyugan Kenshin Gakkaishi (Journal of Japan Association of Breast Cancer Screening)*, vol. 22, no. 3, pp. 411–418, 2013.
- [9] I. o. Medicine, N. R. C. C. o. t. E. D. o. B. Cancer, M. Patlak, S. J. Nass, I. C. Henderson, and J. C. Lashof, "Mammography and Beyond: Developing Technologies for the Early Detection of Breast Cancer: A Non-Technical Summary," *Breast Cancer Research*, vol. 4, no. 3, pp. 1–3, 2002.
- [10] N. Houssami, S. Ciatto, P. Macaskill et al., "Accuracy and surgical impact of magnetic resonance imaging in breast cancer staging: Systematic review and meta-analysis in detection of multifocal and multicentric cancer," *Journal of Clinical Oncology*, vol. 26, no. 19, pp. 3248–3258, 2008.
- [11] J. Beutel, H. L. Kundel, and R. L. Van Metter, *Handbook of medical imaging: Physics and psychophysics*, Spie Press, 2000.
- [12] R. G. Graves, "Principles of Radiological Physics by R. J. Wilks," *Medical Physics*, vol. 10, no. 6, pp. 918–918, 1983.
- [13] F. A. Riebel, "The Moire effect in radiography," *American Journal of Roentgenology Radium Therapy Nuclear Medicine*, vol. 115, no. 3, p. 641, 1972.
- [14] L. J. Cesar, B. A. Schueler, F. E. Zink, T. R. Daly, J. P. Taubel, and L. L. Jorgenson, "Artefacts found in computed radiography," *British Journal of Radiology*, vol. 74, no. 878, pp. 195–202, 2001.
- [15] D. R. Bednarek, S. Rudin, and R. Wong, "Artifacts produced by moving grids," *Radiology*, vol. 147, no. 1, pp. 255–258, 1983.
- [16] D. M. Gauntt and G. T. Barnes, "Grid line artifact formation: A comprehensive theory," *Medical Physics*, vol. 33, no. 6, pp. 1668–1677, 2006.
- [17] D. M. Gauntt and G. T. Barnes, "A novel technique to suppress grid line artifacts," *Medical Physics*, vol. 33, no. 6, pp. 1654–1667, 2006.
- [18] R. C. Gonzalez and R. E. Woods, *Digital Image Processing*, Prentice-Hall, Inc, 3rd edition, 2007.
- [19] J. Wang and H. K. Huang, "Film Digitization Aliasing Artifacts Caused by Grid Line Patterns," *IEEE Transactions on Medical Imaging*, vol. 13, no. 2, pp. 375–385, 1994.
- [20] L. L. Barski and X. Wang, "Characterization, detection and suppression of stationary grids in digital projection radiography imagery," in *Proceedings of the 1999 Medical Imaging - Image Display*, pp. 502–519, February 1999.
- [21] I. Belykh and C. W. Cornelius, "Antiscatter stationary grid artifacts automated detection and removal in projection radiography images," *Proceedings of SPIE - The International Society for Optical Engineering*, vol. 4322, no. 2, pp. 1162–1166, 2001.
- [22] R. Sasada, M. Yamada, S. Hara, H. Takeo, and K. Shimura, "Stationary grid pattern removal using 2-dimensional technique for Moiré-free radiographic image display," in *Proceedings of the Medical Imaging 2003: Visualization, Image-Guided Procedures and Display*, pp. 688–697, USA, February 2003.
- [23] C.-Y. Lin, W.-J. Lee, S.-J. Chen et al., "A study of grid artifacts formation and elimination in computed radiographic images," *Journal of Digital Imaging*, vol. 19, no. 4, pp. 351–361, 2006.
- [24] Z. Zhang, Y. Sheng, S. Zhuang et al., "Adaptively image destriping through frequency filtering," in *Proceedings of the ICO20:Optical Information Processing*, p. 60273V, Changchun, China.
- [25] D. S. Kim and S. Lee, "Grid artifact reduction for direct digital radiography detectors based on rotated stationary grids with homomorphic filtering," *Medical Physics*, vol. 40, no. 6, Article ID 061905, 2013.
- [26] D. S. Kim, "Modulation model for the analysis of the stationary grid artifacts in digital radiography imaging," in *Proceedings of the 7th IEEE International Symposium on Biomedical Imaging: From Nano to Macro, ISBI 2010*, pp. 768–771, Netherlands, April 2010.
- [27] D. S. Kim, N. J. Pelc, E. Samei, S. Lee, and R. M. Nishikawa, "Optimization of the grid frequencies and angles in digital radiography imaging," in *Proceedings of the SPIE Medical Imaging*, p. 79610B, Lake Buena Vista, Florida.
- [28] D. S. Kim and S. Lee, "Grid artifact reduction in radiography with arctan(1/2)-degree rotated grid," in *Proceedings of the 2010 17th IEEE International Conference on Image Processing, ICIP 2010*, pp. 1957–1960, Hong Kong, September 2010.
- [29] H. Tang, D. Tong, X. Dong Bao, and J.-L. Dillenseger, "A new stationary gridline artifact suppression method based on the 2D discrete wavelet transform," *Medical Physics*, vol. 42, no. 4, pp. 1721–1729, 2015.
- [30] P. S. Huang, S. C. Su, and T. M. Tu, "A Destriping and Enhancing Technique for EROS Remote Sensing Imagery," *Journal of Ccit*, 2004.
- [31] S. K. K. Mitra, *Digital Signal Processing: A Computer-Based Approach*, McGraw-Hill Higher Education, 2006.
- [32] R. Wimberger-Friedl, J. W. Mulder, and J. G. De Bruin, *Method for producing a grid structure*, US, 2004.
- [33] K. Bliznakova, R. Speller, J. Horrocks, P. Liaparinos, Z. Kolitsi, and N. Pallikarakis, "Experimental validation of a radiographic simulation code using breast phantom for X-ray imaging," *Computers in Biology and Medicine*, vol. 40, no. 2, pp. 208–214, 2010.

Research Article

Role of Magnetic Resonance Imaging in the Preoperative Staging and Work-Up of Patients Affected by Invasive Lobular Carcinoma or Invasive Ductolobular Carcinoma

Valeria Selvi,¹ Jacopo Nori,¹ Icro Meattini,² Giulio Francolini,² Noemi Morelli,¹ Diego Di Benedetto,¹ Giulia Bicchierai ,¹ Federica Di Naro,¹ Maninderpal Kaur Gill ,³ Lorenzo Orzalesi,⁴ Luis Sanchez,⁴ Tommaso Susini ,⁵ Simonetta Bianchi,⁶ Lorenzo Livi,² and Vittorio Miele ⁷

¹Diagnostic Senology Unit, Azienda Ospedaliero-Universitaria Careggi, University of Florence, Florence, Italy

²Radiation Oncology Unit, Azienda Ospedaliero-Universitaria Careggi, University of Florence, Florence, Italy

³University of Malaya, Kuala Lumpur, Malaysia

⁴Breast Surgery Unit, Azienda Ospedaliero-Universitaria Careggi, University of Florence, Florence, Italy

⁵Department of Gynecology, Perinatology and Human Reproduction, University of Florence, Florence, Italy

⁶Division of Pathological Anatomy, University of Florence, Florence, Italy

⁷Department of Emergency Radiology, Azienda Ospedaliero-Universitaria Careggi, University of Florence, Italy

Correspondence should be addressed to Giulia Bicchierai; giulia.bicchierai@gmail.com

Received 2 November 2017; Revised 22 May 2018; Accepted 3 June 2018; Published 26 June 2018

Academic Editor: Giuseppe Falco

Copyright © 2018 Valeria Selvi et al. This is an open access article distributed under the Creative Commons Attribution License, which permits unrestricted use, distribution, and reproduction in any medium, provided the original work is properly cited.

Purpose. The prevalence of invasive lobular carcinoma (ILC), the second most common type of breast cancer, accounts for 5%–15% of all invasive breast cancer cases. Its histological feature to spread in rows of single cell layers explains why it often fails to form a palpable lesion and the lack of sensitivity of mammography and ultrasound (US) to detect it. It also has a higher incidence of multifocal, multicentric, and contralateral disease when compared to the other histological subtypes. The clinicopathologic features and outcomes of Invasive Ductolobular Carcinoma (IDLC) are very similar to the ILC. The purpose of our study is to assess the importance of MRI in the preoperative management and staging of patients affected by ILC or IDLC. **Materials and Methods.** We identified women diagnosed with ILC or IDLC. We selected the patients who had preoperative breast MRI. For each patient we identified the areas of multifocal, multicentric, or contralateral disease not visible to standard exams and detected by preoperative MRI. We analyzed the potential correlation between additional cancer areas and histological cancer markers. **Results.** Of the 155 women who met our inclusion criteria, 93 (60%) had additional cancer areas detected by MRI. In 61 women, 39,4% of the overall population, the additional cancer areas were confirmed by US/tomosynthesis second look and biopsy. Presurgical MRI staging changed surgical management in the 37,4% of the patients. Only six patients of the overall population needed a reoperation after the initial surgery. No statistically significant correlation was found between MRI overestimation and the presence of histological peritumoral vascular/lymphatic invasion. No statistically significant correlation was found between additional cancer areas and histological cancer markers. **Conclusions.** Our study suggests that MRI is an important tool in the preoperative management and staging of patients affected by lobular or ductolobular invasive carcinoma.

1. Introduction

Breast cancer is the most frequent cancer in USA, with an estimated incidence of 296.980 new cases in 2013. The lifetime risk of developing a breast cancer is about 12%; yearly

screening mammograms are proposed in asymptomatic women with age > 40 [1, 2].

Invasive lobular carcinoma (ILC) is the second most common type of breast cancer. Its prevalence accounts for 5–15% of all invasive breast cancers, with a maximum incidence in

postmenopausal women. It has been found that the mean age of incidence is three years older than that of women affected by invasive ductal carcinoma (IDC) [3].

ILC has a typical histological growth behaviour. It arises from lobular epithelium and spreads as a single row of malignant cells along the breast ducts (Indian file manner), with weak desmoplastic reaction in surrounding connective stroma [3].

Due to these histological features, ILC often fails to present as a clinically palpable lesion, and it is often seen to spread diffusely through the breast stroma on mammography. Moreover, ILC spreading diffusely through the breast stroma leads to lower tendency to form round and circumscribed masses, only seen in 1%–3% of cases of ILC. Thus, ultrasound is more sensitive in detecting ILC [4, 5], with a reported sensitivity ranging from 68 to 98% [6].

On mammography, ILC is commonly characterized by the presence of asymmetry and architectural distortions with absence of calcifications [3]. Moreover ILC also tends to be isodense to normal adjacent breast parenchyma [5].

In view of these factors, mammography and ultrasound resulted in decreased diagnostic accuracy for ILC, with reported sensitivity ranging between 57 and 81% [4, 5].

MRI has a high sensitivity in the detection of breast cancer (over 90%) and it is well known for its increased diagnostic value in detecting multifocal, multicentric, or contralateral disease unrecognized on conventional exams [4]. Schelfout et al. reported that MRI detected 96% of multifocal/multicentric disease, while mammography and ultrasound only detected 28.6% and 26.5% respectively [7].

However, MRI also has a low specificity in detecting breast cancer [4], which can result in overtreatment (i.e., extensive surgery procedures), with no added advantages in terms of clinical outcome [8]. Furthermore, due to its limited availability and high cost [9], MRI is therefore best reserved only to a selected subgroup of patients.

MRI is a suitable diagnostic examination in the preoperative work-up and staging of ILC patients, due to the higher incidence of multifocal, multicentric, and contralateral disease, if compared to other histological subtypes [4]. However, the existing literature about this topic is rather sparse [10]. Ductolobular invasive carcinoma (IDLC) has similar clinic-pathologic features to ILC, with comparable outcomes [11].

For this reason, both ILC and IDLC were included in this analysis.

The aim of the current study is to assess the role of MRI in the preoperative staging and work-up of patients affected by ILC or IDLC.

2. Materials and Methods

The current study was a retrospective review of 163 patients. We included in the study all the patients with breast ILC or IDLC who had MRI studies prior to undergoing surgical therapy between January 2010 and July 2015, at the Breast Unit of Careggi Hospital, in Florence. Exclusions criteria were preoperative chemotherapy/radiotherapy administration or missing data.

Results of mammography (MRX), ultrasound (US), and MRI examinations of each patient were retrospectively reviewed, identifying areas of multifocal, multicentric, or contralateral disease detected only with MRI and not with standard exams (MRX or US). The results of MRX, US, and MRI examinations were scored according to the Breast Imaging Reporting and Data System (BIRADS) [12].

Patients underwent bilateral MRX and US before the MRI; size and position of the index lesion on both examinations were recorded.

Mammographic images were obtained in two standard planes: mediolateral oblique and craniocaudal using a dedicated equipment (Mammomat 2000, Siemens, Erlangen, Germany; Mammomat 3000 Nova, Siemens, Erlangen, Germany; Selenia Dimensions Hologic Inc., Bedford, USA).

Sonographic examination was performed using a broadband 10–13 Mhz linear transducer (Technos Mylab 70 XS; Esaote; Genoa, Italy).

All the MRI examinations were performed in prone position, with dedicated breast coils; A 1.5-Tesla equipment was used (Symphony®, Siemens Medical System, Erlangen, Germany; Philips Medical Systems, DA Best, The Nederland; Magnetom Avanto®, Siemens Medical System, Erlangen, Germany).

The size and position of the index lesion as well as any additional cancer areas detected on MRI were recorded. Regarding the size, the average diameter was chosen as the sizing reference for each lesion. The rate of change in the surgical management in view of the preoperative MRI findings was also recorded. Furthermore, reexcision rate after surgery was evaluated.

Histological diagnosis on surgical specimen performed at the local pathology department was reviewed; the data on the size of the index lesion and its histopathological features were assessed. The presence of peritumoral vascular/lymphatic invasion, ER, PGR and C-erb-2 status, and Ki67 were also collected.

3. Statistical Analysis

t-test was used to evaluate the significance of the differences observed using different diagnostic methods.

4. Results

Eight out of 163 women were excluded from the analysis (3 due to preoperative chemotherapy administration, 5 because of missing data). Thus the population of our study was composed of 155 patients.

Baseline characteristics of the population are summarized in Table 1.

When compared to MRX and US, MRI detected additional cancer areas in 93 out of 155 patients (60% of the overall population). Of these, additional cancer areas were confirmed with both US/tomosynthesis on second look and biopsy in only 61 patients (39,4% of the overall population; multifocal/multicentric and contralateral disease were found in 29,7% and 9,7% of patients, respectively). Presurgical MRI staging changed surgical management in the 37,4% of

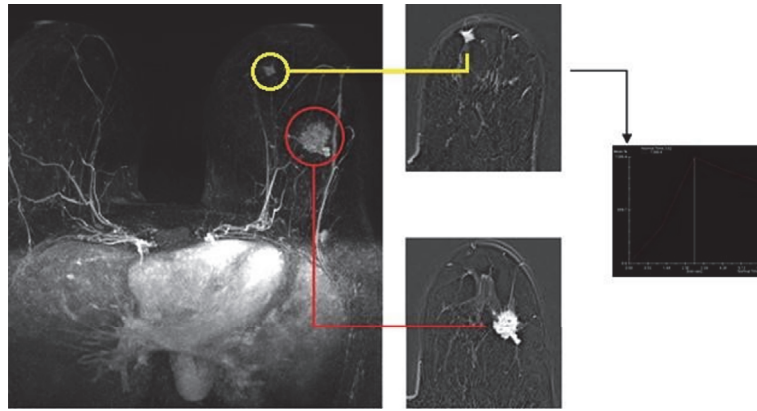


FIGURE 1: Index lesion (red circle; left SEQ, 28 mm), already documented with mammography and ultrasound. MRI leads to the detection of multicentric disease, confirmed to US second look and biopsy (yellow circle: left IIQ, 9 mm) (SEQ: Superior External Quadrant; IIQ: Inferior Internal Quadrant).

TABLE 1: Population description.

Number of patients	155
Median age (range)	53 (31–82)
Histology	ILC: 55% IDLC: 45%
Site of index lesion	SEQ: 49,3% SIQ: 14,6% IEQ: 13,2% IIQ: 6,8% CQ: 16,1%

ILC: Invasive Lobular Carcinoma; IDLC: Invasive Ductolobular Carcinoma; SEQ: Superior External Quadrant; SIQ: Superior Internal Quadrant; IEQ: Inferior External Quadrant; IIQ: Inferior Internal Quadrant; CQ: Central Quadrant; MRI: Magnetic Resonance Imaging.

the patients; 27,4% underwent a wider exeresis/mastectomy instead of initially planned breast-conservative surgery, and 9,7% required also contralateral surgery. Only six patients of the overall population needed a reoperation after the initial surgery: mastectomy was performed in 5 patients because of positive margins after breast-conservative surgery, while one patient required bilateral mastectomy after breast-conservative surgery, due to the presence of BRCA1 mutation. Among the patients who needed to be reoperated on because of positive margins, three patients have had diagnosis of additional cancer area with the MRI performed before the initial surgery, later confirmed with US/tomosynthesis on second look and biopsy. Instead the other two presented the index lesion only and MRI had not added any further diagnostic information to MRX and US. Regarding the false positive patients, in whom the additional cancer areas detected by MRI were not confirmed on US/tomosynthesis second look, none of them presented a local recurrence. MRI performances are summarized in Table 2; in the Appendix there is the MRI documentation of three of the patients studied (Figures 1–3).

Average size of index lesion was 18 mm (range 2–40 mm), 14 mm (range 4–60 mm), and 22 mm (range 6–85 mm) on preoperative MRX, US, and MRI, respectively

The average size of the index lesion measured on surgical specimen was 17 mm (range 2,3–75mm). Difference of lesion size was significantly lower for mammography when compared to US and MRI; US showed a size underestimation rate of 18% while the MRI demonstrated an overestimation rate of 26% and mammography an overestimation rate of only 5% ($p < 0,001$) (Table 3).

Overall sensitivity and specificity of MRI in this setting were 91,04% and 92,4%, respectively. No correlation was found between MRI overestimation and the presence of histological peritumoral vascular/linfatic invasion. No correlation was found in the presence of additional areas detected by MRI and ER status ($p = 0,103$), PGR status ($p = 0,218$), Ki67 (0,668), or C-erb-2 status ($p = 0,955$) (Table 4).

5. Discussion

Results from the current analysis showed that if compared to MRX and US, preoperative MRI detected additional disease in 39,4% of patients, with 29,7% and 9,7% of the patients showing ipsilateral or contralateral undetected areas, respectively. Preoperative MRI had an overall sensitivity of 91,04%, confirming data from literature demonstrating the good performance of this examination in the preoperative setting of ILC and IDLC. Indeed previous series reported a sensitivity of 95% for MRI. [9, 13, 14].

These results therefore support the previous literature data on the superiority of MRI in detecting multifocal, multicentric, and contralateral disease, when compared to MRX and US [9, 15].

Due to the typical growth pattern of ILC/IDLC, with increased likelihood of multifocal, multicentric, and contralateral disease [10], MRI could have a key role in preoperative staging of these patients. In the 37,4% of our patients a change in surgical management was documented. Thus, targeted use of MRI in patients with ILC/IDLC could improve

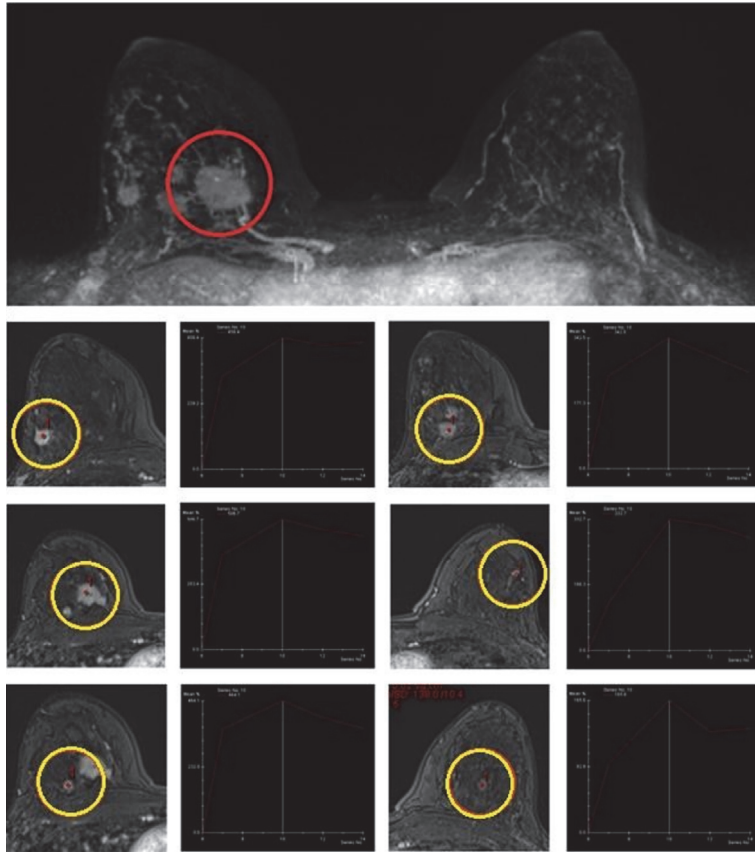


FIGURE 2: Index lesion (red circle; right SIQ, 27 mm), already documented with ultrasound. MRI leads to the detection of multifocal and multicentric disease, confirmed to US second look and biopsy (yellow circles: right SIQ, 6mm; right SEQ, 11mm; right CEQ, 10 mm; right CEQ dx, 11 mm; right CEQ dx, 5mm). Subcentimetric mass enhancement in the left breast resulted as negative to US second look. SEQ: Superior External Quadrant; SIQ: Superior Internal Quadrant; CEQ: Central External Quadrant.

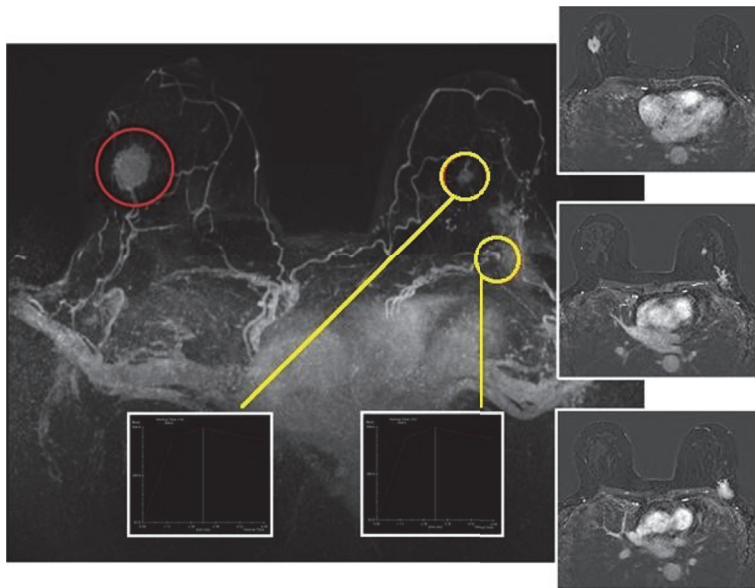


FIGURE 3: Index lesion (red circle; right IEQ, 30 mm), already documented with mammography and ultrasound. MRI leads to the detection of contralateral disease, confirmed to US second look and biopsy (yellow circle: left CEQ, 40 mm; left CEQ, 13 mm) (Inferior External Quadrant; IEQ: CEQ: Central External Quadrant).

TABLE 2: Summary of MRI performances.

	Patients (%)
Additional areas of disease found on MRI (%)	93 (60%)
Multifocal/multicentric disease (%)	46 (29,7%)
Additional cancer areas confirmed on second look exams and biopsy	61 (39,4%)
Contralateral disease	15 (9,6%)
Change in surgical management	58 (37,4%)
Reoperation rate	6 (3,9%)

TABLE 3: Comparison in lesion size.

	Average size (mm)	Range (mm)	Comparison with surgical specimen	p
MRX	18	2-40	+5%	
US	14	4-60	-18%	<0,001
MRI	21,25	6-70	+26%	
Surgical specimen	16,95	2,3-75	0	

TABLE 4: Relationship between additional cancer areas on MRI and Tumor histopathologic features.

Additional cancer areas	Presence of additional cancer areas	Absence of additional cancer areas	P
ER+ %	n of patients %	n of patients %	
≥ 80	98,1	98,7	
<80	1,9	1,3	
TOTAL	100	100	0,103
PgR+ %	n of patients %	n of patients %	
≥ 80	71,2	72,8	
<80	28,8	27,2	
TOTAL	100	100	0,218
HER2	n of patients %	n of patients %	
Positive 3+	3,6	6,3	
Negative 0/1+	52,7	53,2	
Doubt 2+	43,6	40,5	
Total	100	100	0,668

surgical planning, leading a lower rate of reoperation. Other authors achieved similar results too. A population based study conducted on the SEER database showed that preoperative MRI in this setting yielded a better surgical planning [8]. A meta-analysis of 18 studies reported that MRI detected additional disease in 32% of patients, with a subsequent change in surgical management in 28% of women [13]. More recent retrospective reports on ILC patients confirmed that high sensitivity of preoperative MRI in detecting multicentric and contralateral disease yielded a more appropriate surgical management plan [10].

Summarizing, the main aim of our analysis was testing the hypothesis that certain ILC/IDLC histological features could lead to a particular growth pattern, in which MRI could have an increased diagnostic sensitivity. The current study confirms our starting hypothesis.

Data from previous reports have confirmed the advantages of MRI in the preoperative assessment of patients with ILC [5, 6, 8, 10, 11, 15–20].

Furthermore, not all the authors agree that MRI improved sensitivity translated into short-term surgical outcome or long-term patient benefit [21].

This has also been reflected in the disagreements seen between the different guidelines in recent years; European Society of Breast Imaging [22] and EUSOMA working group [23] guidelines suggest a strong recommendation for the use of preoperative MRI for ILC. However, the American College of Radiology guidelines [24], later updated in 2013 [25], do not provide any recommendation about the use of preoperative MRI in patients affected by ILC, reporting insufficient evidence about this topic.

We evaluated also the size of the lesions and the difference between diagnostic imaging.

In the current study, the size of the lesion is significantly overestimated and underestimated with MRI and US, respectively, when compared to average size measured on surgical specimen; instead lesion size measured on MRX and the surgical specimen were relatively similar.

In the previous literature reviews, other authors have emphasised the trend for MRI overestimation of lesion size [3, 11, 26]. Conversely, some reports suggested that MRI could have a higher accuracy in determining tumour size if compared to MRX and US [7, 27].

We hypothesized the MRI overestimation we detected, could be explained by the presence of histological peritumoral vascular/lymphatic invasion. However, no correlation was found between MRI overestimation and this histological feature. To our knowledge, this is the first study testing the correlation between MRI overestimation of the size and histological features of the index lesion. We hypothesized also that the presence of additional cancer areas detected by MRI could be correlated to the presence of certain histological cancer markers. To our knowledge, this is the first study testing this topic; anyway no correlation was documented.

6. Conclusion

Results from this study show that MRI is a useful tool in the preoperative staging and surgical planning of patients affected by ILC/IDLC. MRI is very sensitive in the detection of multifocal, multicentric, and contralateral disease; it provides additional diagnostic information that is missed with the standard imaging modalities (MRX, US). Thus the targeted use of preoperative breast MRI in patients with a proven biopsy diagnosis of ILC or IDLC could significantly improve the surgical approach, allowing a more appropriate oncologic resection.

The retrospective nature of this study could anyway weaken these results. Prospective data on a larger study population are needed to better evaluate MRI performance in this setting; a randomized controlled trial is aimed to be organized in order to confirm the results that our study suggest.

Conflicts of Interest

The authors declare that there are no conflicts of interest regarding the publication of this paper.

References

- [1] T. Schwartz, A. Cyr, and J. Margenthaler, "Screening breast magnetic resonance imaging in women with atypia or lobular carcinoma in situ," *Journal of Surgical Research*, vol. 193, no. 2, pp. 519–522, 2015.
- [2] E. R. Port, A. Park, P. I. Borgen, E. Morris, and L. L. Montgomery, "Results of MRI screening for breast cancer in high-risk patients with LCIS and atypical hyperplasia," *Annals of Surgical Oncology*, vol. 14, no. 3, pp. 1051–1057, 2007.
- [3] T. M. G. Oliveira, J. Elias Jr., A. F. Melo et al., "Evolving concepts in breast lobular neoplasia and invasive lobular carcinoma, and their impact on imaging methods," *Insights into Imaging*, vol. 5, no. 2, pp. 183–194, 2014.
- [4] G. L. G. Menezes, F. M. Knuttel, B. L. Stehouwer, R. M. Pijnappel, and M. A. A. J. Van Den Bosch, "Magnetic resonance imaging in breast cancer: A literature review and future perspectives," *World Journal of Clinical Oncology*, vol. 5, no. 2, pp. 61–70, 2014.
- [5] M. Muttalib, R. Ibrahim, A. S. Khashan, and M. Hajaj, "Prospective MRI assessment for invasive lobular breast cancer. Correlation with tumour size at histopathology and influence on surgical management," *Clinical Radiology*, vol. 69, no. 1, pp. 23–28, 2014.
- [6] C. P. Paramagul, M. A. Helvie, and D. D. Adler, "Invasive lobular carcinoma: Sonographic appearance and role of sonography in improving diagnostic sensitivity," *Radiology*, vol. 195, no. 1, pp. 231–234, 1995.
- [7] K. Schelfout, M. Van Goethem, E. Kersschot et al., "Preoperative breast MRI in patients with invasive lobular breast cancer," *European Radiology*, vol. 14, no. 7, 2004.
- [8] A. K. Fortune-Greeley, S. B. Wheeler, A.-M. Meyer et al., "Pre-operative breast MRI and surgical outcomes in elderly women with invasive ductal and lobular carcinoma: A population-based study," *Breast Cancer Research and Treatment*, vol. 143, no. 1, pp. 203–212, 2014.
- [9] J. K. Lopez and L. W. Bassett, "Invasive lobular carcinoma of the breast: spectrum of mammographic, US, and MR imaging findings," *RadioGraphics*, vol. 29, no. 1, pp. 165–176, 2009.
- [10] M. Derias, A. Subramanian, S. Allan, E. Shah, H. E. Terafi, and D. Howlett, "The Role of Magnetic Resonance Imaging in the Investigation and Management of Invasive Lobular Carcinoma—A 3-Year Retrospective Study in Two District General Hospitals," *The Breast Journal*, vol. 22, no. 4, pp. 384–389, 2016.
- [11] G. L. G. Menezes, M. A. A. J. van den Bosch, E. L. Postma et al., "Invasive ductolobular carcinoma of the breast: Spectrum of mammographic, ultrasound and magnetic resonance imaging findings correlated with proportion of the lobular component," *SpringerPlus*, vol. 2, no. 1, pp. 1–12, 2013.
- [12] E. A. Sickles, C. J. D'Orsi, L. W. Bassett et al., *ACR BI-RADS® Mammography. In: ACR BIRADS® Atlas, Breast Imaging Reporting and Data System*, American College of Radiology, Reston, VA, 2013.
- [13] R. M. Mann, Y. L. Hoogveen, J. G. Blickman, and C. Boetes, "MRI compared to conventional diagnostic work-up in the detection and evaluation of invasive lobular carcinoma of the breast: a review of existing literature," *Breast Cancer Research and Treatment*, vol. 107, no. 1, pp. 1–14, 2007.
- [14] P. J. Kneeshaw, L. W. Turnbull, and P. J. Drew, "Current applications and future direction of MR mammography," *British Journal of Cancer*, vol. 88, no. 1, pp. 4–10, 2003.
- [15] R. M. Mann, "The Effectiveness of MR Imaging in the Assessment of Invasive Lobular Carcinoma of the Breast," *Magnetic Resonance Imaging Clinics of North America*, vol. 18, no. 2, pp. 259–276, 2010.
- [16] I. V. Gruber, M. Rueckert, K. O. Kagan et al., "Measurement of tumour size with mammography, sonography and magnetic resonance imaging as compared to histological tumour size in primary breast cancer," *BMC Cancer*, vol. 13, article no. 328, 2013.
- [17] C. Boetes, R. D. M. Mus, R. Holland et al., "Breast tumors: comparative accuracy of MR imaging relative to mammography and ultrasound for demonstrating extent," *Radiology*, vol. 197, no. 3, pp. 743–747, 1995.
- [18] W. A. Berg, L. Gutierrez, M. S. NessAiver et al., "Diagnostic accuracy of mammography, clinical examination, US, and MR

- imaging in preoperative assessment of breast cancer," *Radiology*, vol. 233, no. 3, pp. 830–849, 2004.
- [19] R. S. Butler, L. A. Venta, E. L. Wiley, R. L. Ellis, P. J. Dempsey, and E. Rubin, "Sonographic evaluation of infiltrating lobular carcinoma," *American Journal of Roentgenology*, vol. 172, no. 2, pp. 325–330, 1999.
- [20] C. Chapellier, C. Balu-Maestro, A. Bleuse, F. Ettore, and J. N. Bruneton, "Ultrasonography of invasive lobular carcinoma of the breast: Sonographic patterns and diagnostic value. Report of 102 cases," *Clinical Imaging*, vol. 24, no. 6, pp. 333–336, 2000.
- [21] M. Pilewskie and T. A. King, "Magnetic resonance imaging in patients with newly diagnosed breast cancer: A review of the literature," *Cancer*, vol. 120, no. 14, pp. 2080–2089, 2014.
- [22] R. M. Mann, C. K. Kuhl, K. Kinkel, and C. Boetes, "Breast MRI: guidelines from the European society of breast imaging," *European Radiology*, vol. 18, no. 7, pp. 1307–1318, 2008.
- [23] F. Sardanelli, C. Boetes, and B. Borisch, "Magnetic resonance imaging of the breast: recommendations from the EUSOMA working group," *European Journal of Cancer*, vol. 46, no. 8, pp. 1296–1316, 2010.
- [24] D. Saslow, C. Boetes, W. Burke et al., "American Cancer Society Guidelines for Breast Screening with MRI as an Adjunct to Mammography," *CA: A Cancer Journal for Clinicians*, vol. 57, no. 2, pp. 75–89, 2007.
- [25] American College of Radiology (ACR), ACR practice guideline for the performance of contrast-enhanced magnetic resonance imaging (MRI) of the breast. 2013. <http://www.acr.org>.
- [26] N. Biglia, V. E. Bounous, L. Martincich et al., "Role of MRI (magnetic resonance imaging) versus conventional imaging for breast cancer presurgical staging in young women or with dense breast," *European Journal of Surgical Oncology*, vol. 37, no. 3, pp. 199–204, 2011.
- [27] M. A. Parvaiz, P. Yang, E. Razia et al., "Breast MRI in invasive lobular carcinoma: A useful investigation in surgical planning?" *The Breast Journal*, vol. 22, no. 2, pp. 143–150, 2016.

Research Article

Use of a Total Variation Minimization Iterative Reconstruction Algorithm to Evaluate Reduced Projections during Digital Breast Tomosynthesis

Tsutomu Gomi ¹ and Yukio Koibuchi²

¹School of Allied Health Sciences, Kitasato University, Sagamihara, Kanagawa, Japan

²Breast and Endocrine Surgery, National Hospital Organization Takasaki General Medical Center, Takasaki, Gunma, Japan

Correspondence should be addressed to Tsutomu Gomi; gomi@kitasato-u.ac.jp

Received 21 January 2018; Revised 28 April 2018; Accepted 12 May 2018; Published 19 June 2018

Academic Editor: Graziella Di Grezia

Copyright © 2018 Tsutomu Gomi and Yukio Koibuchi. This is an open access article distributed under the Creative Commons Attribution License, which permits unrestricted use, distribution, and reproduction in any medium, provided the original work is properly cited.

Purpose. We evaluated the efficacies of the adaptive steepest descent projection onto convex sets (ASD-POCS), simultaneous algebraic reconstruction technique (SART), filtered back projection (FBP), and maximum likelihood expectation maximization (MLEM) total variation minimization iterative algorithms for reducing exposure doses during digital breast tomosynthesis for reduced projections. *Methods.* Reconstructions were evaluated using normal (15 projections) and half (i.e., thinned-out normal) projections (seven projections). The algorithms were assessed by determining the full width at half-maximum (FWHM), and the BR3D Phantom was used to evaluate the contrast-to-noise ratio (CNR) for the in-focus plane. A mean similarity measure of structural similarity (MSSIM) was also used to identify the preservation of contrast in clinical cases. *Results.* Spatial resolution tended to deteriorate in ASD-POCS algorithm reconstructions involving a reduced number of projections. However, the microcalcification size did not affect the rate of FWHM change. The ASD-POCS algorithm yielded a high CNR independently of the simulated mass lesion size and projection number. The ASD-POCS algorithm yielded a high MSSIM in reconstructions from reduced numbers of projections. *Conclusions.* The ASD-POCS algorithm can preserve contrast despite a reduced number of projections and could therefore be used to reduce radiation doses.

1. Introduction

Digital tomosynthesis combines the benefits of digital imaging [1, 2] with the tomographic benefits of computed tomography to provide three-dimensional (3D) structural information. This technique can easily be performed in conjunction with radiography to reduce both the radiation doses and associated costs. Digital breast tomosynthesis (DBT) thus provides 3D structural information by reconstructing an entire image volume from a sequence of projection-view mammograms acquired within a small number of projection angles over a limited angular range. As DBT reduces the camouflaging effects of overlapping fibroglandular breast tissue, thereby improving the conspicuity of subtle lesions, its use could potentially improve the rate of early breast cancer detection [2–4]. Several digital mammography-based DBT

systems have been developed [5], and this technology is the focus of currently ongoing preliminary clinical studies [2, 6].

In previous studies of DBT, Wu et al. evaluated the conventional reconstruction algorithm (filtered back projection; FBP [7]), statistical iterative reconstruction (IR) algorithms (maximum likelihood expectation maximization; MLEM [3]), and simultaneous IR algorithms (the simultaneous iterative reconstruction technique; SIRT [8]). The results led Wu and colleagues to conclude that the MLEM algorithm provides a good balance of image quality between low- and high-frequency features [3]. Other reports have explored various DBT reconstruction methods [7, 9, 10] or have proposed options for suppressing irrelevant plane information and enhancing DBT image quality [11, 12]. Specifically, DBT reconstruction involves inconsistent images limited by a low signal-to-noise ratio consequent to the superposition of

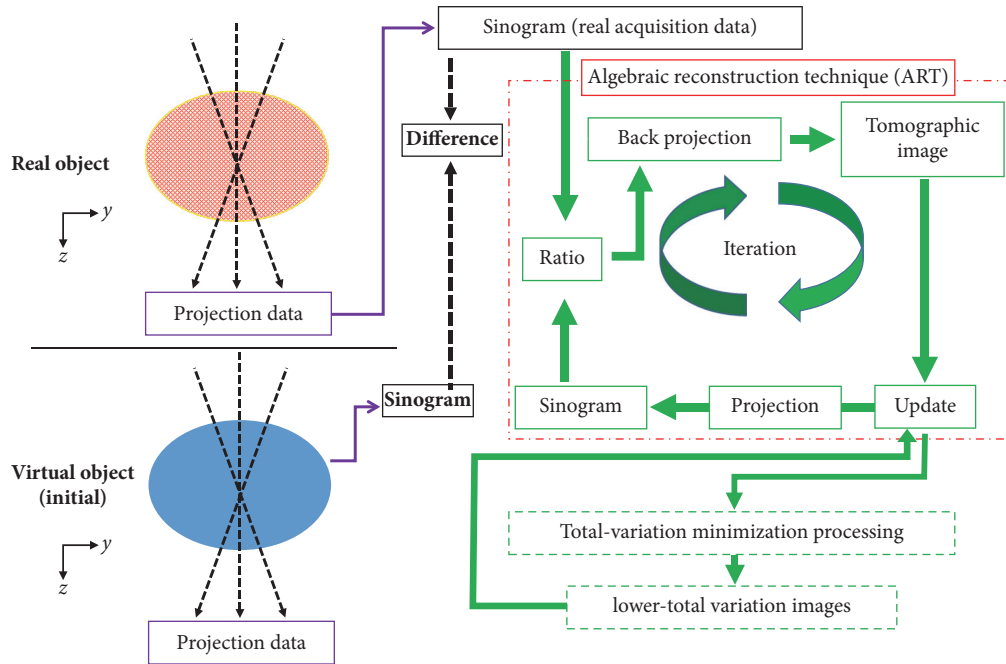


FIGURE 1: The total variation minimization concept based on the adaptive steepest descent projection onto the convex sets reconstruction algorithm for digital breast tomosynthesis.

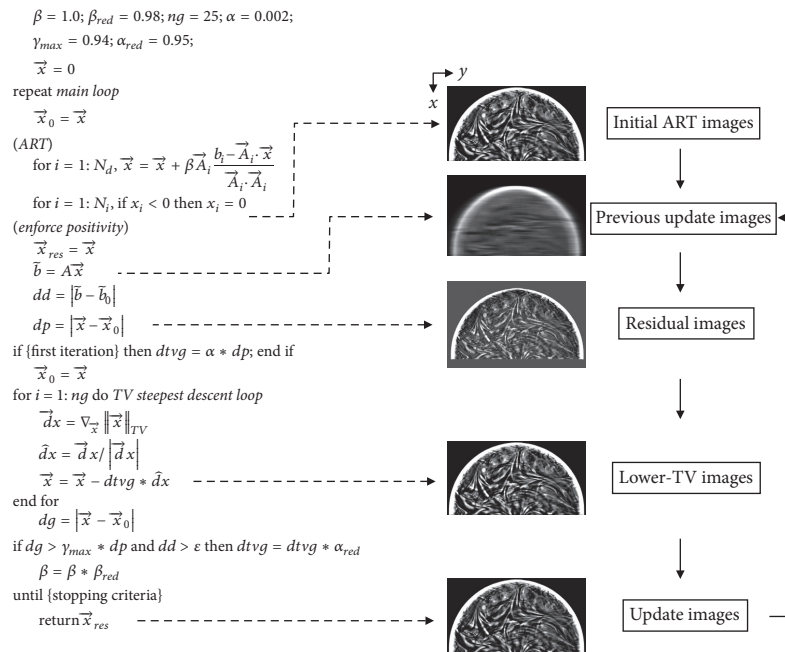


FIGURE 2: The adaptive steepest descent projection onto the convex sets algorithm in the form of a pseudocode. β : the ART operator depends on the relaxation parameter. β_{red} : the ART-relaxation parameter is reduced by a constant fraction. α : total variation (TV) hyperparameter. $\alpha_{red}, \gamma_{max}$: these variables control the evolution of α . ng : iteration number for the TV-steepest descent. Image-space variables are denoted by a vector sign (e.g., \vec{x}). Data-space variables are denoted by a tilde (e.g., \vec{b}). The vector \vec{A}_i is the row of the system matrix that produces the i th data element. \vec{b}_0 is the optimization problem specified by the projection. ϵ is the data-inconsistency-tolerance parameter (reference: Sidky EY, Pan X. Image reconstruction in circular cone-beam computed tomography by constrained, total variation minimization. Phys Med Biol, 2008; 53: p.4788).

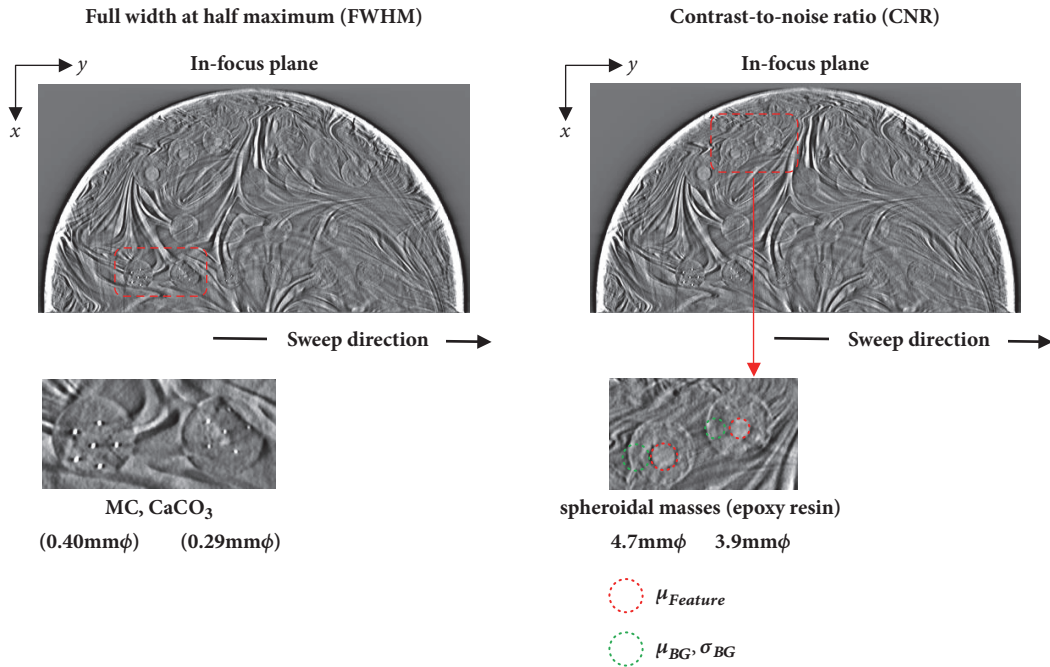


FIGURE 3: Areas where the full width at half-maximum and contrast-to-noise ratio were measured in a reconstructed image of the BR3D Phantom (in-focus plane).

several low-exposure projection images. The concurrent loss of plane-relevant details yields reconstructed images with poor contrast.

Two research objectives have been identified as a consequence of the increasing spread of DBT in clinical practice: estimation of the risk of radiation-induced cancer and characterization of the image qualities of DBT systems to understand the similarities and differences with respect to standard two-dimensional (2D) full-field digital mammography (FFDM). Although both objectives remain under debate [13], Ferreira et al. [14] demonstrated an increase in the risk of induced lung cancer with the DBT scan relative to FFDM, especially if the beam energy has not been optimized in terms of the image quality and absorbed dose [15].

Regarding image quality, a factor called quantum mottle causes spatial incident photon fluctuations and, consequently, radiographic image degradation. As quantum mottle increases at lower levels of exposure, reductions in the doses to patients would be restricted by the degree of quantum mottle even in a perfect detector. Noise also affects the visibility and detectability of subtle microcalcifications (MCs) and masses in reconstructed DBT images. Therefore, a new algorithm that improves image quality via suitable processing would further reduce patient doses and improve detection.

To overcome the above-described limitations, several noise suppression techniques for DBT reconstruction have been proposed [16–19]. Recently, an iterative algorithm based on total variation- (TV-) based compressive sensing was developed for volume image reconstruction from tomographic scans [20–24]. TV is defined as the sum of the first-order derivative magnitudes for all pixels in the image, and TV image has been used as a penalty term in iterative image

reconstruction algorithms [24]. TV-minimization is an image domain optimization method associated with compressed sensing theory [22, 24]. Adaptive steepest descent projection onto convex sets (ASD-POCS), a TV-minimization iterative reconstruction (IR) algorithm for image reconstruction, provides a partial solution to the problem of constrained TV-minimization [22]. In TV-minimization IR, the addition of a penalty to the data-fidelity-objective function smooths noise in the image while preserving the internal edges [20–25]. Therefore, TV-minimization IR can preserve contrast while reducing both projection data and radiation doses.

In this study, we evaluated the abilities of four reconstruction algorithms to reduce radiation dose from normal and half projections (i.e., thinned-out normal): a novel TV-minimization IR algorithm (ASD-POCS) and three conventional reconstruction algorithms (FBP, statistical IR-MLEM, and SIRT algorithm algebraic IR-simultaneous algebraic reconstruction technique; SART) [23]). Specifically, we compared the level of contrast preservation when reconstructing a reduced number of projections of both breast phantoms and clinical cases.

2. Materials and Methods

2.1. Digital Breast Tomosynthesis. This study used a DBT system (Selenia Dimensions; Hologic Inc., Bedford, MA, USA) comprising an X-ray tube with a 0.3-mm focal spot (tube target: W, filtration: 0.7-mm aluminum equivalent) and a digital flat-panel amorphous selenium detector. A total acquisition time of 3.7 s and acquisition angle of 15° were set for DBT procedures. Normal projection

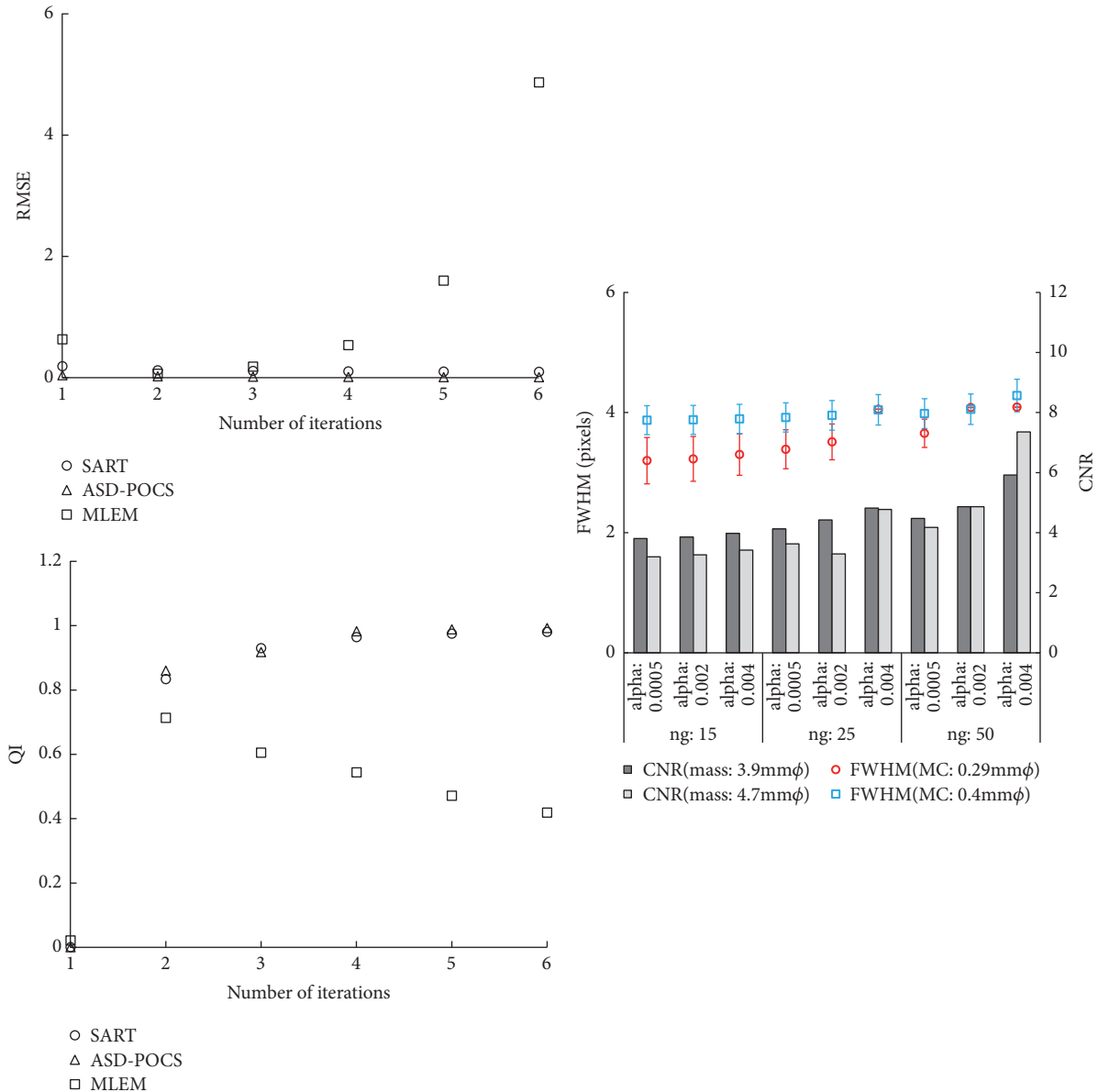


FIGURE 4: At right, the full width at half-maximum (FWHM) and contrast-to-noise ratio (CNR) characteristics caused by differences in parameters [TV hyperparameter (α), iteration number for TV-steepest descent (ng)] in the ASD-POCS algorithm (error bar represents the standard error). At left, the root-mean-square error (RMSE) and universal image quality index (QI) characteristics caused by differences in the numbers of iterations in each reconstruction algorithm.

images were sampled during a single tomographic pass (15 projections), while half projection images (seven projections) were generated by thinning out normal projection data.

2.2. Phantom Specifications. The BR3D Phantom (Model 020; Computerized Imaging Reference Systems, Inc., Norfolk, VA, USA), which comprises multiple heterogeneous slabs, is intended to mimic the composition of glandular and adipose tissues and parenchymal patterns in the human breast. The slabs are composed of epoxy resins with X-ray attenuation properties corresponding to 50% glandular or 50% adipose

breast tissue. The target slab was surrounded by nontarget slabs (top, 30 mm and bottom, 10 mm).

2.3. Radiation Dose Measurement. The following settings were implemented during each radiation dose setup: a reference radiation dose [automatic exposure control (AEC) = exposure condition at 40-mm thickness and predetermined tube voltage and current] at 28 kVp and 50 mA (15 projections). The average glandular dose (AGD) was calculated using the method proposed by Dance et al. [26] and a Piranha dosimeter (RTI Electronics AB, Mölndal, Sweden) to measure radiation exposure. Measured radiation doses were

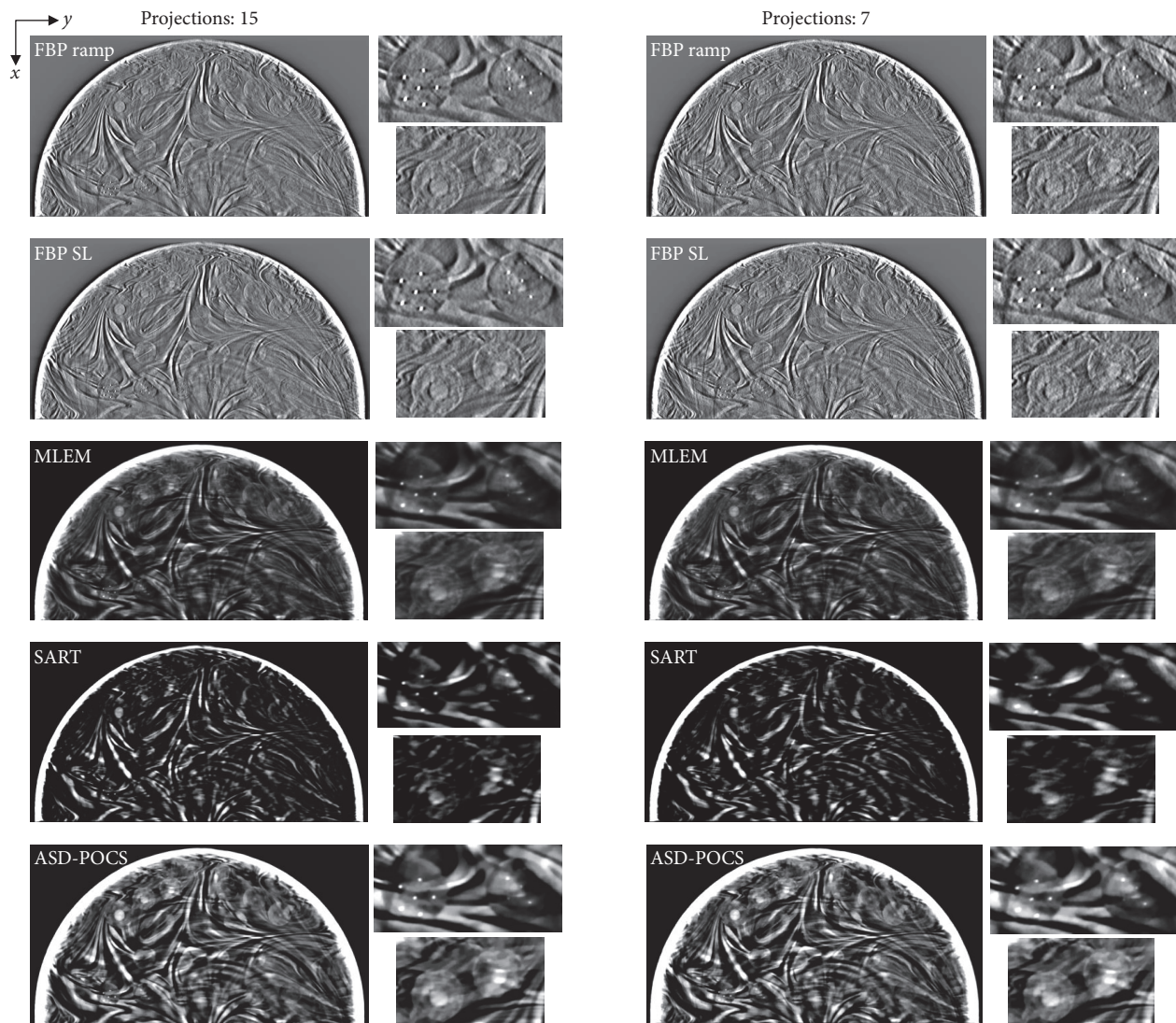


FIGURE 5: Comparisons between different projection number (normal: 15, half: seven) images obtained using each tomosynthesis reconstruction algorithm in the in-focus plane. The X-ray source was moved horizontally along the image. Zoomed images: microcalcifications, spheroidal masses. For corresponding images, the IR (MLEM, SART, and ASD-POCS) images are displayed at the same window width and level, whereas the FBP images have a larger window widths because the backgrounds are less flattened and the gray levels in larger areas would be out of scale in narrower windows.

used to convert the established exposure condition into the AGD; the latter value was 1.51 mGy.

2.4. Reconstruction Algorithm. In this study, we used MATLAB (Mathworks; Natick, MA, USA) to perform the FBP, SART, MLEM, and ASD-POCS image reconstruction calculations [27]. The reconstruction data comprised real projection data acquired on a DBT system.

Two-dimensional (2D) image filtering, which multiplies the Fourier transform by a Ramp or SL filter kernel, was used to restore the impulse shape of the reconstructed image. A conventional Ramp or SL filter kernel and the FBP algorithm, which generally produces precise 3D reconstruction images [7], were used to yield FBP images in this study. In contrast to the single-step back projection and FBP algorithms, IR

algorithms perform a recursive reconstruction [9]. Specifically, IR iteratively updates the unknown linear attenuation coefficients by minimizing errors between the measured and calculated projection data.

Previous studies have investigated algebraic reconstruction technique (ART) methodologies [8]. An ART rapidly converges by updating the linear attenuation coefficients from a single projection value at each time point. However, the least-squares solution can yield considerable noise if the inverse problem is very poorly posed (e.g., limited angle reconstruction). Several improvements to ART have been proposed to address this issue. For instance, modifications of ART may be compatible with other methods, such as SIRT [8], depending on the projection data volume and the method used to update the given estimation. Notably, SART

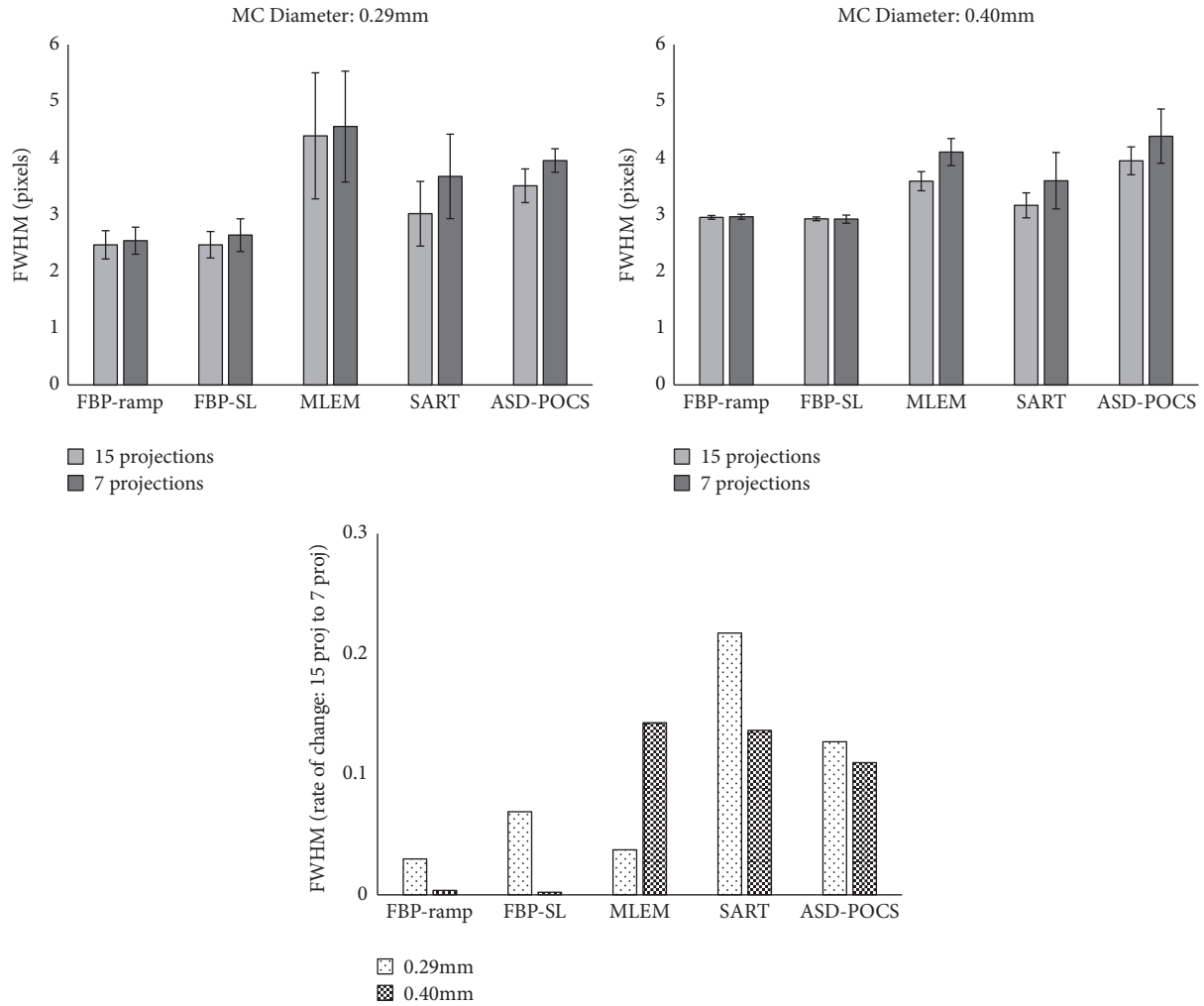


FIGURE 6: Comparisons of the full width at half-maximum (FWHM) and rate of change between normal (15) and half (seven) projections in the in-focus plane images obtained via tomosynthesis under different projection numbers and generated using different reconstruction algorithms. The error bar represents the standard error.

represents a compromise between ART and SIRT that yields acceptable algorithm stability and convergence in the same process. MLEM methods comprising two steps per iteration (e.g., a forward step for DT acquisition process modeling and backward step for reconstructed object updating) have also been proposed. These methods are applied iteratively, such that the reconstructed volume projections computed from an image formation model will resemble the experimental projections.

Another ART is the ASD-POCS algorithm step that improves data consistency, in which basic projection enforces positivity. ASD-POCS minimizes the TV norm separately in each iteration; in other words, the image is first reconstructed, followed by a reduction in the TV norm at each iteration. To nudge the image toward a minimum-TV solution, POCS steps are alternated with the TV-steepest descent [22]. If the TV-minimization step alone was run during the rest of the algorithms, the result would be a flat image. Alternatively, the ROF model ensures that the image is not significantly

altered. The importance of these optimal parameters with respect to image quality has been demonstrated in previous studies [22, 24]. Here, we used optimal parameters for the ASD-POCS algorithms to preserve the edges. Figures 1 and 2 depict the ASD-POCS algorithm in the form of a pseudocode and overview, respectively.

2.5. Phantom Evaluation. We calculated the full width at half-maximum (FWHM) and contrast-to-noise ratio (CNR) to evaluate the effects of contrast preservation on each phantom image featured in the in-focus plane. The spatial resolution derived from the FWHM in the in-focus plane (0.29 and 0.40 mm φ ; CaCO_3) was evaluated as a quantitative measure of the reconstructed image quality, after which the FWHM of the selected intensity profiles intersecting the three MCs on reconstructed DBT slices were measured. To obtain the intensity profile, three neighboring vertical lines intersecting the MCs (perpendicular to the X-ray sweep direction) were arranged.

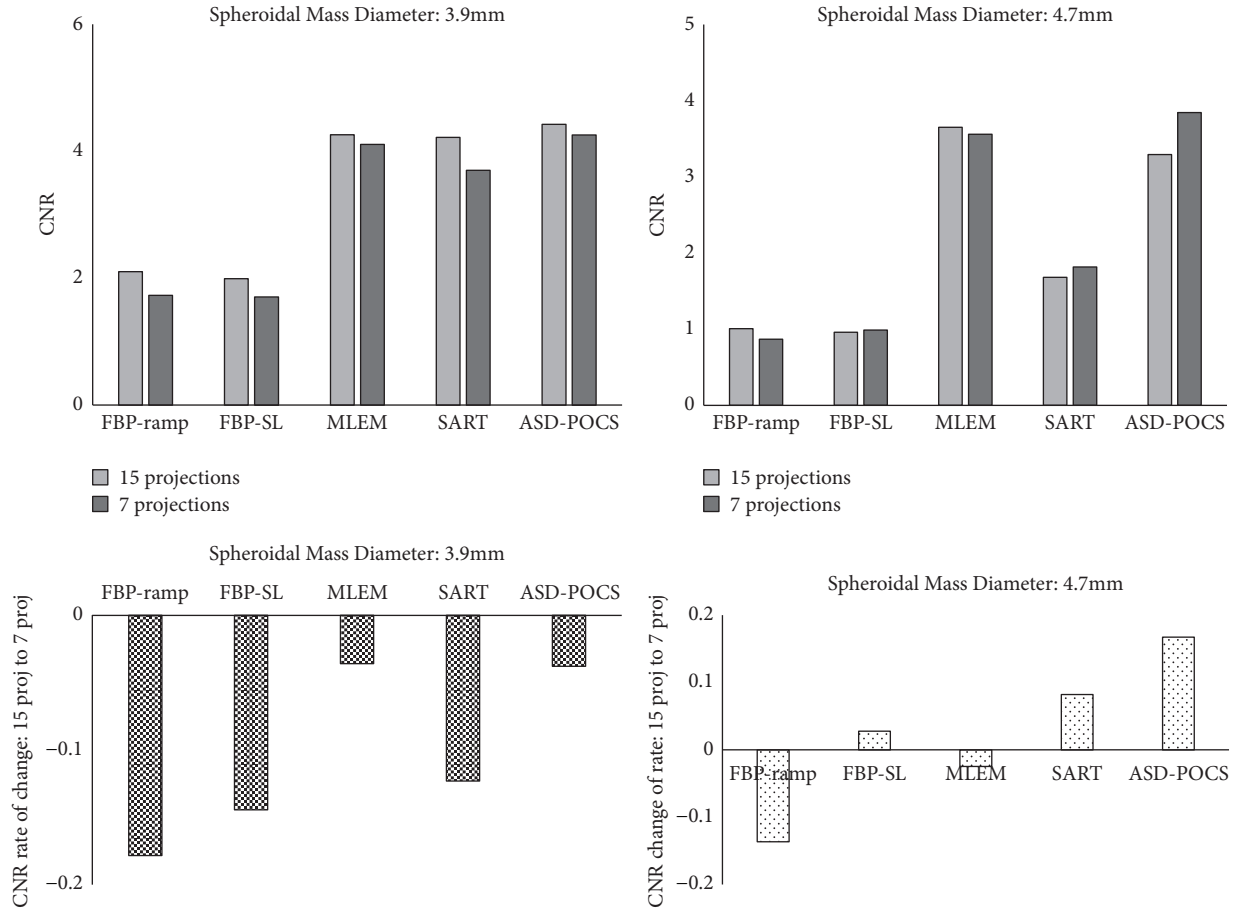


FIGURE 7: Comparisons of the contrast-to-noise ratio (CNR) and rate of change between the normal (15) and half (seven) projections in the in-focus plane images obtained via tomosynthesis under different projection numbers and generated using different tomosynthesis reconstruction algorithms.

The contrast derived from the CNR in the in-focus plane [3.9 and 4.7 mm φ ; spheroidal masses (epoxy resin)] was also evaluated as a quantitative measure of the reconstructed image quality. In tomosynthesis, the CNR is frequently used to estimate low-contrast detectability and was defined in this study as follows:

$$CNR = \frac{\mu_{Feature} - \mu_{BG}}{\sigma_{BG}} \quad (1)$$

where $\mu_{Feature}$ is the mean object pixel value, μ_{BG} is the mean background area pixel value, and σ_{BG} is the standard deviation of the background pixel values. The latter parameter includes the photon statistics and electronic noise from the results, as well as structural noise that could obscure the object. The sizes of all regions of interest (ROIs) used to measure the CNR were adjusted to an internal signal as shown in Figure 3 (3.9 mm; 21×21 pixels, 4.7 mm; 33×25 pixels).

2.6. Optimization Parameters. A range of optional parameters have been identified for ASD-POCS [TV hyperparameter (α), iteration number for TV-steepest descent (ng)]; of these, some are crucial for determining the algorithmic behavior.

In this study, we used the FWHM and CNR to verify the optimization of these parameters. To maintain a quality balance between FWHM and CNR performance, a TV hyperparameter (α) of 0.002 and iteration number for TV-steepest descent (ng) of 25 were selected (Figure 4). We compared the root-mean-square error (RMSE) and universal image quality index (QI) [reconstructed volume image (15 projections) from the previous iteration between the current iteration] to optimize the iteration numbers (i) [28]. The QI is mathematically defined by modeling the image distortion relative to the reference image as a combination of three factors: loss of correlation, luminance distortion, and contrast distortion. Because the QI does not explicitly use a human visual system model, it performs significantly better than the widely used distortion metric mean squared error for various types of image distortion. A feasibility is to keep the convergence of SART and ASD-POCS reconstruction for 5 iterations and MLEM reconstruction for 2 iterations (Figure 4).

The amplification of noise is a characteristic of non-regularized algorithms, such as MLEM. As high-frequency noise in the data is amplified by each iteration of the MLEM algorithm, few iterations may be optimum for the detection

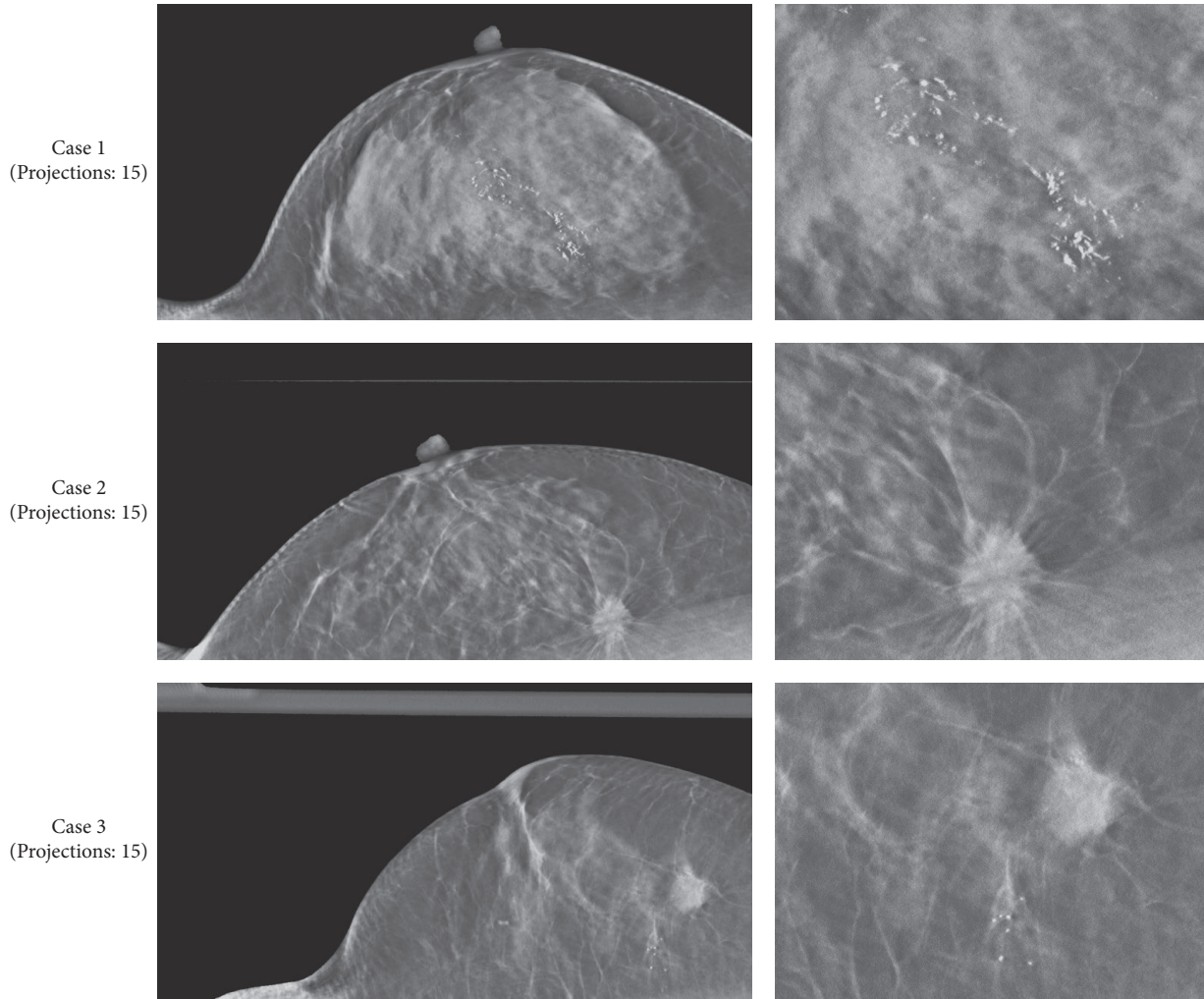


FIGURE 8: Comparisons among clinical case images (in-focus plane) obtained via actual filtered back projection reconstructions from a digital breast tomosynthesis scanner (Selenia Dimensions, 15 projections). The scanner FBP images for the corresponding image are displayed with the same window width and window level (top: case 1, middle: case 2, and bottom: case 3).

of low-contrast objects, such as small masses [3]. In the SART algorithm, the linear attenuation coefficient of each voxel is simultaneously updated using all rays in a single projection (regularized algorithm). The number of imaged volume updates in a single iteration is equal to the number of projections [23]. Considering these factors, we believe that the difference between RMSE and QI is associated with the difference between SART and MLEM algorithms.

2.7. Case Evaluation. In this study, AEC exposure was used to compare different DBT reconstruction methods in a clinical case evaluation. The cases were evaluated using structural similarity (SSIM) [29], where local patterns of luminance- and contrast-normalized pixel intensity were compared to determine the SSIM index of contrast preservation. This image quality metric is based on the assumed suitability of the human visual system for extracting structure-based information.

The SSIM index between pixel values x and y was calculated as follows:

$$SSIM(x, y) = [l(x, y)]^\alpha \cdot [c(x, y)]^\beta \cdot [s(x, y)]^\gamma \quad (2)$$

where l is the luminance, c is the contrast, and s is the structure. Subsequently,

$$\alpha = \beta = \gamma = 1.0. \quad (3)$$

The mean SSIM (MSSIM) was then used to evaluate the overall image quality:

$$MSSIM(X, Y) = \frac{1}{M} \sum_{j=1}^M SSIM(x_i, y_j) \quad (4)$$

where X and Y are the reference [reconstructed image (in-focus plane) from 15 projections] and objective [reconstructed image (in-focus plane) from seven projections] images, respectively; x_i and y_j are the image contents at the j th pixel; and M is the number of pixels in the image.

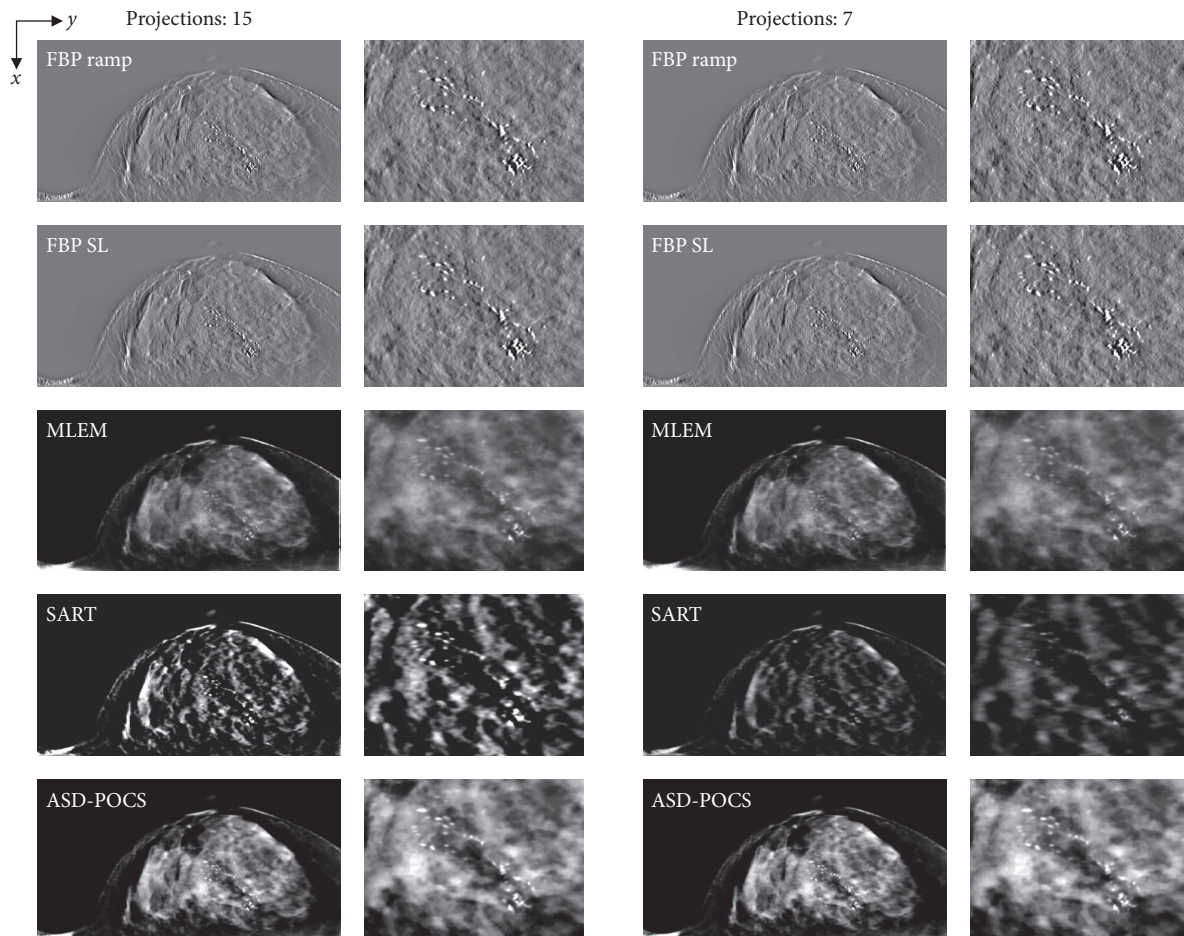


FIGURE 9: Case 1. Comparisons between images obtained at different projection numbers (normal: 15, half: seven) using each tomosynthesis reconstruction algorithm in the in-focus plane. The X-ray source was moved horizontally along the image. Zoomed images depict the lesion areas. For each corresponding set, IR (MLEM, SART, and ASD-POCS) images are displayed at the same window width and level, whereas the FBP images have a larger window widths because the backgrounds are less flattened and the gray levels in larger areas would be out of scale in narrower windows.

Details of each case are listed below.

Case 1. In a 56-year-old woman with diagnosed ductal carcinoma in situ, the following imaging parameters were used: voltage, 30 kV; tube current, 61; thickness, 46 mm; AGD, 1.75 (15 projections).

Case 2. In a 62-year-old woman with a diagnosis of scirrhous, the following parameters were used: voltage, 29 kV; tube current, 47; thickness, 39 mm; AGD, 1.32 (15 projections).

Case 3. In an 81-year-old woman with a diagnosis of solid tubular carcinoma, the following parameters were set: voltage, 29 kV; tube current, 48; thickness, 41 mm; AGD 1.29 (15 projections).

3. Results

Figure 5 presents images of the BR3D Phantom obtained using each reconstruction algorithm. Compared with the FBP algorithm, the IR algorithms tended to yield slightly higher

noise levels as the projection number decreased, although image quality deterioration was not observed. The FBP algorithm exhibited good MC detection ability but also generated remarkable false images from the peripheries of the MCs.

We also compared the FWHM of each reconstructed image obtained using different projection numbers for the in-focus plane (Figure 6). Here, the FBP algorithm yielded the best spatial resolution, whereas this parameter tended to deteriorate while using the ASD-POCS algorithm to reconstruct a reduced number of projections. Furthermore, the number of projections but not the MC size affected the FWHM rate of change.

We further compared the CNR of each reconstructed image obtained using different projection numbers for the in-focus plane (Figure 7). Notably, the ASD-POCS algorithm yielded high-contrast images, regardless of the simulated mass lesion size and projection number. With the FBP algorithm, the contrast degradation increased at reduced projection numbers when generating images of 3.9-mm spheroidal masses. With the MLEM and ASD-POCS algorithms,

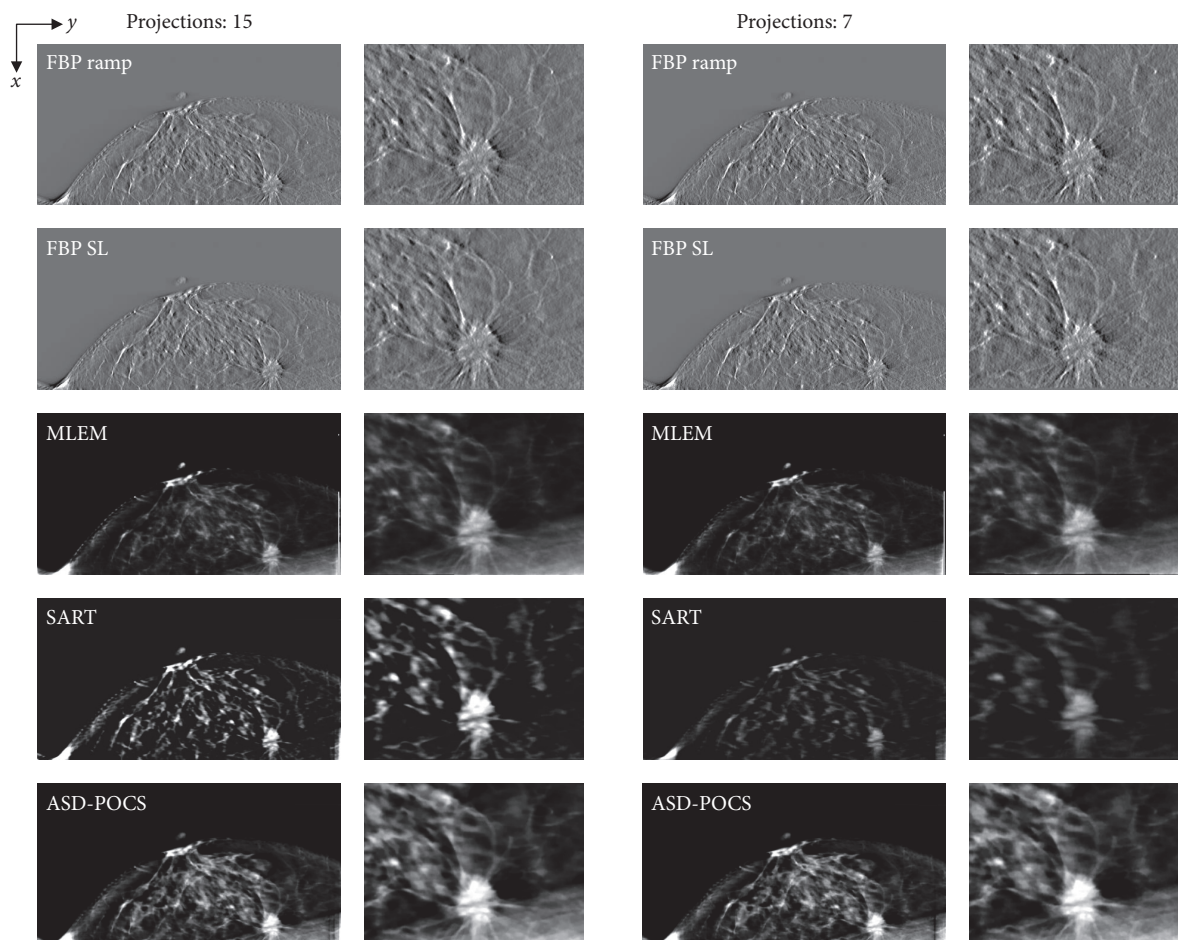


FIGURE 10: Case 2. Comparisons between images obtained at different projection numbers (normal: 15, half: seven) using each tomosynthesis reconstruction algorithm in the in-focus plane. The X-ray source was moved horizontally along the image. Zoomed images depict the lesion areas. For each corresponding set, IR (MLEM, SART, and ASD-POCS) images are displayed at the same window width and level, whereas the FBP images have a larger window widths because the backgrounds are less flattened and the gray levels in larger areas would be out of scale in narrower windows.

contrast deterioration associated with a decreased projection number had only a small effect. For 4.7-mm spheroidal masses, the CNR tended to increase as the projection number decreased when using the FBP(SL), SART, and ASD-POCS algorithms and tended to decrease when using the FBP (ramp) and MLEM algorithms.

Reconstructed images of three clinical cases, which were obtained using actual FBP reconstructed images (in-focus plane) from the scanner (Selenia Dimensions), are presented as reference data in Figure 8. Reconstructed clinical case images obtained using each reconstruction algorithm are presented in Figures 9–11, while Figure 12 compares the SSIM images obtained with each reconstruction algorithm using either 15 or seven projections for the in-focus plane. Figure 13 compares the MSSIM of each reconstructed clinical case image obtained in the in-focus plane. Images reconstructed using the ASD-POCS and MLEM algorithms and a reduced number of projections were highly structurally similar, suggesting that the former could potentially be used in dose reduction initiatives while preserving contrast.

4. Discussion

Our empirical results obtained using various reconstruction algorithms demonstrate that the ASD-POCS algorithm can preserve image contrast even when using reduced projection data. Accordingly, the ASD-POCS algorithm could potentially be used to reduce radiation doses to patients.

The outermost repeat-until loop instruction of the ASD-POCS algorithm contains two main components: an adjustment toward data consistency via the POCS step loop and the steepest descent toward lower-TV images. The algorithm is effective when each POCS step involves multiple small descent substeps, particularly during the early iterations [20]. TV-minimization assumes that the true image is piecewise and relatively uniform, whereas noise and artifacts appear as fluctuations, or peaks and valleys; accordingly, noise and artifact-corrupted images would have relatively larger TV values because TV is defined as the sum of first-order derivative magnitudes [22]. In contrast, compared with the SART algorithm MSSIM results similar to the ASD-POCS

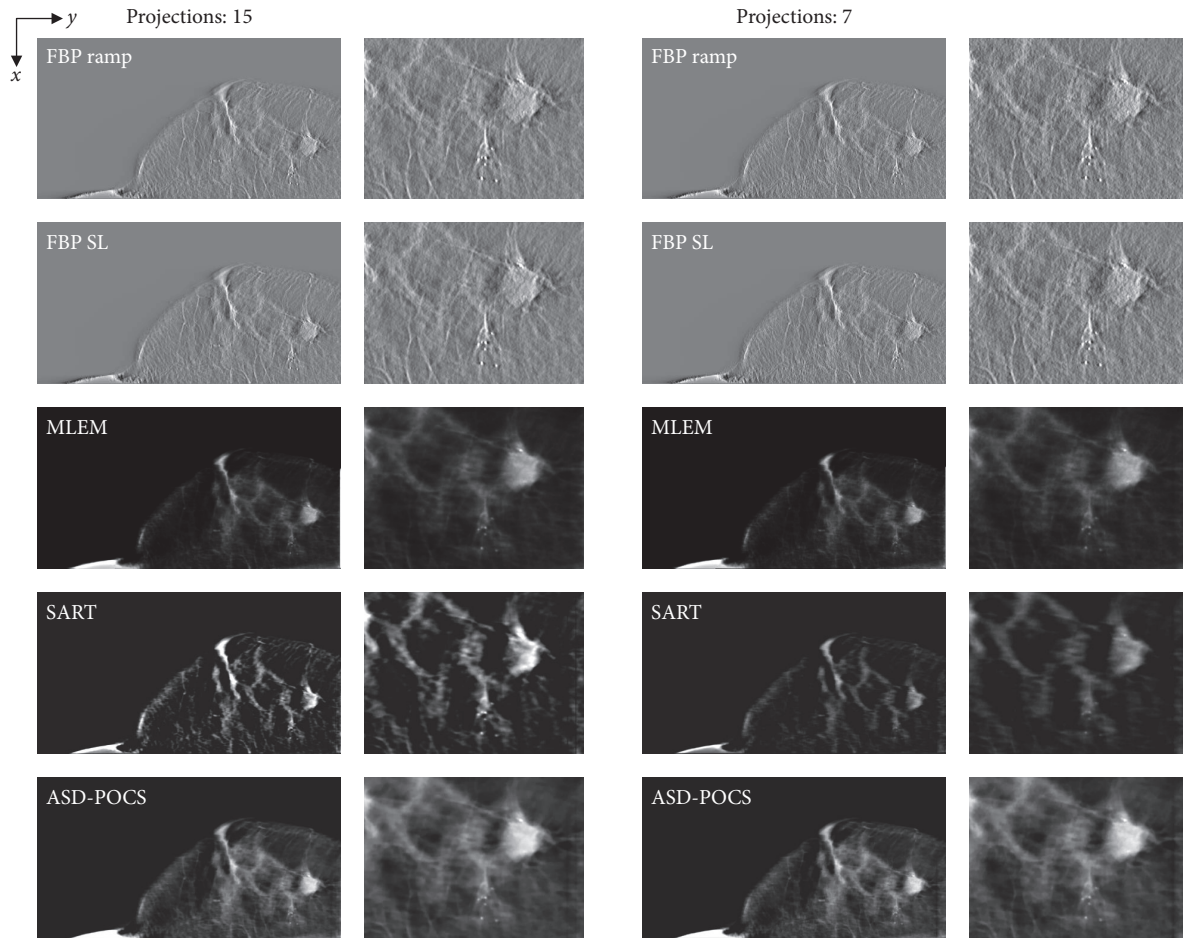


FIGURE 11: Case 3. Comparisons between images obtained at different projection numbers (normal: 15, half: seven) using each tomosynthesis reconstruction algorithm in the in-focus plane. The X-ray source was moved horizontally along the image. Zoomed images depict the lesion areas. For each corresponding set, IR (MLEM, SART, and ASD-POCS) images are displayed at the same window width and level, whereas the FBP images have a larger window widths because the backgrounds are less flattened and the gray levels in larger areas would be out of scale in narrower windows.

algorithm have shown preserved contrast, but a large change rate from the FWHM and low-contrast detection compared with the ASD-POCS algorithm. We suggest that these results are attributable to the inability of the SART algorithm to correct increases in noise. Moreover, incorrect assumptions in the reconstruction models lead to the active introduction of artifacts, whereas TV suppresses the high-frequency components of artifacts introduced by data consistency.

In general, image artifacts are caused by a loss of the largest normal contributions from artifact-free voxels. As these voxels normally produce original contributions, their values decrease slightly after the largest normal contribution has been omitted. Accordingly, a single abnormal contribution within a voxel is resolved while all other contributions are retained, including the largest normal contribution; voxels containing such abnormalities therefore tend to exhibit higher values than their neighboring artifact-free voxels, leading to the appearance of objects in which artifact-free voxels are more noticeable against the background. This

phenomenon is a drawback of the FBP algorithm, and consequent artifacts are conspicuous when compared with artifact-free images.

DT image quality depends on several factors, including size, shape, density, atomic number, and the size and shape of the object cross-section. Highly attenuating objects yield streak artifacts (dark-band artifacts) on DBT acquisitions, which adversely affect image quality. Additionally, beam hardening and scattering have significant effects, particularly on highly attenuating objects from MCs. Accordingly, noise-induced streak artifacts primarily affect image quality. In such cases, the IR reconstruction algorithm, which is thought to adequately address quantum noise [30], appears to be a promising approach to the reduction of artifacts stemming from MCs with relatively high atomic numbers.

SART does not imply an even distribution of noise across an image. Rather, SART uses an algebraic matrix to selectively identify and subtract noise from an image according to a mathematical model. However, each iteration

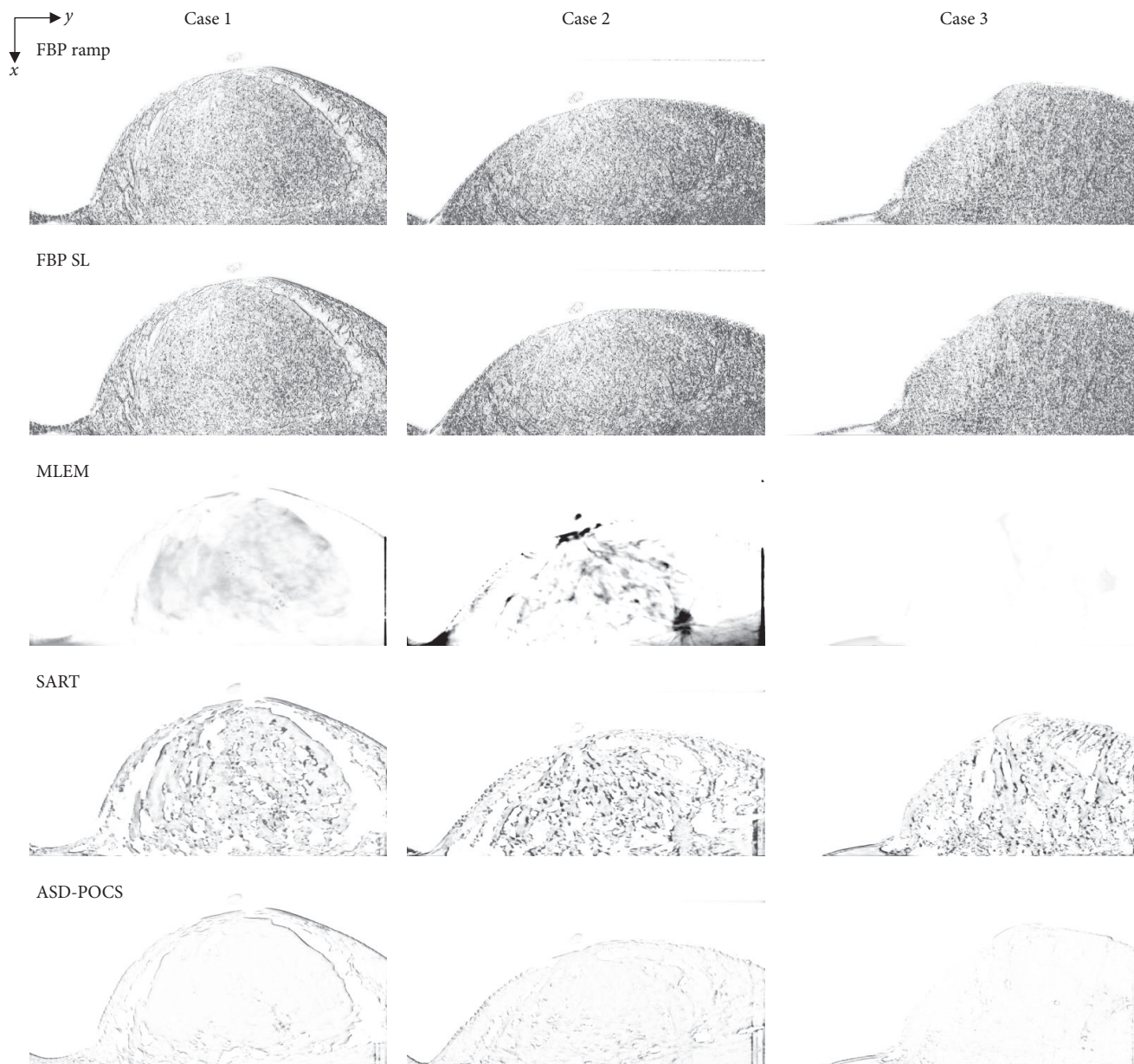


FIGURE 12: Comparisons of structural similarity among images obtained from each case and using each tomosynthesis reconstruction algorithm in the in-focus plane. The X-ray source was moved horizontally along the image. Images are in grayscale; white and black indicate high and low structural similarity, respectively. The window width and level in each display are varied to allow a visual comparison of the contrast and background gray level. Corresponding IR (MLEM, SART, and ASD-POCS) images are displayed at the same window width and level.

of the reconstruction algorithm amplifies high-frequency noise within the data. Therefore, the MLEM algorithm may be optimal for detecting low-contrast objects [3].

We further found that images generated using the ASD-POCS algorithm with a reduced projection number exhibited deteriorated spatial resolution. TV-based approaches uniformly penalize the image gradient, regardless of the image structure. Therefore, oversmoothing of the reconstructed image remains a major concern, despite the advantages of using a TV norm as the regularization term

[31]. Frequent oversmoothing of the edges of the reconstructed image causes the loss of low-contrast information [32].

Most studies have evaluated breast imaging at different radiation doses [33]. We believe that investigations of the relationship between normal and half projections and contrast preservation are useful for determining the feasibility of radiation dose reduction and hope that our study results serve as a guideline for image reconstruction under reduced projection data conditions. However, our study had several

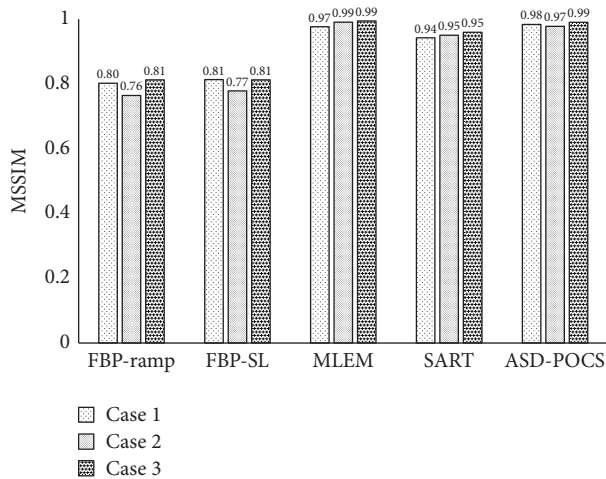


FIGURE 13: Comparisons of mean structural similarity among in-focus plane images obtained via tomosynthesis data from clinical cases under normal (15) and half projections (seven) and using each tomosynthesis reconstruction algorithm.

limitations. First, we did not test actual mammary gland tissues. However, we believe that the BR3D Phantom is an accurate representation of actual mammary gland tissues. Second, we did not perform an observational study. In future, we plan to conduct such a study to investigate the correlations among physical evaluation parameters (e.g., spatial resolution and contrast). Third, the phantom thickness was fixed at 4 cm. In future evaluations, other phantom thicknesses will be needed to confirm the utility of the algorithm. Despite these limitations, we believe that our results can serve as reference data and thus assist physicians with contrast preservation while reducing radiation exposure.

5. Conclusion

This study evaluated the ASD-POCS algorithm as a novel technique for contrast preservation in DBT images obtained under a reduced projection number. Our findings suggest that the ASD-POCS algorithm could be used to reconstruct dose-reduced images. As this approach exploits *a priori* knowledge about contrast preservation and noise reduction, we presume that the ASD-POCS algorithm will enhance the clinical application of DBT in medical imaging, wherein these parameters are a major focus of interest.

Data Availability

No data were used to support this study.

Conflicts of Interest

The authors declare that they have no conflicts of interest.

Ethical Approval

Our institutional review board approved this study (clinical evaluation) (National Hospital Organization Takasaki General Medical Center, No. H28-43, approved: July 2016)

Consent

Written informed consent was obtained from all patients.




References

- [1] H. Machida, T. Yuhara, T. Mori, E. Ueno, Y. Moribe, and J. M. Sabol, "Optimizing parameters for flat-panel detector digital tomosynthesis," *RadioGraphics*, vol. 30, no. 2, pp. 549–562, 2010.
- [2] P. Skaane, A. I. Bandos, R. Gullien et al., "Comparison of digital mammography alone and digital mammography plus tomosynthesis in a population-based screening program," *Radiology*, vol. 267, no. 1, pp. 47–56, 2013.
- [3] T. Wu, A. Stewart, M. Stanton et al., "Tomographic mammography using a limited number of low-dose cone-beam projection images," *Medical Physics*, vol. 30, no. 3, pp. 365–380, 2003.
- [4] M. A. Helvie, M. A. Roubidoux, Y. Zhang, P. L. Carson, and H. P. Chan, *Tomosynthesis Mammography Vs Conventional Mammography: Lesion Detection and Reader Reference*, vol. 355, 2006.
- [5] I. Sechopoulos, K. Bliznakova, and B. Fei, "Power spectrum analysis of the x-ray scatter signal in mammography and breast tomosynthesis projections," *Medical Physics*, vol. 40, no. 10, Article ID 101905, pp. 1–7, 2013.
- [6] D. Gur, M. L. Zuley, M. I. Anello et al., "Dose reduction in digital breast tomosynthesis (DBT) screening using synthetically reconstructed projection images. An observer performance study," *Academic Radiology*, vol. 19, no. 2, pp. 166–171, 2012.
- [7] J. T. Dobbins III and D. J. Godfrey, "Digital x-ray tomosynthesis: Current state of the art and clinical potential," *Physics in Medicine and Biology*, vol. 48, no. 19, pp. R65–R106, 2003.
- [8] R. Gordon, R. Bender, and G. T. Herman, "Algebraic reconstruction techniques (ART) for three-dimensional electron microscopy and X-ray photography," *Journal of Theoretical Biology*, vol. 29, no. 3, pp. 471–481, 1970.
- [9] P. Bleuet, R. Guillemaud, I. Magnin, and L. Desbat, "An adapted fan volume sampling scheme for 3D algebraic reconstruction in linear tomosynthesis," *IEEE Xplore: IEEE Transactions on Nuclear Science*, vol. 3, pp. 1720–1724, 2001.
- [10] T. Wu, J. Zhang, R. Moore et al., "Digital tomosynthesis mammography using a parallel maximum likelihood reconstruction method," *SPIE*, vol. 5368, pp. 1–11, 2004.
- [11] Y. Lu, H.-P. Chan, J. Wei, L. M. Hadjiiski, and R. K. Samala, "Multiscale bilateral filtering for improving image quality in digital breast tomosynthesis," *Medical Physics*, vol. 42, no. 1, Article ID 4903283, pp. 182–195, 2015.
- [12] S. Xu, J. Lu, O. Zhou, and Y. Chen, "Statistical iterative reconstruction to improve image quality for digital breast tomosynthesis," *Medical Physics*, vol. 42, no. 9, pp. 5377–5390, 2015.
- [13] A. Maldera, P. De Marco, P. E. Colombo, D. Origgi, and A. Torresin, "Digital breast tomosynthesis: Dose and image quality assessment," *Physica Medica*, vol. 33, pp. 56–67, 2017.
- [14] P. Ferreira, M. Baptista, S. Di Maria, and P. Vaz, "Cancer risk estimation in Digital Breast Tomosynthesis using GEANT4

- Monte Carlo simulations and voxel phantoms,” *Physica Medica*, vol. 32, no. 5, pp. 717–723, 2016.
- [15] S. Di Maria, M. Baptista, M. Felix et al., “Optimal photon energy comparison between digital breast tomosynthesis and mammography: A case study,” *Physica Medica*, vol. 30, no. 4, pp. 482–488, 2014.
- [16] E. Y. Sidky, I. S. Reiser, R. Nishikawa, and X. Pan, “Image reconstruction in digital breast tomosynthesis by total variation minimization,” in *Proceedings of the Medical Imaging 2007: Physics of Medical Imaging*, vol. 6510, pp. U1110–U1115, February 2007.
- [17] E. Y. Sidky, X. Pan, I. S. Reiser, R. M. Nishikawa, R. H. Moore, and D. B. Kopans, “Enhanced imaging of microcalcifications in digital breast tomosynthesis through improved image-reconstruction algorithms,” *Medical Physics*, vol. 36, no. 11, pp. 4920–4932, 2009.
- [18] Y. Lu, H.-P. Chan, J. Wei, and L. M. Hadjiiski, “Selective-diffusion regularization for enhancement of microcalcifications in digital breast tomosynthesis reconstruction,” *Medical Physics*, vol. 37, no. 11, pp. 6003–6014, 2010.
- [19] M. Das, H. C. Gifford, J. M. O’Connor, and S. J. Glick, “Penalized maximum likelihood reconstruction for improved microcalcification detection in breast tomosynthesis,” *IEEE Transactions on Medical Imaging*, vol. 30, no. 4, pp. 904–914, 2011.
- [20] E. J. Candes, J. Romberg, and T. Tao, “Robust uncertainty principles: exact signal reconstruction from highly incomplete frequency information,” *Institute of Electrical and Electronics Engineers Transactions on Information Theory*, vol. 52, no. 2, pp. 489–509, 2006.
- [21] E. J. Candes, J. K. Romberg, and T. Tao, “Stable signal recovery from incomplete and inaccurate measurements,” *Communications on Pure and Applied Mathematics*, vol. 59, no. 8, pp. 1207–1223, 2006.
- [22] E. Y. Sidky and X. Pan, “Image reconstruction in circular cone-beam computed tomography by constrained, total-variation minimization,” *Physics in Medicine and Biology*, vol. 53, no. 17, pp. 4777–4807, 2008.
- [23] M. Aharon, M. Elad, and A. Bruckstein, “K-SVD: An algorithm for designing overcomplete dictionaries for sparse representation,” *IEEE Transactions on Signal Processing*, vol. 54, no. 11, pp. 4311–4322, 2006.
- [24] Y. Du, X. Wang, X. Xiang, and Z. Wei, “Evaluation of hybrid SART + OS + TV iterative reconstruction algorithm for optical-CT gel dosimeter imaging,” *Physics in Medicine and Biology*, vol. 61, no. 24, pp. 8425–8439, 2016.
- [25] G.-H. Chen, J. Tang, and S. Leng, “Prior image constrained compressed sensing (PICCS): a method to accurately reconstruct dynamic CT images from highly undersampled projection data sets,” *Medical Physics*, vol. 35, no. 2, pp. 660–663, 2008.
- [26] D. R. Dance, K. C. Young, and R. E. Van Engen, “Estimation of mean glandular dose for breast tomosynthesis: Factors for use with the UK, European and IAEA breast dosimetry protocols,” *Physics in Medicine and Biology*, vol. 56, no. 2, pp. 453–471, 2011.
- [27] Mathworks, Inc., <http://www.mathworks.com/products/matlab/>, 2014.
- [28] Z. Wang and A. C. Bovik, “A universal image quality index,” *IEEE Signal Processing Letters*, vol. 9, no. 3, pp. 81–84, 2002.
- [29] Z. Wang, A. C. Bovik, H. R. Sheikh, and E. P. Simoncelli, “Image quality assessment: from error visibility to structural similarity,” *IEEE Transactions on Image Processing*, vol. 13, no. 4, pp. 600–612, 2004.
- [30] T. Wu, R. H. Moore, E. A. Rafferty, and D. B. Kopans, “A comparison of reconstruction algorithms for breast tomosynthesis,” *Medical Physics*, vol. 31, no. 9, pp. 2636–2647, 2004.
- [31] Y. Liu, J. Ma, Y. Fan, and Z. Liang, “Adaptive-weighted total variation minimization for sparse data toward low-dose x-ray computed tomography image reconstruction,” *Physics in Medicine and Biology*, vol. 57, no. 23, pp. 7923–7956, 2012.
- [32] Z. Tian, X. Jia, K. Yuan, T. Pan, and S. B. Jiang, “Low-dose CT reconstruction via edge-preserving total variation regularization,” *Physics in Medicine and Biology*, vol. 56, no. 18, pp. 5949–5967, 2011.
- [33] T. Gomi, “Comparison of different reconstruction algorithms for decreasing the exposure dose during digital breast tomosynthesis: a phantom study,” *Journal of Biomedical Science and Engineering*, vol. 08, pp. 471–478, 2015.

Research Article

The Evolving Role of Ultrasound Guided Percutaneous Laser Ablation in Elderly Unresectable Breast Cancer Patients: A Feasibility Pilot Study

Jacopo Nori,¹ Maninderpal Kaur Gill ,² Icro Meattini,³ Camilla Delli Paoli,³ Dalmar Abdulcadir,¹ Ermanno Vanzi,¹ Cecilia Boeri,¹ Silvia Gabbrielli,¹ Elisabetta Giannotti,¹ Francesco Lucci,¹ Vania Vezzosi,⁴ Diego De Benedetto,¹ Giulia Bicchierai ,¹ Simonetta Bianchi,⁴ Luis Sanchez,⁵ Lorenzo Orzalesi,⁵ Guido Carmelo,⁶ Vittorio Miele ,¹ Lorenzo Livi,³ and Donato Casella⁴

¹Diagnostic Unit, Azienda Ospedaliero-Universitaria Careggi, Florence, Italy

²Department of Biomedical Imaging, Kuala Lumpur General Hospital, Kuala Lumpur, Malaysia

³Radiation Oncology Unit, Azienda Ospedaliero-Universitaria Careggi, University of Florence, Florence, Italy

⁴Division of Pathological Anatomy, University of Florence, Florence, Italy

⁵Breast Surgery Unit, Azienda Ospedaliero-Universitaria Careggi, University of Florence, Florence, Italy

⁶Anesthesia Unit, Azienda Ospedaliero-Universitaria Careggi, Florence, Italy

Correspondence should be addressed to Giulia Bicchierai; giulia.bicchierai@gmail.com

Received 22 October 2017; Accepted 14 March 2018; Published 11 June 2018

Academic Editor: Gianluca Gatta

Copyright © 2018 Jacopo Nori et al. This is an open access article distributed under the Creative Commons Attribution License, which permits unrestricted use, distribution, and reproduction in any medium, provided the original work is properly cited.

Background and Objectives. Breast-conserving surgery represents the standard of care for the treatment of small breast cancers. However, there is a population of patients who cannot undergo the standard surgical procedures due to several reasons such as age, performance status, or comorbidity. Our aim was to investigate the feasibility and safety of percutaneous US-guided laser ablation for unresectable unifocal breast cancer (BC). **Methods.** Between December 2012 and March 2017, 12 consecutive patients underwent percutaneous US-guided laser ablation as radical treatment of primary inoperable unifocal BC. **Results.** At median follow-up of 28.5 months (range 6-51), no residual disease or progression occurred; the overall success rate for complete tumor ablation was therefore 100%. No significant operative side effects were observed, with only 2 (13.3%) experiencing slight to mild pain during the procedure, and all patients complained of a mild dull aching pain in the first week after procedure. **Conclusions.** Laser ablation promises to be a safe and feasible approach in those patients who are not eligible to the standard surgical approach. However, longer follow-up results and larger studies are strongly needed.

1. Introduction

Breast cancer (BC) is the most frequently occurring cancer in women (28.8% of all cancer diagnosis) and the second most common in the world, with an estimated lifetime risk of 1/10 women [1].

Despite the steady increase of the number of BC newly diagnosed worldwide, its mortality has shown a slight decrease in western countries. This might be due to widespread screening programs, resulting in an increased

diagnosis of small tumors, and it might be secondary to better therapeutic strategies [2, 3]. Over 40% of women with newly diagnosed BC are aged 65 years or older, and the median age at diagnosis is around 60 years [4].

Although breast-conserving surgery (BCS) represents the treatment of choice for small BC [5], elderly women often receive less than this standard therapy. In a large study, which involved over 120,000 women, decreased surgical rates were associated with higher age due to several reasons such as performance status or comorbidity [4, 6, 7].

Therefore, in the last decade, in parallel to the increasing age of patients with a diagnosis of breast cancer, there has been a progressive demand for minimally invasive treatments specifically aimed at BC [8–10]. These treatments are not substitutes for breast surgery, which is still the primary treatment of choice, but they could represent a radical treatment for the nonoperable group of patients or for those who refuse surgery. The approaches available include cryoablation [11–15], radiofrequency [16, 17], microwave ablation [18], focused ultrasound (US) [19, 20], and laser ablation [21, 22].

The purpose of our single-center retrospective study is to assess the feasibility of ultrasound guided percutaneous laser ablation (LA), as the treatment of small unifocal breast cancer in nonoperable elderly patients and in patients who refuse surgery.

2. Methods

We achieved the Internal Review Board (IRB) approval for this trial, performed in a large university referral hospital for breast disease. Written informed consent of patients was required for the inclusion in this study. All procedures were in accordance with the ethical standards of the institutional and/or national research committee and with the 1964 Helsinki Declaration and its later amendments or comparable ethical standards.

The primary objectives of our study are to (i) describe the results of laser ablation in nonoperable patients with unifocal BC and (ii) assess the effectiveness and safety of LA to treat BC.

The secondary objectives would be to (i) evaluate the breast cosmesis, (ii) determine regional and distant breast tumor recurrence rate up to 5 years, and (iii) determine the overall survival rate among the period of the study.

2.1. Patient Selection and Period of Study. We retrospectively reviewed 12 breast cancer patients who underwent percutaneous procedures in our Department of Breast Diagnostic Senology Unit of the Careggi Hospital, Italy, between December 2012 and March 2017. The multidisciplinary team of our department carefully selected elderly patients (>75 years), with inoperable breast cancer, due to comorbidities and/or to high anesthetic risks, or who refuse surgery.

The inclusion criteria were as follows:

- (1) unresectable unifocal BC due to comorbidity (e.g., severe cardiovascular or respiratory comorbidities, age, performance status),
- (2) tumor size ≤ 20 mm in the greatest diameter,
- (3) the necessity of lesion being US visible at the time of treatment,
- (4) tumor located at least 1.0 cm from the chest wall as well as the skin and nipple at USG,
- (5) a biopsy proving invasive ductal unifocal, mucinous, or tubular carcinoma.

The exclusion criteria were as follows:

- (1) patients suitable for surgery or radiation approach,

- (2) patients with multifocal or multicentric tumors,
- (3) absence of written informed consent.

2.2. Procedure Planning. All patients underwent clinical and radiological assessments prior to the laser ablation. Clinical assessment included physical breast examination to exclude skin or nipple involvement.

2.3. Breast Mammogram and Ultrasound. Radiological assessment included a bilateral two-projection 2D-3D mammography (MMG) (Selenia® Dimensions®, Hologic®, Bedford, USA) and ultrasonographic (US) examinations were performed using a 10–13 MHz transducer and a US unit (ESAOTE, MyLab 70 XVG, Genoa, Italy).

2.4. Ultrasound Guided Biopsy. All lesions were sampled with US-guided core-needle biopsy (CNB) using a 10 cm 14-gauge cutting needle with a 22 mm throw (Precisa™, HS® Hospital Service, Rome, Italy). A mean of 4 samples (range 3-5 samples) was taken in each case to evaluate the histological and biological parameters of the tumor. Specimens underwent a standard histological evaluation.

2.5. Laser Ablation Procedure. The procedure needed an ultrasound interventional suite. Procedures were performed by using a commercially available US system with an integrated laser source with a 1064 nm wavelength (EchoLaser; Elesta, Calenzano, Italy).

In each case, procedure needed the presence of an anesthesiologist in the ultrasound interventional room and available venous access. Generally, patients underwent local anesthesia; we used conscious sedation only if indicated.

The operator inserts the 21G spinal needle in the most suitable direction to reach the lesion following the shortest possible path. Then the operator introduces and advances a 300 μ m flat-tip laser fiber to the tip of the needle. The introducer-needle was designed to expose the fiber tip of 5 mm. The procedure must provide a safe distance of 1.0 cm from the skin and 1.0 cm from the chest wall. The operator must progressively move the device LA (introducer-needle and fiber) towards the target, choosing the best path to correctly position the tip of the fiber. It is necessary to make sure that the path of the applicator is as parallel as possible to the chest wall. The tip of the device must always be in the center of the lesion and its position must always be controlled with two-plane ultrasound images (Figure 1).

According to previous experiences of other authors in other applications of the thin needle laser methodology, each treatment was performed with a fixed power protocol (3W), modifying the lighting time according to the size of the tumor. Depending on the size of the tumor at baseline, the operator performs one or two consecutive illuminations with a “pull-back” technique during the same treatment session. The treatment ends when the gas, formed during the ablation, covers the entire desired area or up to 1800 J for illumination. Each ablation time varies from a minimum of 600 seconds (for tumor size up to 1.0 cm) to a maximum of 1200 seconds (for tumor size between 1.0 and 2.0 cm), in order to maintain the total energy applied between 1800 and

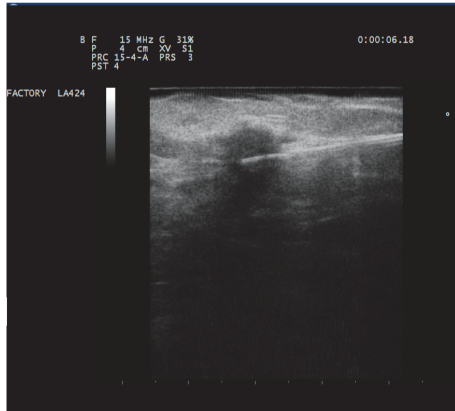


FIGURE 1: The device LA (introducer-needle and fiber) must be progressively inserted towards the target, choosing the best path to correctly position the tip of the fiber. It is necessary to ensure that the path of the applicator is as parallel as possible to the chest wall. The tip of the device should always be inserted at the center of the lesion and its position must always be controlled with two-plane ultrasound images.

3600 J], respectively [23–26]. Patient vital signs monitoring was continuous during all of the procedure.

In all cases, the laser fiber was active during the retraction of the needle, in order to prevent a possible seeding of tumor cells along the needle tract. Patient monitoring continued up to 2–4 hours, in order to exclude unexpected acute complications, and patient discharge occurred subsequently, during the same day.

2.6. Follow-Up of Patients. Clinical follow-up began after 1 week, then at 3 months, and every 6 months until the fifth year. Clinical examination assessed the skin and nipple conditions and it evaluated the clinical size of the treated lesion, if palpable. Radiological follow-up included a weekly US examination from the 1st and 4th week after the ablation procedure. Follow-up also included bilateral mammography and ultrasound after 6 months from the laser procedure and every 12 months thereafter up to 5 years.

The radiologist who performed the LA procedure was the same that performed the ultrasound and mammographic image evaluation. We have observed modifications of treated site after the procedure, and we have considered as suggestive of ablation/recurrence the radiologic aspects observed. Complete ablation corresponded to a well-demarcated area of coagulation zone at the previously ablated site on ultrasound. Definition of recurrences were as follows:

(1) *Local*

- (i) The previously ablated area had an ill-defined margin, and a soft tissue echogenicity within 10 mm of the ablated margin was seen.
- (ii) The previously ablated region increased in size.

(2) *Distant*

- (i) New lesion was at >10 mm from the ablated margin.

TABLE 1: Data of patients and diagnostic findings prior to treatment.

Characteristic	Value
Median age (range)	79.25 (75-92)
Postmenopausal, % (n)	100 (12/12)
Right breast, % (n)	41.7%, 5/12
Left breast, % (n)	58.3%, 7/12
Median ultrasound tumor size (mm) (range)	12.72 (range 0.7-20)
Histology, % (n)	
(i) Ductal carcinoma	83.3% (10/12)
(ii) Mucinous carcinoma	8.3% (1/12)
(iii) Tubular carcinoma	8.3% (1/12)

2.7. Complications. Major complications were related to admission to the hospital for therapy, an unplanned increase in the level of care, prolonged hospitalization (more than 3 days), permanent adverse sequelae, or death. Any other complication was considered minor.

We have recorded complications of treatment according to the Society of Interventional Radiology (SIR) guidelines [27, 28].

2.8. Survival. Overall survival was defined as the time from the initial laser ablation session until death or the last patient contact. The follow-up for this study ended in March 2017.

3. Results

3.1. Demographic Analysis of Study Population. Data of 12 patients with invasive breast cancers are summarized in Table 1. Their mean age was 79.2 years (range 75-92). All patients were postmenopausal.

They have completed preliminary diagnostic phase in a mean of 11 days before the laser treatment (range 1-60), and they underwent laser ablation in the US-dedicated room, through local and conscious anesthesia. Mean US-based ablated lesion size was 12.72 mm (range 0.7-20).

Five (41.7%, 5/12) tumors were located in the right breast while seven (58.3%, 7/12) tumors were in the left breast. The pathological diagnoses of the carcinomas were 10 ductal infiltrating (83.3%, 10/12), 1 mucinous (8.3%, 1/12), and 1 tubular (8.3%, 1/12). Table 2 reported the clinical and US assessment prior to ablation.

3.2. Laser Ablation Analysis. The fibers were placed into the center of the lesion of each tumor, and LA was completed according to a planned protocol in all sessions with a technical success rate of 100 %. The overall treatment time ranged from 20 to 35 minutes.

Response to the treatment was evaluated using US after 1 to 4 weeks, with US and mammogram at 6 months, and then annually up to 5 years.

At the site of ablation, all lesions showed a well-demarcated cystic lesion, visible at the 6-month US and compatible with coagulative necrosis. The overall success rate for complete tumor ablation (CTA) was 100% (Figures 2-3).

TABLE 2: Patients characteristics.

Patient Number	Reason for non-operability	Age (Years)	USG tumor size (Pre-biopsy) (mm)
01	Hypertension (HTN) and diabetes mellitus (DM)	80	15 mm
02	Congestive heart failure with DM	88	15 mm
03	CVS co-morbidity and HTN	83	10 mm
04	Ischemic heart disease	84	15 mm
05	DM with end stage renal disease	87	12 mm
06	Cardiomyopathy	86	10 mm
07	Patient refused operation	90	7 mm
08	CVS co-morbidity and pacemaker	85	15 mm
09	Patient refused operation	75	11 mm
10	Age factor with diabetes and hypertension	92	12 mm
11	Parkinson's	90	20 mm
12	Congestive heart failure	88	15 mm

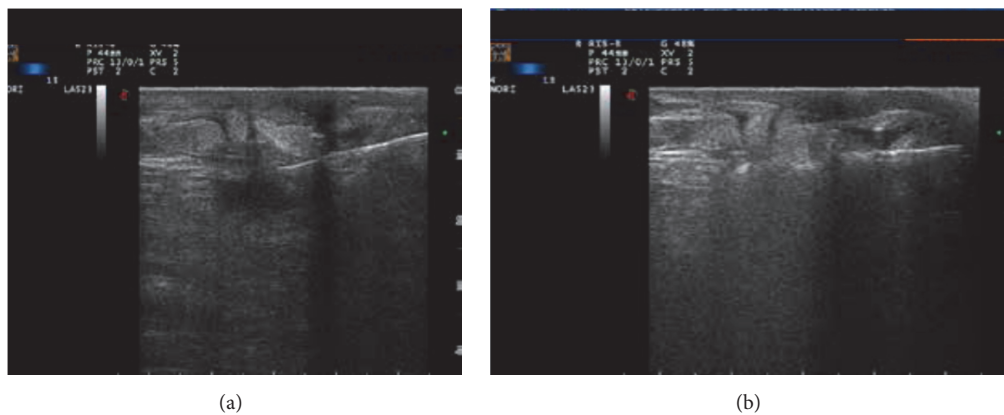


FIGURE 2: Representative case of successful LA ablation in a patient with invasive ductal unifocal breast carcinoma of 18 mm of max diameter in the upper outer quadrant of the right breast. (a) The US image before treatment shows the hypoechoic lesion with ill-defined margins and the fine needle and the tip of the fiber in the outer third of the tumor mass. (b) The US image at the end of the treatment shows an evident shadow cone due to the presence of gas bubbles that completely cover the ablated area.

At mammography, the necrotic lesion appeared as a typical area of steatonecrosis (Figure 4).

Follow-up lasted a mean time of 28.5 months (range 6-51). None of the patients demonstrated evidence of local or distant recurrence during follow-up. No breast cancer related deaths occurred in any of the patients.

3.3. Complications. During the procedure, 2 (16.6%, 2/12) patients complained of mild pain and required conscious sedation. The remaining patients well tolerated the procedure with local anesthesia. However, all the patients experienced a minimal aching sensation at the ablation site during the first week after the procedure (SIR class A) [27, 28]. There were no complications of skin burns in the posttreatment clinical follow-up. The overall treatment time ranged from 20 to 35 minutes. Patients did not need hospitalization; they underwent procedure and they discharged the same day.

None of the patients sustained any systemic adverse effects and there was no evidence of postablation hematoma, infection, or skin burns.

4. Discussion

The main advantages of minimally percutaneous therapies included the non-invasiveness, the good cosmesis, the lower painfulness, the short recovery time, and the possibility of a daycare procedure. These factors reduce the cost of hospital stay and they potentially lower risks of morbidity and mortality, in this group of elderly patients.

Our study showed that percutaneous laser ablation is a feasible and effective option for selected unresectable BC patients. We managed to obtain complete ablation in patients with small lesions (T1 lesions ≤ 20 mm). We excluded invasive lobular carcinoma and ductal carcinoma in situ, due to the unfavorable results with other minimally invasive techniques, as shown by previous reports [22].

In line with the above-mentioned studies, we chose US to guide the treatment, since it was effective in showing the real-time correct positioning of the needle at the center of the lesion and the change in echogenicity during treatment. In all cases, the increased echogenicity had an effect of partial hiding of the treatment area (fog-effect). This is due to high temperatures close to the fiber tip when it reaches over 100°C

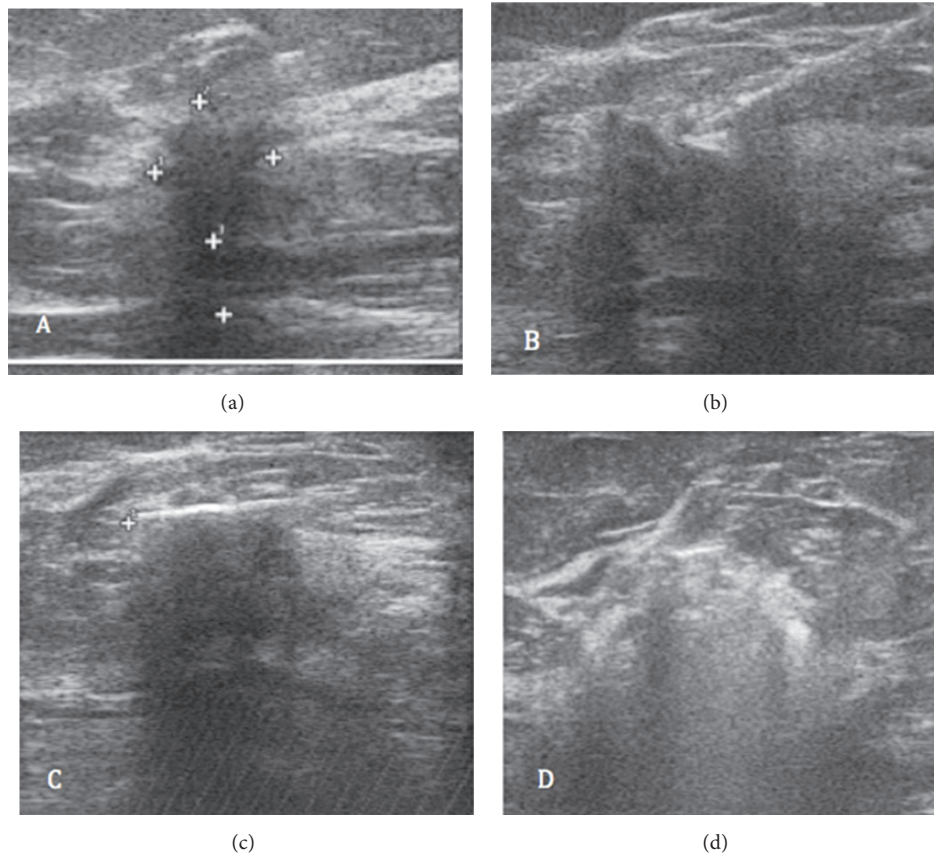


FIGURE 3: Another example of successful LA ablation in a patient with invasive ductal carcinoma of 15 mm of max diameter in the upper outer quadrant of the right breast. (a) The US image before treatment shows the hypoechoic lesion with blurred margins. (b) The US image shows the laser applicator (21G needle and fiber) which, with a course parallel to the chest wall, reaches the outer edge of the lesion. (c) Finally, the lesion is no longer appreciable, and in the treated area, there is an echogenic line with an evident shadow cone. (d) The US image of the ablated area in the first hours after treatment appears in the form of a heterogeneous predominantly hyperechoic zone (gas bubbles) with blurred margins.

and the secondary formation of air bubbles [22]. The choice of the amount of energy administered to ablate the treated lesions accorded with previous reports [23–26].

The choice of lesions up to 20 mm in the greatest diameter is due to the waited association between the success rate of laser ablation and tumor size. The fine needle approach offered the maximum flexibility and it allowed a tailored approach to the characteristics and location of the tumor. Increased experience of the radiologist could lead to the ablation of larger lesions. None of our patients demonstrated a radiological disease progression.

A breast MRI would have been an ideal contrasted baseline examination in addition to the mammogram and ultrasound, since it represents one of the most sensitive techniques to assess the real extension of the lesion [29, 30]. However, in our group of patients, considering the age factor and associated comorbidities of renal failure and pacemakers in situ, we could not perform an MRI as a baseline examination to all patients. This can represent a limitation of our study.

Other limitation is related to the type of evaluation after treatment, depending only on the imaging, without histological confirmation of the response to the treatment. A

future prospective study is going to need a longer follow-up and an evaluation of efficacy, proved through a biopsy after treatment.

Moreover, in other case reports about small lesions (up to 15 mm), authors have reported response rates to ablative technique through mammography and US [21].

Less than 15% of our patients showed complications as mild pain during procedure, while all the patients complained of a mild dull aching pain after procedure. Long-term cosmetic result was also satisfactory. Among the limitations of the study, there is the small number of patients, highly selected in the group of elderly patients affected by unifocal tumors who are nonsurgical candidates. However, through our pilot study, we can state that laser ablation can be useful and feasible in the treatment of single small breast cancers with complete necrosis of the lesion, good cosmetic outcome, and cost effectiveness.

5. Conclusion

Laser ablation is a feasible, minimally invasive, and cost-effective alternative for a subset of patients affected by small lesions, who are not eligible to the standard surgical approach,

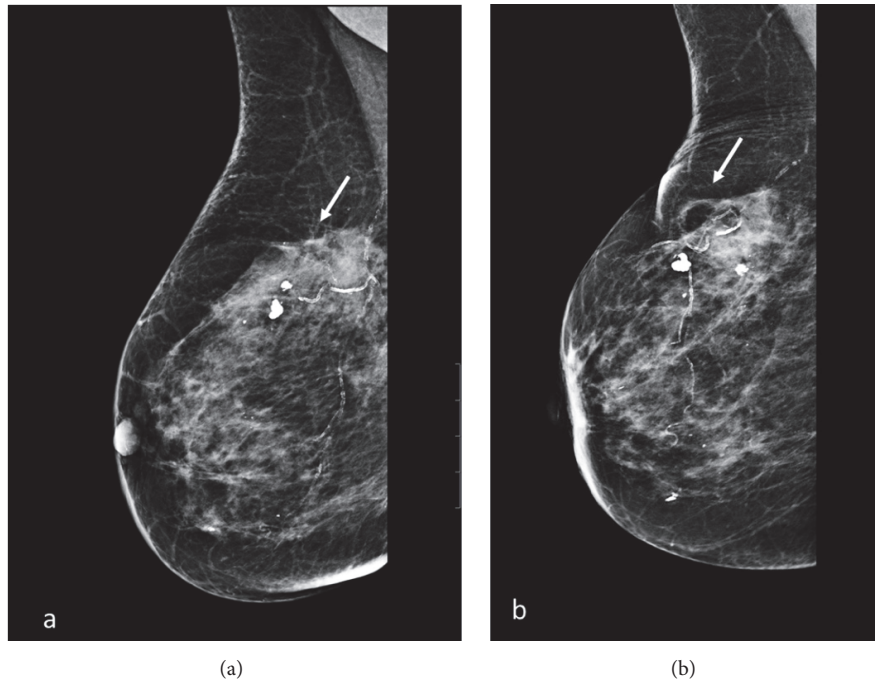


FIGURE 4: Sequential mammograms showing the cystic oil formation by steatonecrosis over a period of 24 months. (a) Before LA (white arrow) and (b) 24 month after a single laser treatment (white arrow).

as well as for patients who refuse surgery. However, further larger prospective studies are strongly needed in order to confirm our preliminary results.

Ethical Approval

This study received clinical trial approval from the Clinical Ethics Committee of Florence on 22-07-2011 bearing the number 591/11.

Conflicts of Interest

The authors declare that there are no conflicts of interest

References

- [1] American Cancer Society, *Cancer Facts & Figures 2016*, American Cancer Society, Atlanta, Ga, USA, 2016.
- [2] D. A. Berry, K. A. Cronin, S. K. Plevritis et al., "Effect of screening and adjuvant therapy on mortality from breast cancer," *The New England Journal of Medicine*, vol. 353, no. 17, pp. 1784–1792, 2005.
- [3] J. G. Elmore, K. Armstrong, C. D. Lehman, and S. W. Fletcher, "Screening for breast cancer," *The Journal of the American Medical Association*, vol. 293, no. 10, pp. 1245–1256, 2005.
- [4] National Cancer Institute Surveillance, *Epidemiology and End Results: Breast Cancer Incidence and Mortality*, (SEER) Program, Rockville, Md, USA, 2013.
- [5] R. Arriagada, M. G. Lê, J.-M. Guinebretière, A. Dunant, F. Rochard, and T. Tursz, "Late local recurrences in a randomised trial comparing conservative treatment with total mastectomy in early breast cancer patients," *Annals of Oncology*, vol. 14, no. 11, pp. 1617–1622, 2003.
- [6] E. Bastiaannet, G. J. Liefers, A. J. M. de Craen et al., "Breast cancer in elderly compared to younger patients in the Netherlands: stage at diagnosis, treatment and survival in 127,805 unselected patients," *Breast Cancer Research and Treatment*, vol. 124, no. 3, pp. 801–807, 2010.
- [7] M. B. El-Tamer, B. M. Ward, T. Schiffner, L. Neumayer, S. Khuri, and W. Henderson, "Morbidity and mortality following breast cancer surgery in women: National benchmarks for standards of care," *Annals of Surgery*, vol. 245, no. 5, pp. 665–671, 2007.
- [8] G. Manenti, F. Bolacchi, T. Perretta et al., "Small breast cancers: In vivo percutaneous US-guided radiofrequency ablation with dedicated cool-tip radiofrequency system," *Radiology*, vol. 251, no. 2, pp. 339–346, 2009.
- [9] J. Palussière, C. Henriques, L. Mauriac et al., "Radiofrequency ablation as a substitute for surgery in elderly patients with non-resected breast cancer: pilot study with long-term outcomes," *Radiology*, vol. 264, no. 2, pp. 597–605, 2012.
- [10] T. Nguyen, E. Hattery, and V. P. Khatri, "Radiofrequency ablation and breast cancer: a review," *Gland Surgery*, vol. 3, pp. 128–135, 2014.
- [11] G. Manenti, T. Perretta, E. Gaspari et al., "Percutaneous local ablation of unifocal subclinical breast cancer: Clinical experience and preliminary results of cryotherapy," *European Radiology*, vol. 21, no. 11, pp. 2344–2353, 2011.
- [12] C. Pusceddu, B. Sotgia, G. Amucano et al., "Breast cryoablation in patients with bone metastatic breast cancer," *Journal of Vascular and Interventional Radiology*, vol. 25, no. 8, pp. 1225–1232, 2014.
- [13] P. J. Littrup, B. Jallad, P. Chandiwala-Mody, M. D'Agostini, B. A. Adam, and D. Bouwman, "Cryoablation for breast cancer:

- a feasibility study without excision,” *Journal of Vascular and Interventional Radiology*, vol. 20, no. 10, pp. 1329–1341, 2009.
- [14] E. D. Staren, M. S. Sabel, L. M. Gianakakis et al., “Cryosurgery of breast cancer,” *Archives of Surgery*, vol. 132, no. 1, pp. 28–34, 1997.
- [15] M. A. Roubidoux, M. S. Sabel, J. E. Bailey, C. G. Kleer, K. A. Klein, and M. A. Helvie, “Small (< 2.0-cm) breast cancers: mammographic and US findings at US-guided cryoablation—initial experience,” *Radiology*, vol. 233, no. 3, pp. 857–867, 2004.
- [16] W. E. Burak Jr., D. M. Agnese, S. P. Povoski et al., “Radiofrequency ablation of invasive breast carcinoma followed by delayed surgical excision,” *Cancer*, vol. 98, no. 7, pp. 1369–1376, 2003.
- [17] M. Noguchi, M. Earashi, H. Fujii, K. Yokoyama, K.-I. Harada, and K. Tsuneyama, “Radiofrequency ablation of small breast cancer followed by surgical resection,” *Journal of Surgical Oncology*, vol. 93, no. 2, pp. 120–128, 2006.
- [18] W. Zhou, Y. Jiang, L. Chen et al., “Image and pathological changes after microwave ablation of breast cancer: a pilot study,” *European Journal of Radiology*, vol. 83, no. 10, pp. 1771–1777, 2014.
- [19] F. Wu, Z.-B. Wang, Y.-D. Cao et al., “A randomised clinical trial of high-intensity focused ultrasound ablation for the treatment of patients with localised breast cancer,” *British Journal of Cancer*, vol. 89, no. 12, pp. 2227–2233, 2003.
- [20] F. Wu, Z.-B. Wang, H. Zhu et al., “Extracorporeal high intensity focused ultrasound treatment for patients with breast cancer,” *Breast Cancer Research and Treatment*, vol. 92, no. 1, pp. 51–60, 2005.
- [21] K. Dowlatshahi, J. J. Dieschbourg, and K. J. Bloom, “Laser therapy of breast cancer with 3-year follow-up,” *The Breast Journal*, vol. 10, no. 3, pp. 240–243, 2004.
- [22] K. H. Haraldsdóttir, K. Ivarsson, S. Götberg, C. Ingvar, U. Stenram, and K.-G. Tranberg, “Interstitial laser thermotherapy (ILT) of breast cancer,” *European Journal of Surgical Oncology*, vol. 34, no. 7, pp. 739–745, 2008.
- [23] C. M. Pacella, G. Bizzarri, G. Francica et al., “Percutaneous laser ablation in the treatment of hepatocellular carcinoma with small tumors: analysis of factors affecting the achievement of tumor necrosis,” *Journal of Vascular and Interventional Radiology*, vol. 16, no. 11, pp. 1447–1457, 2005.
- [24] C. M. Pacella, G. Francica, F. M. L. Di Lascio et al., “Long-term outcome of cirrhotic patients with early hepatocellular carcinoma treated with ultrasound-guided percutaneous laser ablation: a retrospective analysis,” *Journal of Clinical Oncology*, vol. 27, no. 16, pp. 2615–2621, 2009.
- [25] C. M. Pacella, G. Mauri, G. Achille et al., “Outcomes and risk factors for complications of laser ablation for thyroid nodules: A multicenter study on 1531 patients,” *The Journal of Clinical Endocrinology & Metabolism*, vol. 100, no. 10, pp. 3903–3910, 2015.
- [26] G. Mauri, L. Cova, T. Ierace et al., “Treatment of metastatic lymph nodes in the neck from papillary thyroid carcinoma with percutaneous laser ablation,” *CardioVascular and Interventional Radiology*, vol. 39, no. 7, pp. 1023–1030, 2016.
- [27] M. Ahmed, L. Solbiati, C. L. Brace et al., “Image-guided tumor ablation: standardization of terminology and reporting criteria—a 10-year update,” *Journal of Vascular and Interventional Radiology*, vol. 25, pp. 1691–1705, 2014.
- [28] D. Sacks, T. E. McClenny, J. F. Cardella, and C. A. Lewis, “Society of interventional radiology clinical practice guidelines,” *Journal of Vascular and Interventional Radiology*, vol. 14, pp. S199–S202, 2003.
- [29] C. Kuhl, W. Kuhn, M. Braun, and H. Schild, “Pre-operative staging of breast cancer with breast MRI: one step forward, two steps back?” *The Breast*, vol. 16, supplement 2, pp. S34–S44, 2007.
- [30] C. K. Kuhl, “Current status of breast MR imaging: Part 2. Clinical applications,” *Radiology*, vol. 244, no. 3, pp. 672–691, 2007.

Review Article

Use of Quantitative Morphological and Functional Features for Assessment of Axillary Lymph Node in Breast Dynamic Contrast-Enhanced Magnetic Resonance Imaging

Roberta Fusco ¹, Mario Sansone ², Vincenza Granata ¹, Maurizio Di Bonito,³
Franca Avino,⁴ Orlando Catalano,¹ Gerardo Botti,³ and Antonella Petrillo ¹

¹Radiology Unit, “Dipartimento di Supporto ai Percorsi Oncologici Area Diagnostica, Istituto Nazionale Tumori-IRCCS-Fondazione G. Pascale”, Via Mariano Semmola, Naples, Italy

²Department of Electrical Engineering and Information Technologies, University “Federico II” of Naples, Via Claudio, Naples, Italy

³Pathology Unit, “Dipartimento di Supporto ai Percorsi Oncologici Area Diagnostica, Istituto Nazionale Tumori-IRCCS-Fondazione G. Pascale”, Via Mariano Semmola, Naples, Italy

⁴Senology Surgery Unit, “Dipartimento Corp-S Assistenziale e di Ricerca dei Percorsi Oncologici del Distretto Toracico, Istituto Nazionale Tumori-IRCCS-Fondazione G. Pascale”, Via Mariano Semmola, Naples, Italy

Correspondence should be addressed to Roberta Fusco; r.fusco@istitutotumori.na.it

Received 10 December 2017; Accepted 29 April 2018; Published 30 May 2018

Academic Editor: Giuseppe Falco

Copyright © 2018 Roberta Fusco et al. This is an open access article distributed under the Creative Commons Attribution License, which permits unrestricted use, distribution, and reproduction in any medium, provided the original work is properly cited.

Background. Axillary lymph-node assessment is considered one of the most important prognostic factors concerning breast cancer survival. **Objective.** We investigated the discriminative power of morphological and functional features in assessing the axillary lymph node. **Methods.** We retrospectively analysed data from 52 consecutive patients who undergone DCE-MRI and were diagnosed with primary breast carcinoma: 94 lymph nodes were identified. Per each lymph node, we extracted morphological features: circularity, compactness, convexity, curvature, elongation, diameter, eccentricity, irregularity, radial length, entropy, rectangularity, roughness, smoothness, sphericity, spiculation, surface, and volume. Moreover, we extracted functional features: time to peak (TTP), maximum signal difference (MSD), wash-in intercept (WII), wash-out intercept (WOI), wash-in slope (WIS), wash-out slope (WOS), area under gadolinium curve (AUGC), area under wash-in (AUWI), and area under wash-out (AUWO). Selection of important features in predicting metastasis has been done by means of receiver operating characteristic (ROC) analysis. Performance of linear discriminant analysis was analysed. **Results.** All morphological features but circularity showed a significant difference between median values of metastatic lymph nodes group and nonmetastatic lymph nodes group. All dynamic parameters except for MSD and WOS showed a statistically significant difference between median values of metastatic lymph nodes group and nonmetastatic lymph nodes group. Best results for discrimination of metastatic and nonmetastatic lymph nodes were obtained by AUGC (accuracy 75.8%), WIS (accuracy 71.0%), WOS (accuracy 71.0%), and AUCWO (accuracy 72.6%) for dynamic features and by compactness (accuracy 82.3%), curvature (accuracy 71.0%), radial length (accuracy 71.0%), roughness (accuracy 74.2%), smoothness (accuracy 77.2%), and speculation (accuracy 72.6%) for morphological features. Linear combination of all morphological and/or of all dynamic features did not increase accuracy in metastatic lymph nodes discrimination. **Conclusions.** Compactness as morphological feature and area under time-intensity curve as dynamic feature were the best parameters in identifying metastatic lymph nodes on breast MRI.

1. Background

In 2017, breast cancer had the highest incidence among female cancers and is still the second (after lung) leading cause of death from cancer in the US [1]. The transition

from nonmetastatic to metastatic state of breast cancer is characterised by the diffusion of the primary lesion towards lymphatic sites. Therefore, accurate evaluation of metastasis in axillaries lymphatic nodes is a crucial factor affecting medical management, surgery, and prognosis [2–4].

Sentinel lymph-node biopsy (SLNB) has been effectively used for identifying, via radiotracer and/or blue dye, the nodes draining the breast which are possibly the first to be encountered during tumor spreading [5]. SLNB is commonly executed after surgical removal of the primary lesion and has shown an accuracy of 93.5 to 97.5% [6, 7]. However, it has been noticed that SLNB can have long-term morbidity that potentially can affect the quality of life despite being less significant than axillary lymph-node dissection [8, 9]. In addition, preoperative evaluation of axillary lymph nodes might improve patient-based treatment: in fact, options might include neoadjuvant chemotherapy, intraoperative breast radiotherapy, and reconstruction planning. Moreover, when metastatic axillary disease is diagnosed before surgery, the surgeon can discuss specific aspects of axillary lymph-node dissection with the patient.

Despite being not very accurate, imaging techniques such as ultrasound (US), computed tomography (CT), and positron emission tomography (PET)/CT are often used in clinical practice [10–13]. Breast magnetic resonance imaging (MRI), because of its versatility, has gained a large consensus over the past two decades and many technological improvements have contributed to its diffusion [12]. In particular, dynamic contrast-enhanced magnetic resonance imaging (DCE-MRI) has been shown to be able to distinguish benign from malignant breast lesions by means of simultaneous evaluation of morphological and functional information. At the time of writing, axillary lymph nodes evaluation via DCE-MRI has not yet been introduced in clinical practice. Mainly, diagnostic criteria for malignancy of axillary lymph nodes are based exclusively on morphology; however, these are still controversial [11, 14, 15].

In this study, we investigated the discriminative power of MRI in both morphological and functional features derived by dynamic contrast-enhanced MRI (DCE-MRI) for axillary lymph-node evaluation. We attempted to identify the best quantitative feature to discriminate metastatic from nonmetastatic lymph nodes among 26 morphological and functional parameters and their linear combinations.

2. Methods

2.1. Patients Inclusion Criteria. A prospectively collected database has been reviewed after Institutional Review Board approval. We identified 268 consecutive patients from February 2009 to December 2013 for newly diagnosed breast carcinoma. All these subjects had undergone DCE-MRI in a single cancer centre. The study population comprised 52 patients with breast cancer who also underwent pathological evaluation of axillary lymph nodes. Age ranged from 31 to 58 years. Patients included in the study (1) had breast cancer with clinical evaluation (TNM score) T1-T2 and (2) underwent SLNB or/and axillary lymphadenectomy. Patients who carried an implanted device, were pregnant, or had any contraindication for MRI were not included in the study. In addition, we excluded patients having undergone radiation therapy or chemotherapy within 12 months before the MRI. All patients provided informed consent to the use of their data for research purposes. This retrospective study

was performed according to regulations issued by our local Institutional Review Board.

2.2. MRI Methodology. DCE-MRI has been executed using 1.5 T breast-dedicated equipment (Aurora; Aurora Imaging Technology, North Andover, USA), embodying an in-table coil [14]. Exams were arranged from the 7th to 14th day of the menstrual cycle in premenopausal women; no scheduling limitations were applied in postmenopausal women.

The sequence used for precontrast imaging was a three-dimensional (3D) nonspoiled SPIRAL-RODEO fat-sat (TR 29 ms, TE 4.8 ms, flip angle 45°, matrix 512 × 512, thickness 1.13 mm, and gap 1.13 mm); after contrast injection, four dynamic 3D spoiled SPIRAL-RODEO fat-sat acquisitions (TR 29 ms, TE 4.8 ms, flip angle 45°, matrix 512 × 512, thickness 1.13 mm, and gap 1.13 mm) were used. The time interval between acquisitions was 90 s. A bolus of gadobenate dimeglumine (Multihance, Gd-BOPTA Bracco; Atlanta Pharma, Konstanz, Germany) has been intravenously injected using a dose of 0.1 mmol/kg body weight at a flow rate of 2 ml/s, followed by 20 ml of saline solution at the same rate. An automatic contrast delivery system was employed (Optistar Elite, Covidien Imaging Solution, Hazelwood, USA).

2.3. Histopathological Evaluation and Operation of Axillary Lymph Nodes. Samples of SLNB were assessed by immediate frozen section and hematoxylin and eosin staining. The nodes were subsequently submitted for permanent sectioning and immunohistochemical assay. According to the American Joint Committee on Cancer guidelines for breast cancer staging [16], a patient with isolated tumor cells was considered node-negative and did not undergo any additional lymph-node surgery.

2.4. Images Analysis. Two radiologists having more than 15 years of experience (AP) and more than 10 years of experience (SF), respectively, reviewed images. For each lymph node having a lower diameter ≥ 10 mm, the manual segmentation was made using OsiriX v.3.8.1, on the data acquired after contrast injection using a pulse sequence for three-dimensional fat-saturated axial nonspoiled SPIRAL-RODEO images (Figure 1). Per each lymph node, on each slice, a region of interest (ROI) was drawn: the set of all ROIs corresponding to a single lymph node formed a Volume of Interest (VOI). ROI border has been placed in the lymph-node periphery close to the margin. Lymph nodes were evaluated using quantitative descriptors involving morphological and dynamic parameters.

2.5. Dynamic Parameters. Nine dynamic features emerged from the literature [17–20], which were extracted using the approach previously reported in a previous publication from our group [19] (Figure 2): maximum signal difference (MSD), the time to peak (TTP) between the wash-in (WI) and wash-out (WO) segments, the WI slope (WIS), the WO slope (WOS), the WI intercept (WII), the WO intercept (WOI), the area under curve (AUC), the area under WI tract (AUCWI), and the area under WO tract (AUCWO).

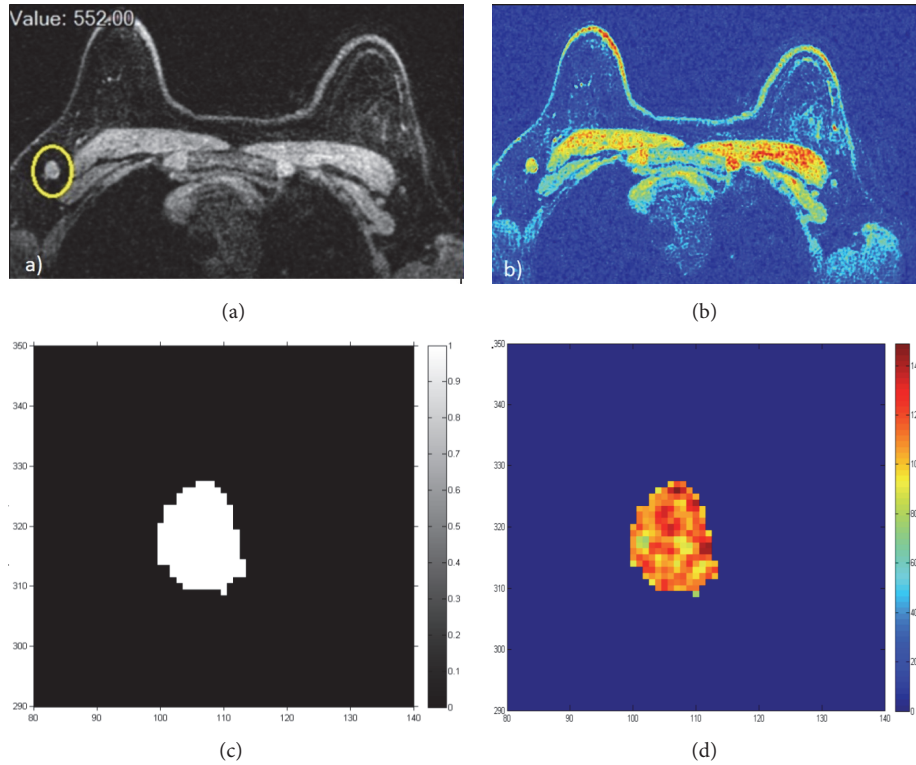


FIGURE 1: Lymph-node illustration on contrast-enhanced MR imaging and their segmentation for a single slice: (a)–(c) grey level; (b)–(d) RGB values.

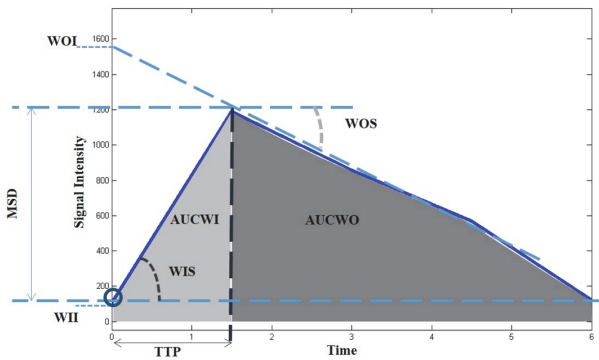


FIGURE 2: Dynamic parameters illustration.

2.6. *Feature Extraction.* Per each VOI, 17 morphological features were calculated [21–23]. Before feature computation, all lymph-node binary masks have been reinterpolated on a common grid of equal size ($1 \times 1 \times 1 \text{ mm}^3$) in three orthogonal directions. A brief description of all morphological features has been provided in Table 1. Detailed mathematical definitions might slightly vary among studies; therefore, we report the specific definitions we used:

- (1) Circularity = (volume of the sphere with average lymph-node radius)/(lymph-node volume).
- (2) Compactness = (lymph-node surface area)/(lymph-node volume).

- (3) Irregularity = $1 - (\text{surface area of the sphere with average lymph-node radius})/(\text{lymph-node surface area})$.
- (4) Diameter = diameter of the sphere corresponding to the lymph-node volume.
- (5) Rectangularity = (lymph-node volume)/(volume of the smallest parallelepiped containing the lymph node).
- (6) Radial length = average distance between boundary points and lymph-node barycentre.
- (7) Volume = number of voxels of the lymph node times the volume of a single voxel.
- (8) Smoothness = $(1/N) \sum_n R_n - (R_{n-1} + R_{n+1})/2$, where R_n is the n th boundary point distance from the barycentre along a lymph-node slice.
- (9) Curvature = $\text{average}(\text{abs}(x' y'' - y' x''))/(x'^2 + y'^2)^{(3/2)}$, where x, y are the coordinate parametric representation of the boundary points along a lymph-node slice, x', y' are the first derivative with respect to the parameter, and x'', y'' are the second derivative.
- (10) Roughness: $([(1/N) \sum_{n=1}^N (R_n - \mu)^4]^{1/4} - [(1/N) \sum_{n=1}^N (R_n - \mu)^2]^{1/2})/\mu$, where N is the number of points of the boundary, R_n is the radial distance of the n th point, and μ is the average radial distance.
- (11) Sphericity = (average radial length)/(standard deviation radial length).

TABLE 1: List of features used in analysis with definitions.

Feature category	Feature	Description
Dynamic	TTP	Time to peak
	MSD	Maximum signal difference
	AUGC	Area under gadolinium curve
	AUCWI	Area under gadolinium curve in the wash-in phase
	AUCWO	Area under gadolinium curve in the wash-out phase
	WIS	Wash-in slope
	WII	Wash-in intercept
	WOS	Wash-out slope
	WOI	Wash-out intercept
Morphological	circularity	Similarity of the lesion shape to a sphere
	compactness	Ratio between surface and volume
	convexity	Ratio between the smallest volume with convex curvature that contains the lymph node and its volume
	curvature	Measure of curvature of lymph node contour
	elongation	Parameter that estimates how much the ROI is pronounced along one direction than along the other
	diameter	Diameter of the sphere having the same ROI volume
	eccentricity	Ratio of the larger rope and the largest among the orthogonal ropes
	irregularity	Deviation of the lesion surface from the surface of a sphere
	radial length	Average distance between points on the border and the center of the lymph node
	entropy	Entropy of radial length
	rectangularity	Similarity of the lesion shape to a rectangle
	roughness	Distances of each point of the center than the radial length average
	smoothness	Measurement of lymph node contour irregularities
	sphericity	Ratio between the average radial length and the standard deviation of the rays
	spiculation	Standard deviation of the radial lengths with respect to the radial length average
surface	Sum of lymph nodes contour pixels	
volume	Volume of the entire lymph node	

(12) Eccentricity = (lymph-node largest diameter)/(the largest diameter orthogonal to the previous one).

(13) Surface = number of voxels belonging to the lymph-node boundary.

(14) Spiculation = standard deviation of radial length.

(15) Convexity = (convex-hull volume)/(lymph-node volume);

(16) Entropy: $-\sum_n P(R_n = r_n) \log P(R_n = r_n)$, where $P(R = rn)$ is the distribution of radial length.

(17) Elongation = (length)/(width) of the smallest rectangle containing the lymph node averaged per each slice in three orthogonal directions.

staging. For each parameter, median and standard deviation (SD) were calculated as representative values of segmented VOI. Interobserver agreement was calculated to assess the variability between two readers in the manual lymph-nodes segmentation. As is commonly reported, an interobserver correlation coefficient of 0–0.20 reflected a poor agreement, of 0.21–0.40 reflected a fair agreement, of 0.41–0.60 reflected a moderate agreement, of 0.61–0.80 reflected a good agreement, and of 0.81–1.00 reflected an excellent agreement. The nonparametric Mann–Whitney test was used to emphasize statistically significant difference between median values of morphological and dynamic parameters in metastatic lymph-nodes group versus nonmetastatic lymph-nodes group. A P value of <0.05 was considered significant for all tests.

2.7. *Statistical Analysis.* Histopathological results after surgical intervention served as a reference standard for N

Receiver operating characteristic (ROC) analysis in addition to sensitivity, specificity, misclassification error (number

TABLE 2: Morphological features median and standard deviation values for each parameter. *P* value was calculated using Mann–Whitney test.

Morphological Features	Metastatic Lymph-nodes		Non Metastatic Lymph-nodes		<i>P</i> value
	Median	SD	Median	SD	
circularity	0,001	0,002	0,002	0,003	0,829
compactness	0,339	0,125	0,453	0,076	0,021
Convexity	0,824	0,133	0,857	0,159	0,005
curvature	0,091	0,038	0,133	0,052	0,001
Elongation	1,133	0,307	1,281	0,430	0,000
diameter	17,812	7,891	14,392	3,278	0,000
eccentricity	1,658	0,584	1,679	0,678	0,000
Irregularity	−3,487	0,562	−3,425	0,760	0,000
radial length	0,929	0,031	0,960	0,020	0,000
Entropy	4,763	0,214	4,664	0,241	0,000
rectangularity	0,358	0,071	0,332	0,092	0,000
Roughness	0,353	0,232	0,102	0,078	0,000
smoothness	4,283	1,914	3,320	0,539	0,000
sphericity/roundness	26,372	15,870	41,890	27,259	0,000
Spiculation	6,602	2,656	4,323	1,369	0,000
Surface	1094,000	1207,675	698,000	540,839	0,000
volume	2959,000	7956,682	1561,000	1114,509	0,000

TABLE 3: Dynamic features median and standard deviation values for each parameter. *P* value was calculated using Mann–Whitney test.

Features	Metastatic Lymph-nodes		Non Metastatic Lymph-nodes		<i>P</i> value
	Median	SD	Median	SD	
MSD	1079,000	641,773	597,500	474,324	1,000
TTP	372,261	169,279	459,888	179,981	0,021
AUC	3,000	1,193	3,000	0,994	0,003
WII	1,453	0,215	1,521	0,198	0,001
WOI	11475,000	3002,216	8871,375	2198,225	0,000
WIS	1924,637	819,422	2005,110	668,567	0,037
WOS	1384,000	535,408	1442,450	486,190	0,214
AUCWI	395,952	174,820	468,695	179,586	0,002
AUCWO	2951,250	1549,637	3654,000	1280,761	0,000

of false negatives and false positives over the total), and accuracy (number of true negatives and true positives over the total) has been performed with respect to histopathological results.

Moreover, we applied a linear discriminant analysis (LDA) [24] to identify the best weighted linear combination of features producing the best results considering, respectively, morphological features only, dynamic features only, and both kinds of features together (sensitivity and specificity were reported and were considered significant for the features with an accuracy of >70% at ROC analysis). 10-fold cross-validation has been performed in order to have robust result [24].

Statistical processing and classification have been performed by means of the Statistics Toolbox within Matlab R2007a (MathWorks Inc., Natick, USA).

3. Results

In the present study, 94 dominant lymph nodes were evaluated in 52 patients with primary breast carcinoma: 48 metastatic lymph nodes and 46 not pathological lymph nodes.

Table 2 reports median and standard deviation for each morphological parameter in the metastatic lymph-nodes group versus the nonmetastatic lymph-nodes group. The median of all the parameters, except circularity, showed a statistically significant difference between the two groups.

Table 3 reports median and standard deviation for each dynamic parameter in the metastatic lymph-nodes group versus the nonmetastatic lymph-nodes group. The median of all parameters, except MSD and WOS, showed a statistically significant difference between the two groups.

TABLE 4: ROC analysis findings for each morphological and dynamic parameter in terms of sensitivity, specificity, misclassification error, and accuracy.

Features	Sensitivity [%]	Specificity [%]	Misclassification Error [%]	Accuracy [%]	AUC
MSD	73,910	64,100	32,260	67,740	0.668
TTP	38,890	34,620	62,900	37,100	0.516
AUC	80,770	72,220	24,190	75,810	0.769
WII	40,000	43,240	58,060	41,940	0.501
WOI	44,830	45,450	54,840	45,160	0.437
WIS	78,260	66,670	29,030	70,970	0.717
WOS	70,970	70,970	29,030	70,970	0.657
AUCWI	28,570	39,020	64,520	35,480	0.459
AUCWO	81,820	67,500	27,420	72,580	0.766
Circularity	60,980	71,430	35,480	64,520	0.762
Compactness	83,330	81,250	17,740	82,260	0.824
Convexity	42,420	41,380	58,060	41,940	0.469
Curvature	68,570	74,070	29,030	70,970	0.770
Elongation	57,890	62,500	40,320	59,680	0.680
Diameter	69,230	63,890	33,870	66,130	0.738
Eccentricity	52,630	54,170	46,770	53,230	0.453
Irregularity	54,550	55,170	45,160	54,840	0.448
Radial Length	76,000	67,570	29,030	70,970	0.811
Entropy	62,500	72,730	33,870	66,130	0.699
Rectangularity	56,670	56,250	43,550	56,450	0.564
Roughness	85,710	68,290	25,810	74,190	0.834
Smoothness	90,480	70,730	22,580	77,420	0.810
Sphericity/roundness	62,790	78,950	32,260	67,740	0.710
Spiculation	81,820	67,500	27,420	72,580	0.742
Surface	68,180	60,000	37,100	62,900	0.713
Volume	92,860	62,500	30,650	69,350	0.738

TABLE 5: LDA analysis findings when all morphological and dynamic features were considered and when the linear combinations of significant morphological and dynamic features were considered.

	Sensitivity [%]	Specificity [%]	AUC
All dynamic features	77,420	70,970	0.778
All morphological features	70,970	80,650	0.803
All features	64,520	77,400	0.754
All significant dynamic features	85,000	66,700	0.794
All significant morphologic features	88,500	77,800	0.812
All significant features	81,000	65,900	0.789

Interobserver correlation coefficient calculated on VOI for each segmented lymph node was of 0.864 (95% CI: 0.835–0.884) indicating an excellent agreement between the two manual segmentations; in addition, this indicates the robustness of morphological and dynamic parameters calculated on segmented lymph nodes.

Table 4 reports findings of ROC analysis for each morphological and dynamic parameter in terms of sensitivity, specificity, misclassification error, and accuracy. The best discrimination between metastatic lymph nodes and nonmetastatic lymph nodes has been obtained by AUC, WIS, WOS, and AUCWO of the dynamic features and by

compactness, curvature, radial length, roughness, smoothness, and speculation of the morphological features.

Table 5 reports the finding of LDA analysis when all morphological and dynamic features were considered and when the linear combination of significant morphological and dynamic features was considered.

4. Discussion

Histopathologic staging of axillary lymph node is one of the most commonly used predictors of breast cancer survival. Currently, diagnosis of metastatic involvement requires

invasive procedures such as pathologic assessment of biopsy tissue or postsurgery dissection. Conventional MRI with double breast coils can noninvasively evaluate both breasts and simultaneously assess axillary lymph nodes; moreover, new techniques, such as DCE-MRI, are now achieving a sufficient degree of maturity for breast cancer evaluation. The verification of MRI-based diagnoses of a specific node with histopathologic analysis of the same node is still a challenge. Moreover, the use of DCE-MRI for assessment of metastatic axillary lymph nodes has not yet been sufficiently investigated and conflicting results until now have been published [25–32]. In this study, we used several morphological features and several dynamic MRI characteristics of axillary lymph nodes. We investigated whether and how malignant nodes could be assessed preoperatively and noninvasively by means of MRI using both morphologic and dynamic criteria. The sensitivity of these features ranged from 28.6% to 92.9%, and the specificity ranged from 34.6% to 81.3%. The best results for discrimination of nonmetastatic lymph nodes by metastatic lymph nodes have been achieved by AUC, WIS, WOS, and AUCWO, among the dynamic features, and by compactness, curvature, radial length, roughness, smoothness, and speculation, among morphological features. The best dynamic parameter was AUC reporting a sensitivity, specificity, misclassification error, and accuracy of 81%, 72%, 24%, and 76%, respectively. The best morphological parameter was compactness reporting a sensitivity, specificity, misclassification error, and accuracy of 83%, 81%, 18%, and 82%, respectively.

Our results are similar to those of other researchers [25–29]. Choi et al. [25] performed a meta-analysis reporting the diagnostic performance of CT, MRI, and PET/CT for detection of metastatic lymph nodes in cervical cancer patients: for region- and node-based data analysis, MRI sensitivity and specificity were 38% and 97%, respectively. He et al. [26] and Baltzer et al. [27] investigated diagnostic performance of specific morphological and/or dynamic features obtained by MR imaging. He et al. reported the area under ROC (AUROC) for short and long lymph-node axis of 0.89 and 0.74, respectively (sensitivity of 93.3% and specificity of 72.6% for short axis, sensitivity of 88.1% and specificity of 64.1% for long axis) and the AUROC of early stage enhancement rate as a dynamic feature (sensitivity of 97.0% and specificity of 73.5%). Baltzer et al. [27] investigated only the margin of lymph nodes as a morphological parameter reporting a sensitivity of 41.2% and a specificity of 95.2%. Schacht et al. [28] reported the results of a quantitative breast MR image analysis for classification of axillary lymph nodes. The best features in that study were the circularity as a morphological parameter with AUROC of 0.67 and the wash-out rate with AUROC of 0.62. Harada et al. [29] evaluated the diagnostic performance of morphologic features computable from MR images using a contrast agent actually not commercialized (ultrasmall superparamagnetic iron oxide): sensitivity, specificity, and overall accuracy were 36.5%, 94.1%, and 81%, respectively.

On the basis of our results, a linear combination of morphological and dynamic feature does not increase the accuracy in lymph-nodes discrimination. LDA results of each group and combination of groups (morphological and/or

dynamic parameters) were comparable to results of dynamic and morphological parameters considered separately. A future endpoint could be to perform multivariate analysis of functional parameters including other modalities such as PET/CT examination or quantitative parameters derived by hybrid system like PET/MRI [33].

A limit of our study consists of the manual segmentation of lymph nodes. However, an expert breast radiologist performed this procedure. A second limitation is the level of complexity in the “gold standard” due to the difficult task of identifying which lymph nodes were biopsied or dissected and of matching the pathologic results to the imaged nodes.

Disclosure

Each author has participated sufficiently in the submission to take public responsibility for its content.

Conflicts of Interest

The authors have no conflicts of interest to disclose.

References

- [1] <https://www.cancer.org/content/dam/cancer-org/research/cancer-facts-and-statistics/annual-cancer-facts-and-figures/2017/cancer-facts-and-figures-2017.pdf>.
- [2] G. Le Bouedec, T. Gauthier, P. Gimbergues, and J. Dauplat, “Axillary recurrence after negative sentinel lymph node biopsy in breast cancer,” *La Presse Médicale*, vol. 37, no. 11, pp. 1685–1687, 2008.
- [3] P. Strnad, L. Rob, H. Krizová, A. Zuntová, J. Chod, and M. Halaska, “Sentinel lymphatic node biopsy for breast cancer in practice,” *Česká Gynekologie*, vol. 70, no. 4, pp. 291–295, 2005.
- [4] S. W. Beenken, M. M. Urist, Y. Zhang et al., “Axillary Lymph Node Status, but Not Tumor Size, Predicts Locoregional Recurrence and Overall Survival after Mastectomy for Breast Cancer,” *Annals of Surgery*, vol. 237, no. 5, pp. 732–739, 2003.
- [5] S. A. McLaughlin, M. J. Wright, K. T. Morris et al., “Prevalence of lymphedema in women with breast cancer 5 years after sentinel lymph node biopsy or axillary dissection: Objective measurements,” *Journal of Clinical Oncology*, vol. 26, no. 32, pp. 5213–5219, 2008.
- [6] U. Veronesi, G. Paganelli, G. Viale et al., “A randomized comparison of sentinel-node biopsy with routine axillary dissection in breast cancer,” *The New England Journal of Medicine*, vol. 349, no. 6, pp. 546–553, 2003.
- [7] D. N. Krag, S. J. Anderson, T. B. Julian et al., “Technical outcomes of sentinel-lymph-node resection and conventional axillary-lymph-node dissection in patients with clinically node-negative breast cancer: results from the NSABP B-32 randomized phase III trial,” *The Lancet Oncology*, vol. 8, no. 10, pp. 881–888, 2007.
- [8] R. Crane-Okada, R. A. Wascher, D. Elashoff, and A. E. Giuliano, “Long-term morbidity of sentinel node biopsy versus complete axillary dissection for unilateral breast cancer,” *Annals of Surgical Oncology*, vol. 15, no. 7, pp. 1996–2005, 2008.
- [9] A. D. Purushotham, S. Upponi, M. B. Klevesath et al., “Morbidity after sentinel lymph node biopsy in primary breast cancer: results from a randomized controlled trial,” *Journal of Clinical Oncology*, vol. 23, no. 19, pp. 4312–4321, 2005.

- [10] P. Vassallo, G. Edel, N. Roos, A. Naguib, and P. E. Peters, "In-vitro high-resolution ultrasonography of benign and malignant lymph nodes: A sonographic-pathologic correlation," *Investigative Radiology*, vol. 28, no. 8, pp. 698–705, 1993.
- [11] G. C. Dooms, H. Hricak, L. E. Crooks, and C. B. Higgins, "Magnetic resonance imaging of the lymph nodes: Comparison with CT," *Radiology*, vol. 153, no. 3 I, pp. 719–728, 1984.
- [12] S. Ueda, H. Tsuda, H. Asakawa et al., "Utility of 18F-fluorodeoxyglucose emission tomography/ computed tomography fusion imaging (18F-FDG PET/CT) in combination with ultrasonography for axillary staging in primary breast cancer," *BMC Cancer*, vol. 8, article no. 165, 2008.
- [13] K. L. Cooper, Y. Meng, S. Harnan et al., "Positron emission tomography (PET) and magnetic resonance imaging (MRI) for the assessment of axillary lymph node metastases in early breast cancer: systematic review and economic evaluation," *Health Technology Assessment*, vol. 15, no. 4, 2011.
- [14] M. Memarsadeghi, C. C. Riedl, A. Kaneider et al., "Axillary lymph node metastases in patients with breast carcinomas: assessment with nonenhanced versus USPIO-enhanced MR imaging," *Radiology*, vol. 241, no. 2, pp. 367–377, 2006.
- [15] A. Luciani, F. Pigneur, F. Ghozali et al., "Ex vivo MRI of axillary lymph nodes in breast cancer," *European Journal of Radiology*, vol. 69, no. 1, pp. 59–66, 2009.
- [16] S. B. Edge, D. R. Byrd, C. C. Compton, A. G. Fritz, F. L. Greene, and A. Trotti, *American Joint Commission on Cancer. Breast Cancer: Perspectives on Anatomic Staging—Based on The AJCC Staging Manual*, Springer, New York, NY, USA, 7th edition, 2010.
- [17] R. Fusco, M. Sansone, S. Filice et al., "Integration of DCE-MRI and DW-MRI Quantitative Parameters for Breast Lesion Classification," *BioMed Research International*, vol. 2015, Article ID 237863, 12 pages, 2015.
- [18] T. Schlossbauer, G. Leinsinger, A. Wismuller et al., "Classification of small contrast enhancing breast lesions in dynamic magnetic resonance imaging using a combination of morphological criteria and dynamic analysis based on unsupervised vector-quantization," *Investigative Radiology*, vol. 43, no. 1, pp. 56–64, 2008.
- [19] R. Fusco, A. Petrillo, M. Petrillo, and M. Sansone, "Use of tracer kinetic models for selection of semi-quantitative features for DCE-MRI data classification," *Applied Magnetic Resonance*, vol. 44, no. 11, pp. 1311–1324, 2013.
- [20] W. J. Krzanowski, *Principles of multivariate analysis*, vol. 3 of *Oxford Statistical Science Series*, The Clarendon Press, Oxford University Press, New York, 1988.
- [21] D. M. Ikeda, N. M. Hylton, K. Kinkel et al., "Development, standardization, and testing of a lexicon for reporting contrast-enhanced breast magnetic resonance imaging studies," *Journal of Magnetic Resonance Imaging*, vol. 13, no. 6, pp. 889–895, 2001.
- [22] C. E. McLaren, W.-P. Chen, K. Nie, and M.-Y. Su, "Prediction of Malignant Breast Lesions from MRI Features. A Comparison of Artificial Neural Network and Logistic Regression Techniques," *Academic Radiology*, vol. 16, no. 7, pp. 842–851, 2009.
- [23] M. Sansone, R. Fusco, A. Petrillo, M. Petrillo, and M. Bracale, "An expectation-maximisation approach for simultaneous pixel classification and tracer kinetic modelling in dynamic contrast enhanced-magnetic resonance imaging," *Medical & Biological Engineering & Computing*, vol. 49, no. 4, pp. 485–495, 2011.
- [24] R. Fusco, M. Sansone, S. Filice et al., "Pattern Recognition Approaches for Breast Cancer DCE-MRI Classification: A Systematic Review," *Journal of Medical and Biological Engineering*, vol. 36, no. 4, pp. 449–459, 2016.
- [25] H. J. Choi, W. Ju, S. K. Myung, and Y. Kim, "Diagnostic performance of computer tomography, magnetic resonance imaging, and positron emission tomography or positron emission tomography/computer tomography for detection of metastatic lymph nodes in patients with cervical cancer: Meta-analysis," *Cancer Science*, vol. 101, no. 6, pp. 1471–1479, 2010.
- [26] N. He, C. Xie, W. Wei et al., "A new, preoperative, MRI-based scoring system for diagnosing malignant axillary lymph nodes in women evaluated for breast cancer," *European Journal of Radiology*, vol. 81, no. 10, pp. 2602–2612, 2012.
- [27] P. A. T. Baltzer, M. Dietzel, H. P. Burmeister et al., "Application of MR mammography beyond local staging: Is there a potential to accurately assess axillary lymph nodes? Evaluation of an extended protocol in an initial prospective study," *American Journal of Roentgenology*, vol. 196, no. 5, pp. W641–W647, 2011.
- [28] D. V. Schacht, K. Drukker, I. Pak, H. Abe, and M. L. Giger, "Using quantitative image analysis to classify axillary lymph nodes on breast MRI: A new application for the Z 0011 Era," *European Journal of Radiology*, vol. 84, no. 3, pp. 392–397, 2015.
- [29] T. Harada, N. Tanigawa, M. Matsuki, T. Nohara, and I. Narabayashi, "Evaluation of lymph node metastases of breast cancer using ultrasmall superparamagnetic iron oxide-enhanced magnetic resonance imaging," *European Journal of Radiology*, vol. 63, no. 3, pp. 401–407, 2007.
- [30] A. Luciani, T. H. Dao, M. Lapeyre et al., "Simultaneous Bilateral Breast and High-Resolution Axillary MRI of Patients with Breast Cancer: Preliminary Results," *American Journal of Roentgenology*, vol. 182, no. 4, pp. 1059–1067, 2004.
- [31] S. O. Hwang, S.-W. Lee, H. J. Kim, W. W. Kim, H. Y. Park, and J. H. Jung, "The comparative study of ultrasonography, contrast-enhanced MRI, and 18F-FDG PET/CT for detecting axillary lymph node metastasis in T1 breast cancer," *Journal of Breast Cancer*, vol. 16, no. 3, pp. 315–321, 2013.
- [32] S. A. Valente, G. M. Levine, M. J. Silverstein et al., "Accuracy of predicting axillary lymph node positivity by physical examination, mammography, ultrasonography, and magnetic resonance imaging," *Annals of Surgical Oncology*, vol. 19, no. 6, pp. 1825–1830, 2012.
- [33] S. G. Kim, K. Friedman, S. Patel, and M. Hagiwara, "Potential role of PET/MRI for imaging metastatic lymph nodes in head and neck cancer," *American Journal of Roentgenology*, vol. 207, no. 2, pp. 248–256, 2016.